



Title	HIGH FIELD MAGNETISM OF THE HALDANE-GAP MATERIALS AND BIOLOGICAL SYSTEMS
Author(s)	Takeuchi, Tetsuya
Citation	大阪大学, 1992, 博士論文
Version Type	VoR
URL	<a href="https://doi.org/10.11501/3063571">https://doi.org/10.11501/3063571</a>
rights	
Note	

*The University of Osaka Institutional Knowledge Archive : OUKA*

<https://ir.library.osaka-u.ac.jp/>

The University of Osaka

**HIGH FIELD MAGNETISM OF THE HALDANE-GAP MATERIALS  
AND BIOLOGICAL SYSTEMS**

**by Tetsuya TAKEUCHI**

DISSERTATION IN PHYSICS



**THE OSAKA UNIVERSITY  
GRADUATE SCHOOL OF SCIENCE  
TOYONAKA, OSAKA**

HIGH FIELD MAGNETISM OF THE HALDANE-GAP MATERIALS  
AND BIOLOGICAL SYSTEMS

by  
Tetsuya TAKEUCHI

DISSERTATION IN PHYSICS

THE OSAKA UNIVERSITY  
GRADUATE SCHOOL OF SCIENCE  
TOYONAKA, OSAKA

AUGUST, 1992

## CONTENTS

### Part I: HIGH FIELD MAGNETIZATION OF THE HALDANE-GAP MATERIALS

	page
Abstract	1
1. Introduction	3
2. Experimental procedures	
2-1 Samples	7
2-2 Magnetization measurements	9
2-3 Magnetic susceptibility measurements	14
3. Crystal structures	
3-1 NENP and NINO	16
3-2 TMNIN	18
3-3 NINAZ	20
4. Magnetic properties	
4-1 Magnetic properties of NENP and NINO	22
4-2 Magnetic properties of TMNIN and NINAZ	27
5. Experimental results and discussions	
5-1 High field magnetization of NENP and NINO	31
5-2 High field magnetization of TMNIN and NINAZ	45
6. Conclusion	53
REFERENCES	55

Part II: EXTENSION OF THE HIGH FIELD MAGNETISM TO THE BIOLOGICAL  
SYSTEMS

	page
Abstract	58
1. Introduction	59
2. Theory	61
3. Experimental procedures	67
4. Polymerization of fibrinogen in high magnetic fields	
4-1 Structure of fibrin fiber and sample preparation	69
4-3 Experimental results and discussion	73
5. Blood cells in high magnetic fields	
5-1 Materials and experiments	84
5-2 Magnetic orientation of red blood cells	89
5-1 Magnetic orientation of blood platelets	99
6. Conclusion	107
REFERENCES	109
ACKNOWLEDGEMENTS	111

## PART I

### HIGH FIELD MAGNETIZATION OF THE HALDANE-GAP MATERIALS

#### ABSTRACT

Magnetization measurements have been performed on the Haldane gap materials NENP:  $\text{Ni}(\text{C}_2\text{H}_8\text{N}_2)_2\text{NO}_2(\text{ClO}_4)$ , NINO:  $\text{Ni}(\text{C}_3\text{H}_{10}\text{N}_2)_2\text{NO}_2(\text{ClO}_4)$ , TMNIN:  $(\text{CH}_3)_4\text{NNi}(\text{NO}_2)_3$ , and NINAZ:  $\text{Ni}(\text{C}_3\text{H}_{10}\text{N}_2)_2\text{N}_3(\text{ClO}_4)$  by a pulsed high magnetic field. Single crystal samples of NENP and NINO exhibit clear evidence of the existence of the Haldane gap. No magnetization appears up to 10 Tesla (T) reflecting the existence of the Haldane gap and linear magnetization appears in both compounds above this field. The observed anisotropy of the transition field is explained by the Haldane gap energy  $E_g$  and the orthorhombic crystalline field constants D and E in the lowest excited triplet. The parameters are estimated as  $E_g=16.8$  K,  $D=-16.1$  K, and  $E=-1.3$  K for NENP and  $E_g=14.2$  K,  $D=-11.5$  K, and  $E=2.1$  K for NINO.

Powdered sample of TMNIN shows a typical magnetization profile of the Haldane material with the gap energy of 4.1 K. The Haldane gap vanishes around 2.7 T and magnetic saturation is obtained above 30 T. This magnetization process of  $S=1$  linear chain Heisenberg antiferromagnet is observed for the first time in this compounds. In NINAZ, the Haldane gap disappears at around 30 T reflecting a large gap energy with the magnitude of 44.3 K. The relation of the Haldane gap energy  $E_g$  and the intrachain exchange energy  $J$  is obtained from these experiments

to be  $E_g = (0.3 \pm 0.05)|J|$  which is close to the theoretical value of  $E_g = 0.41|J|$ .

## 1. Introduction

There has been an increasing interest in the spin wave energy spectrum of the one-dimensional Heisenberg antiferromagnet. In 1983, Haldane predicted that the one-dimensional Heisenberg antiferromagnet with integer spin value has an energy gap between the singlet ground state and the first excited one while the system with a half-integer spin value has no energy gap.<sup>1)</sup>

In the spin 1/2 case, the eigen state energy was calculated exactly by Bethe using so-called the Bethe ansatz method.<sup>2)</sup> NO energy gap exists above the ground state. Magnetization and susceptibility curves have been calculated by Bonner and Fisher<sup>3)</sup> and corresponding much experimental work has been done. The one-dimensional Heisenberg antiferromagnet system has been believed to have no energy gap irrespective of the spin value.

The prediction by Haldane is now well supported theoretically by numerical calculations and exactly solvable model.<sup>4-12)</sup> The value of this energy gap  $E_g$  in one-dimensional Heisenberg antiferromagnet with  $S=1$  with following exchange Hamiltonian:

$$H = -J \sum S_j S_{j+1}, \quad (1)$$

has been estimated numerically by Monte Carlo method to be  $E_g = 0.41|J|$ .<sup>7)</sup>

The presence of the uniaxial anisotropy ( $DS_z^2$ ) is inevitable for  $S \geq 1$  systems. Furthermore, the interchain exchange interaction ( $J'$ ) always exist in real materials. Botet et al.<sup>5)</sup> have done a finite-size-scaling study of the  $S=1$  one-dimensional

Heisenberg antiferromagnet with D-term. The lowest excited state they considered is triplet, which corresponds to an excitation with total spin 1 from the ground state. The excited triplet splits into a doublet and a singlet due to the D-term. An effect of single ion anisotropy term  $DS_z^2$  on the Haldane gap has been considered and it has been shown that the Haldane gap exist for  $-0.29 < D/|J| < 0.93$ . Moreover, Haldane gap is also stable when the interchain exchange interaction is small.<sup>11)</sup>

$\text{CsNiCl}_3$  was first tried to observe the Haldane gap. Buyers et al.<sup>13)</sup> and Steiner et al.<sup>14)</sup> have done neutron scattering measurements in the short-range-ordered phase above the Néel temperature of  $T_N=4.9$  K. By using the parameters of the spin Hamiltonian obtained from the neutron scattering measurement, these author concluded that the energy gap observed above  $T_N$  cannot be explained by the single ion anisotropy. Then they suggest that their experimental results support the existence of the Haldane gap. However, the interchain exchange interaction  $J'$  is not negligible in comparison with the intrachain exchange interaction  $J$  in this compound ( $J'/J \approx 1.7 \times 10^{-2}$ ) so that it is difficult to observe the ideal Haldane state at enough low temperature. Thus  $\text{CsNiCl}_3$  is not an ideal system as a test sample for the Haldane's conjecture.

Renard et al. have found several organic compounds which contain  $\text{Ni}^{2+}$  chains and have done susceptibility<sup>15,16)</sup> and neutron scattering<sup>15,16,17)</sup> measurements on single crystal samples NENP and NINO with the chemical formulas  $\text{Ni}(\text{C}_2\text{H}_8\text{N}_2)_2\text{NO}_2(\text{ClO}_4)$  and  $\text{Ni}(\text{C}_3\text{H}_{10}\text{N}_2)_2\text{NO}_2(\text{ClO}_4)$ , respectively. These compounds show no

long-range magnetic order down to 0.5 K reflecting negligible interchain exchange interaction and regarded as suitable materials for testing the Haldane gap.

The electron spin resonance (ESR) measurement in pulsed high magnetic field on both compounds was done by Date and Kindo<sup>18)</sup> and they found the resonance between the sub-levels of the excited triplet. Their data were satisfactorily explained by introducing a model that the first excited triplet is described by a localized two-spin-bound state with the resultant spin  $S=1$ . The observed angular and temperature dependencies of the resonance lines are explained by a truncated effective spin Hamiltonian for the two-spin-bound state written by

$$H = g\mu_B SH + D(S_z^2 - S(S+1)/3) + E(S_x^2 - S_y^2), \quad (2)$$

where the last term describes the orthorhombic anisotropy in the plane perpendicular to the chain.

In these circumstances, experiments on one-dimensional Heisenberg antiferromagnet systems with  $S=1$  are clearly needed. In particular, the behavior of these systems in the external magnetic field is very interesting, since the field-induced quenching of the Haldane gap is expected. This paper describes the result of high field magnetization measurements on single crystal samples NENP and NINO. Recently, new Haldane gap materials TMNIN and NINAZ have been found by Renard et al.. The high field magnetization measurements have been also done for these materials. The whole magnetization process have been observed in powdered sample of TMNIN and a large Haldane gap was obtained

in NINAZ. The comparison of these results with the theory are also reported in this paper.

## 2. Experimental procedures

### 2-1 Samples

Single crystal samples used in this experiments are prepared by following methods. NENP is prepared by mixing stoichiometric amounts of  $\text{Ni}(\text{C}_2\text{H}_8\text{N}_2)(\text{H}_2\text{O})_2(\text{ClO}_4)_2$  and  $\text{NaNO}_2$  in aqueous solutions. Stoichiometric mixture of  $\text{Ni}(\text{ClO}_4)_2 \cdot 6\text{H}_2\text{O}$ , 1,3-propanediamine and  $\text{NaNO}_2$  is used as starting materials for NINO. Well-shaped red single crystals are obtained by slow evaporation. The single crystals of NENP and NINO show strong cleavage and usually grow up in the shape as shown in Fig. 1. It is noticed that the cleavage plane is parallel to ab-plane in NENP but it is bc-plane in NINO. Directions of crystal axes are carefully determined by X-ray analysis.

The powdered sample of TMNIN used in the present experiment is prepared by following method.<sup>19)</sup> Fawn compound  $(\text{CH}_3)_4\text{NNi}(\text{NO}_2)_3$  (TMNIN), is immediately precipitated when a concentrated aqueous solution of  $\text{NiBr}(10^{-2} \text{ mol in } 5 \text{ cm}^3)$  is added to an aqueous solution of  $(\text{CH}_3)_4\text{Br}(10^{-2} \text{ mol in } 5 \text{ cm}^3)$  in an excess of sodium nitride ( $6 \times 10^{-2} \text{ mol in } 10 \text{ cm}^3$ ). The compound is insoluble in organic solvents, very slightly soluble in methanol, and slightly soluble in water. Tiny needle-shaped crystals can be obtained under slow evaporation of above solution.

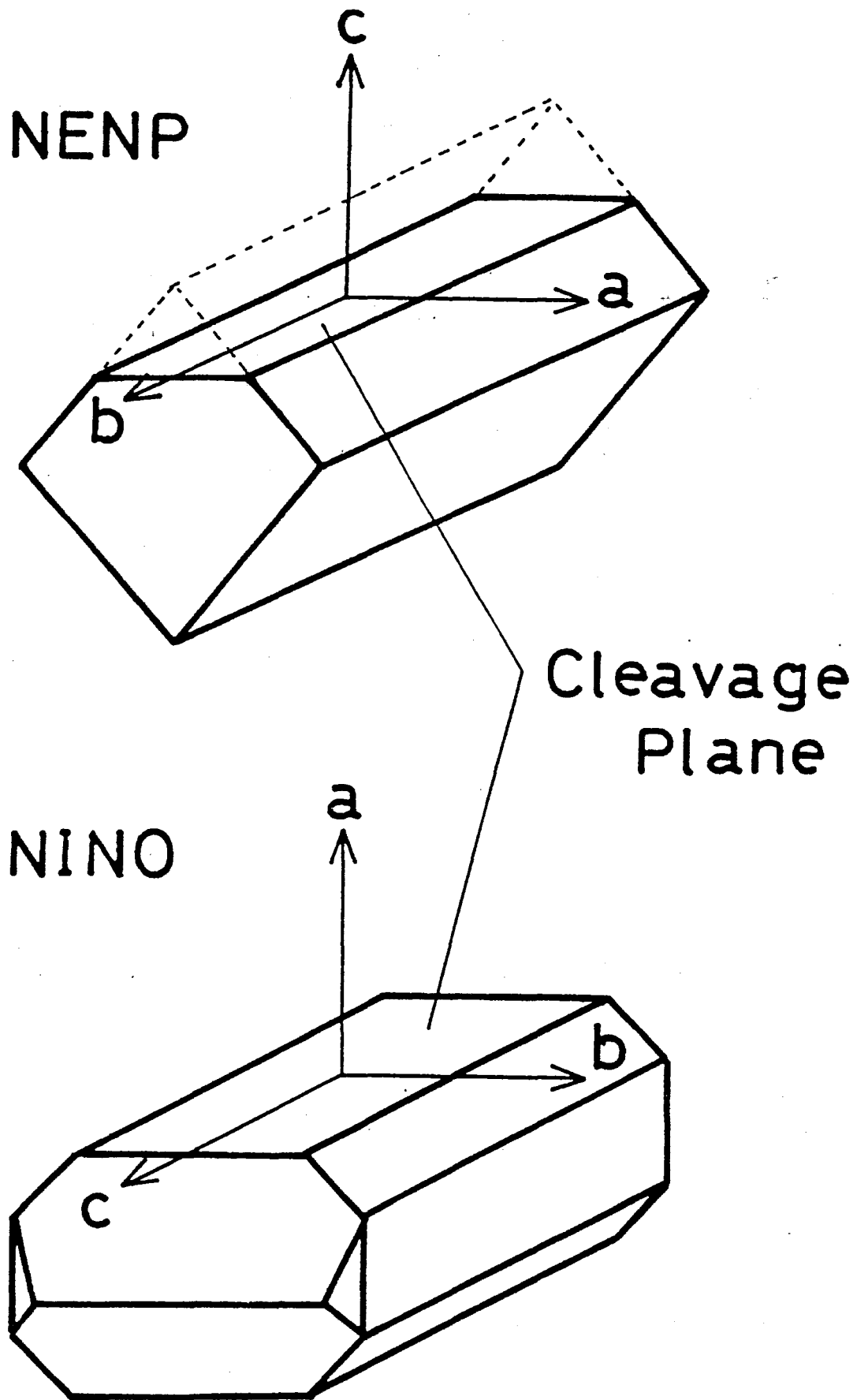
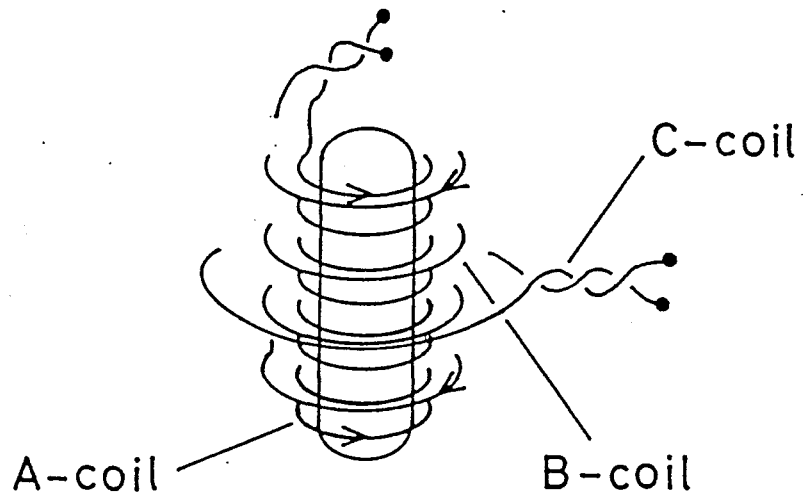


Fig. 1. Sketches of as-grown crystals of NENP and NINO with their crystallographic axes and the cleavage planes.

## 2-2 Magnetization measurements

High field magnetization measurements have been performed at the high magnetic field laboratory of Research Center for Extreme Materials, Osaka University. The two-layer magnet 150(2L)20 and the single-layer large bore magnet 150(1L)60 were used in this experiment. These magnet can produce the magnetic field up to 70 T and 50 T, respectively. The pulse width is about 400  $\mu$ sec. The magnetization was measured by using a balanced pick-up coil system.<sup>20)</sup> The technically important point of the pick-up coil system is how to compensate the background flux change due to a transient field. This is done by setting three coils as shown schematically in Fig. 2. The A-coil picks up the magnetic flux change of the specimen while the B-coil is wound in the opposite direction to the A-coil in order to compensate the background flux change. Fine adjustment is done by adjusting the output of the one-turn C-coil using a bridge balance circuit. The A- and B-coil are wound around the specimen with 80 turns on a 3.0 mm diameter bakelite bobbin and 40 turns on a 4.3 mm diameter bakelite bobbin on the A-coil, respectively. The cross section of B-coil is twice as large as that of A-coil so as to make the net flux in A-coil is equal to that in B-coil. The C-coil is wound on the B-coil. The out-put signal of the bridge balance circuit is proportional to  $dM/dt$  but still contains background noise. The transient digital recorder is used to reduce this residual noise. Two sets of data, with and without specimen, are taken by using two shots of pulsed field. The signal  $dM/dt$  is obtained by the difference of these two

## Pick up coil



## Signal Transmission

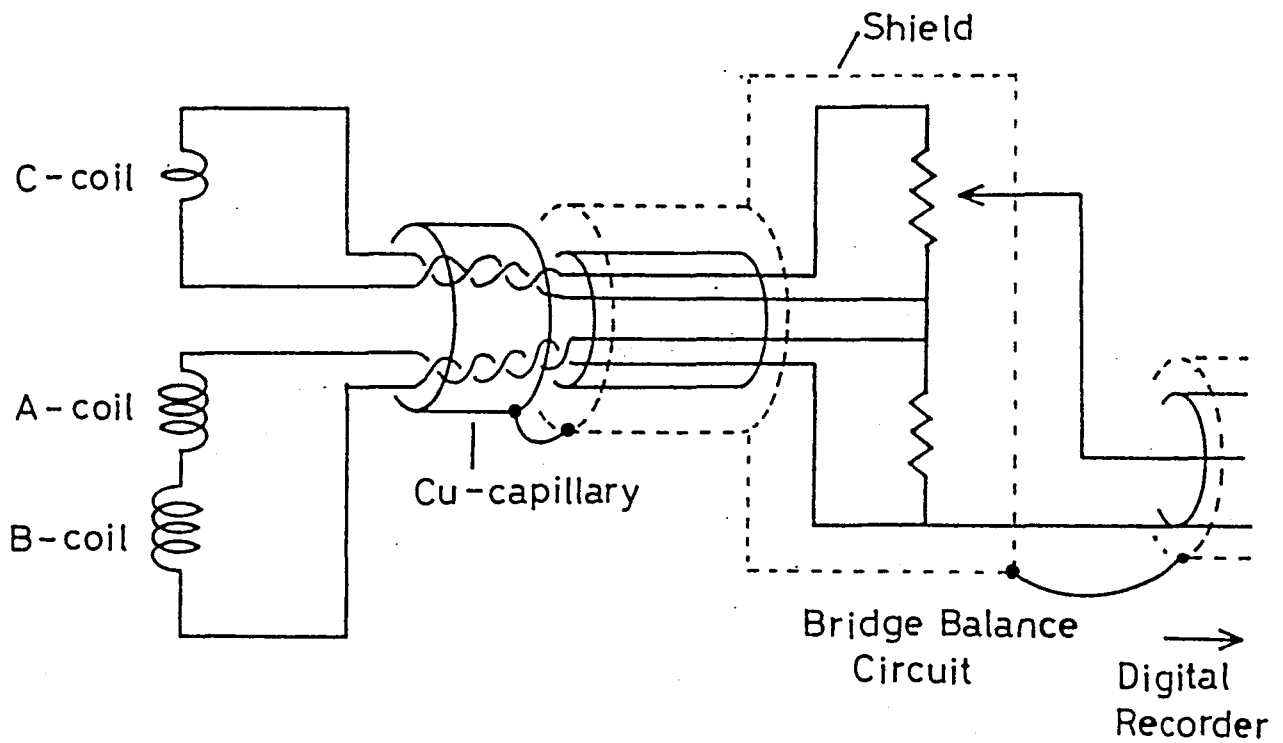


Fig. 2. Schematic view of the pick-up coil system and the bridge balance circuit for the fine compensation.

data. The field derivative of magnetization  $dM/dH$  is calculated by dividing the subtracted data  $dM/dt$  by the signal  $dH/dt$ . The field and magnetization pick-up coils are calibrated by single crystalline  $MnF_2$  as the standard specimen using the spin-flop transition field and the susceptibility above the transition. The block diagram of the magnetization measurement system is shown in Fig. 3.

Magnetization measurement at 1.3 K were done by pumping  $^4He$  in the quartz dewar connected to the high vacuum pump. A conventional single-shot  $^3He$  cryostat was used for the magnetization measurement below 1 K.<sup>21)</sup> The cut view of the cryostats is illustrated in Fig. 4. The dewar vessels and most part of the cryostat are made of glass to avoid the skin effect and eddy current heating due to the pulse field with the pulse width of 400  $\mu$ sec. The exchange gas chamber, as well as the dewar vessels, are silvered along the inside wall with two vertical slits. The slit is necessary to cut the current loop along the wall. However, the slit causes heat inflow of about 100  $\mu$ W to liquid  $^3He$ . The volume of liquid  $^3He$  is about 3  $cm^3$  and experiment in 3-4 hours can be done under usual conditions. The temperature below 1 K is controlled by pumping  $^3He$  gas.

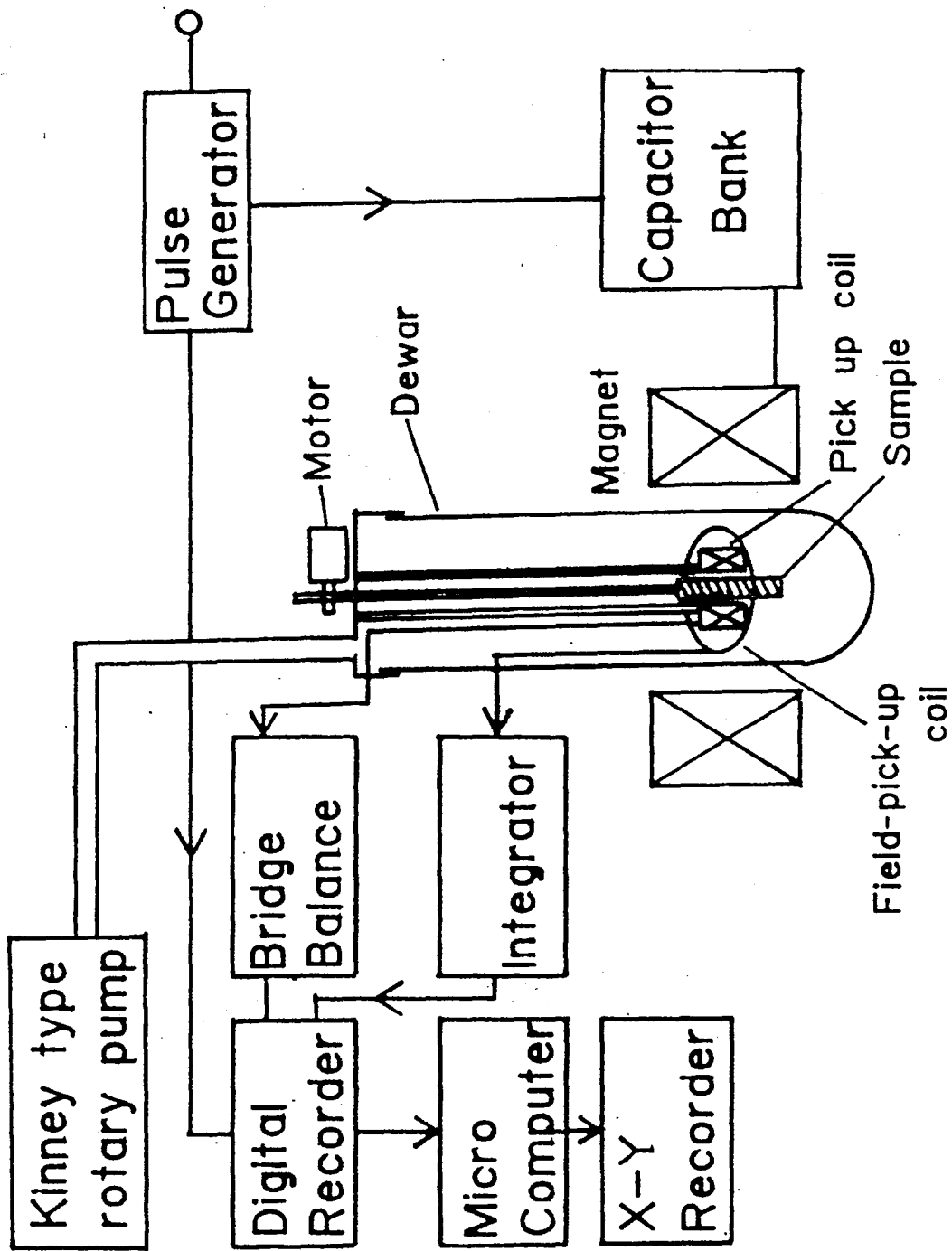


Fig. 3. Block diagram of the magnetization measurement system.

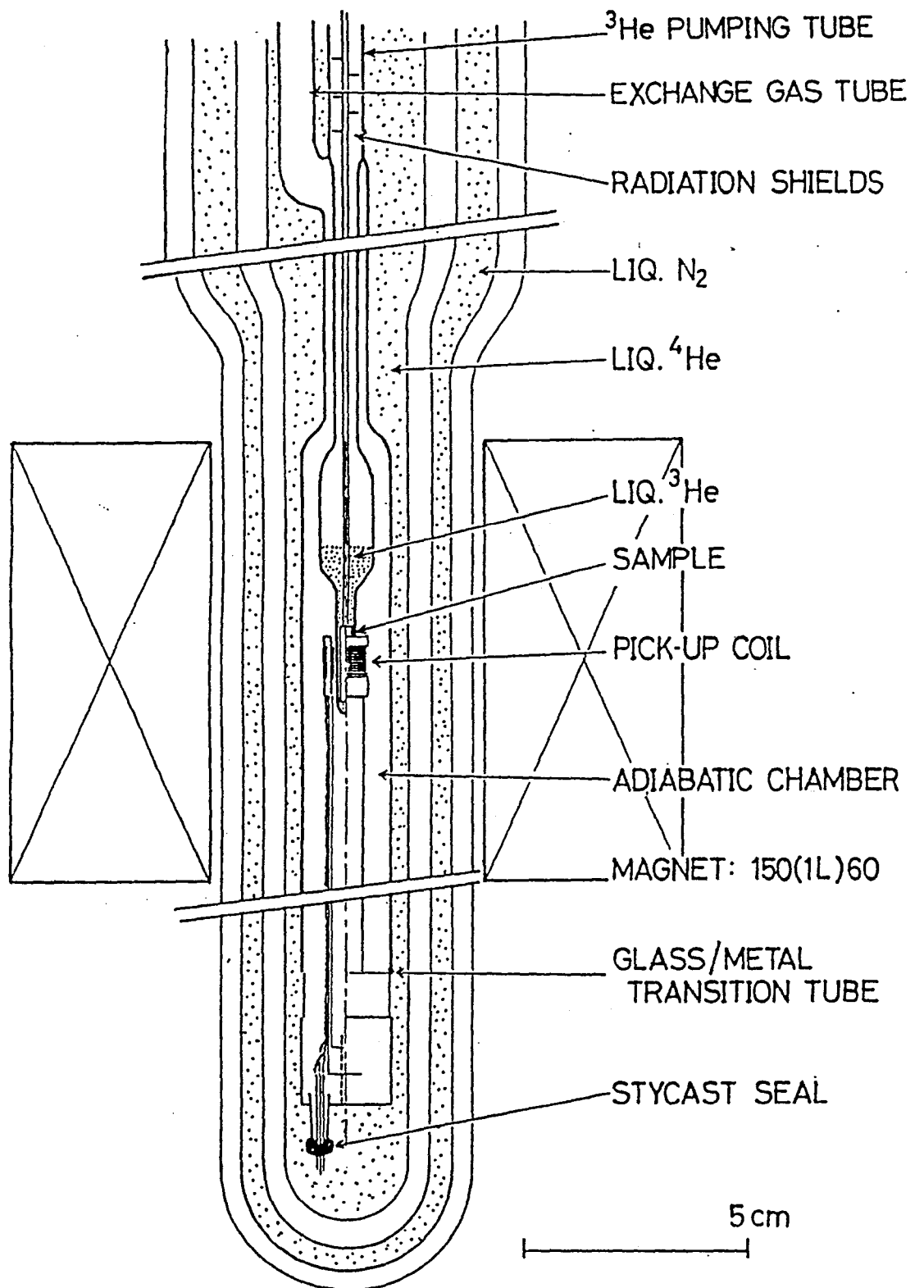


Fig. 4. Cut view of <sup>3</sup>He cryostat.

### 2-3 Magnetic susceptibility measurements

Magnetic susceptibility measurements were performed in the temperature region from 1.5 K to 300 K by the Faraday method using CAHN-2000 Electro-Balance system. The block diagram of magnetic susceptibility measurement system is shown in Fig. 5. The electro-magnet has a gap of about 100 mm. The magnet power supply (IDX corporation IPM-08404-C) is controlled by the computer using the GPIB interface. The balance system is set in  $^4\text{He}$  gas atmosphere with the pressure of about 1 Torr and sample is mounted at the maximum field gradient. All susceptibility measurements were done at the static magnetic field of 3.7 KOe and the field gradient  $dH_z/dz$  of 0.85 KOe/cm. The magnetic force acting on the sample can be obtained by evaluating the current flowing through the torque motor of the balance. This current is monitored by a computing digital multimeter (Takeda Riken TR6877). Subtracting the blank data without sample, the susceptibility is obtained. The magnetic force is calibrated using standard sample  $\text{FeSO}_4(\text{NH}_4)_2\text{SO}_4 \cdot 6\text{H}_2\text{O}$  with susceptibility of  $(31.22 \pm 0.32) \times 10^{-6}$  emu/g at 300 K. Temperature is controlled by two heaters or pumping  $^4\text{He}$  gas and is monitored by digital multimeter (Takeda Riken TR6840) using Au-0.07%Fe vs Ag thermocouple and vapor pressure of  $^4\text{He}$ .

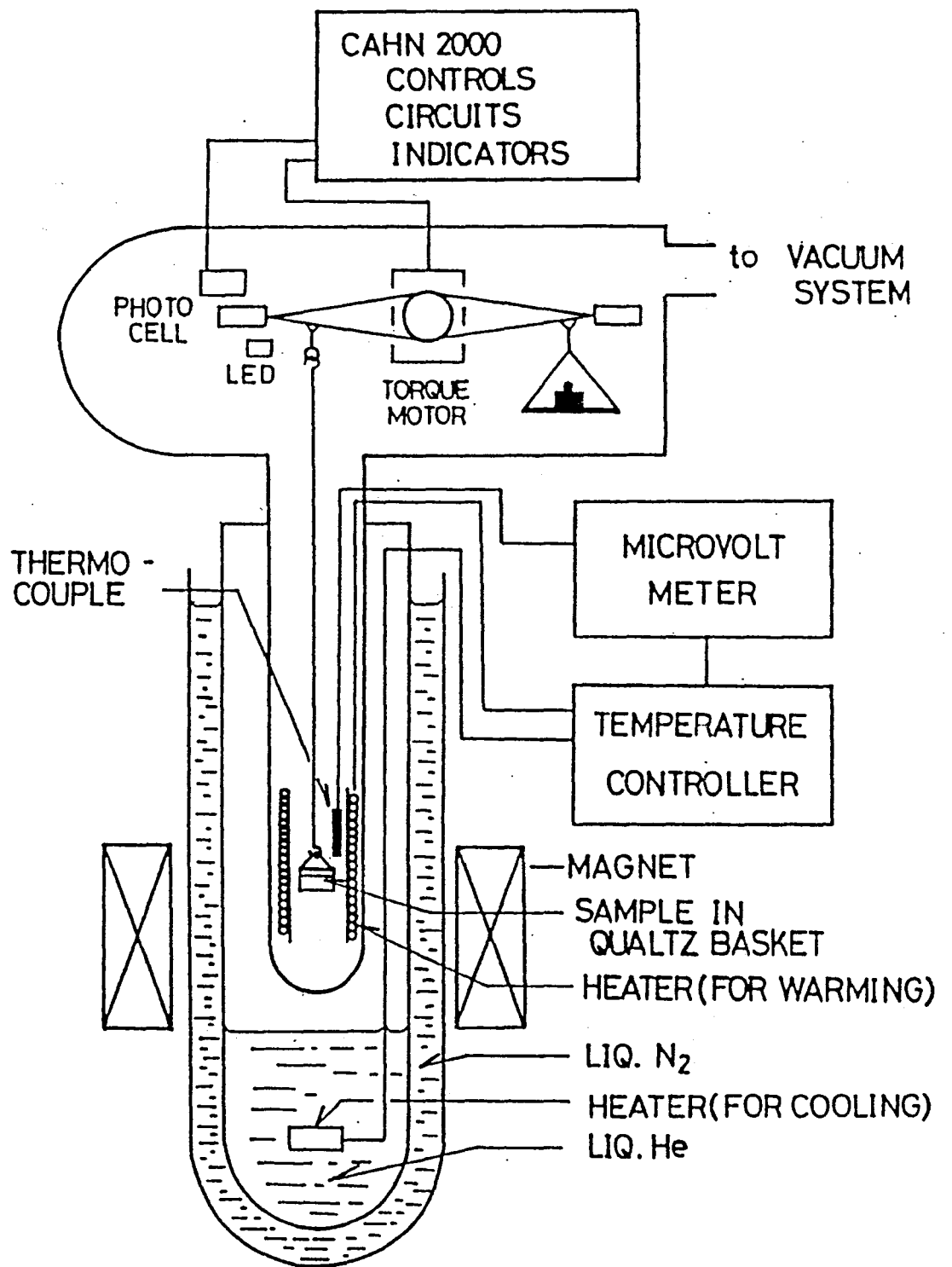


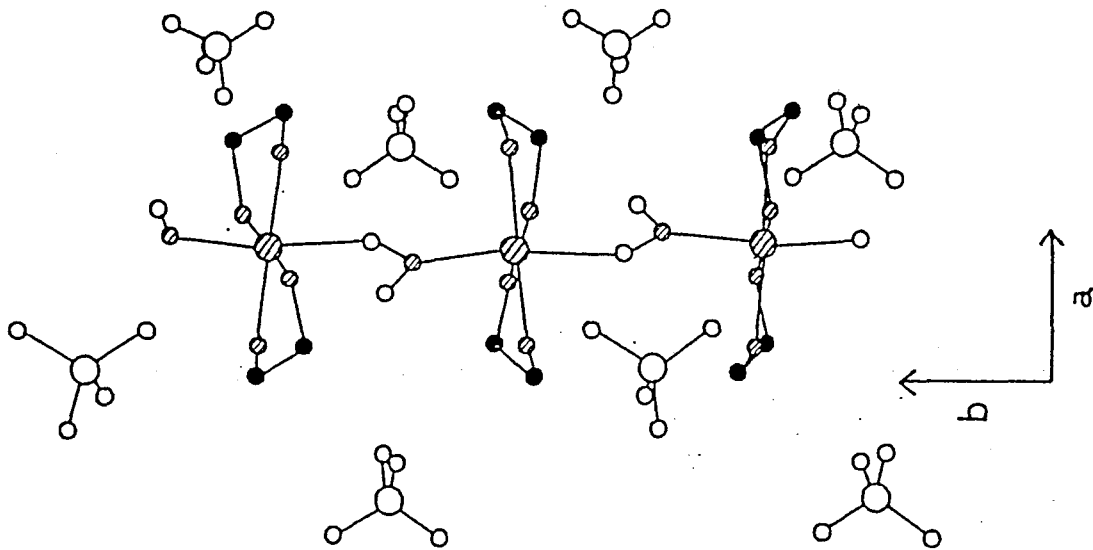
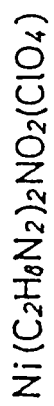
Fig. 5. Block diagram of magnetic susceptibility measurement system.

### 3. Crystal structures

#### 3-1 NENP and NINO

NENP and NINO have similar crystallographic structure with the orthorhombic symmetry.<sup>16)</sup> NENP has a space group of the  $Pn2_1a$  or  $Pnma$ , and NINO has the  $Pbn2_1$  space group. The lattice constants are  $a=15.223 \text{ \AA}$ ,  $b=10.300 \text{ \AA}$  and  $c=8.295 \text{ \AA}$  in NENP and  $a=15.384 \text{ \AA}$ ,  $b=10.590 \text{ \AA}$  and  $c=8.507 \text{ \AA}$  in NINO. In both compounds the nickel ions are located one-dimensionally along b-axis and chains of nickel ions are well separated from each other by  $ClO_4$  perchlorate anions as shown in Fig. 6.<sup>16)</sup> The nickel ions are linked by the  $NO_2$  group along the b-axis with covalent bond and each nickel ion is surrounded by four nitrogen atoms belonging to two diamine molecules. The Ni-4N plane is nearly perpendicular to the b-axis. Therefore, the nickel ion is regarded to be located at the center of a distorted nitrogen octahedron. Main structural differences is the coordination around the nickel ions, ethandiamine in NENP and 1,3-propanediamine in NINO. It can be pointed out that the change from ethandiamine in NENP to propane-diamine in NINO allows us to modify the stereochemistry of nickel ions, and therefore its anisotropy properties.

NENP



NINO

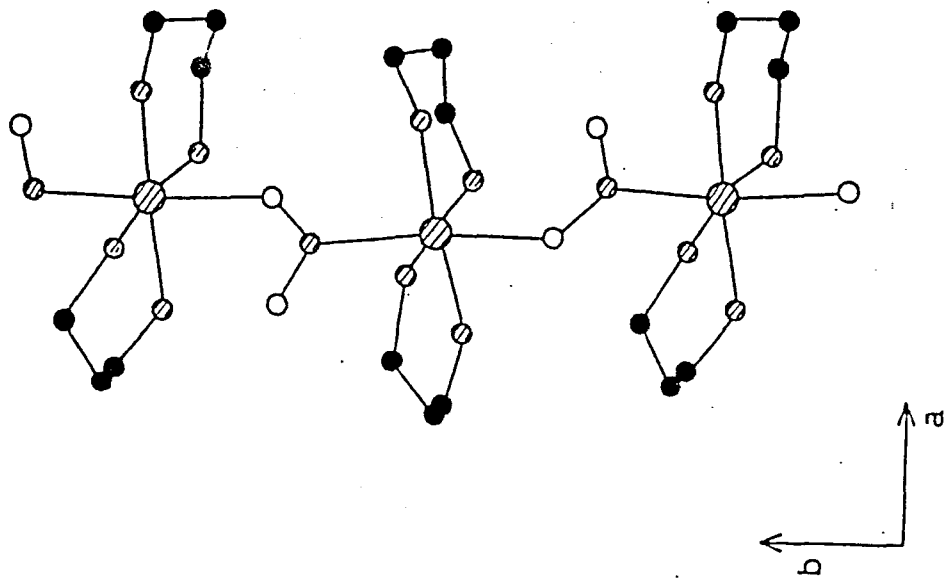


Fig. 6. Schematic view of the chain structure of NENP and NINO.

### 3-2 TMNIN

The crystal structure of TMNIN is similar to that of one-dimensional antiferromagnet TMMC((CH<sub>3</sub>)<sub>4</sub>NMnCl<sub>3</sub>). A perspective view of the structure determined by Gleizes is shown in Fig. 7.<sup>19)</sup> Lattice constants of the hexagonal structure are  $a=b=9.096(1)$  Å and  $c=7.083$  Å. Nickel ions are located along  $c$ -axis and they are bridged by three nitrite anions. The Ni-Ni distance is equal to  $c/2=3.54$  Å. This bridging mode of the nitrite anions Ni-(NO<sub>2</sub>)<sub>3</sub>-Ni is quite different from the one in NENP and NINO which have the chain structure Ni-NO<sub>2</sub>-Ni. The chains are well separated by tetramethylammonium cations.

TMNIN  
 $(\text{CH}_3)_4\text{NNi}(\text{NO}_2)_3$

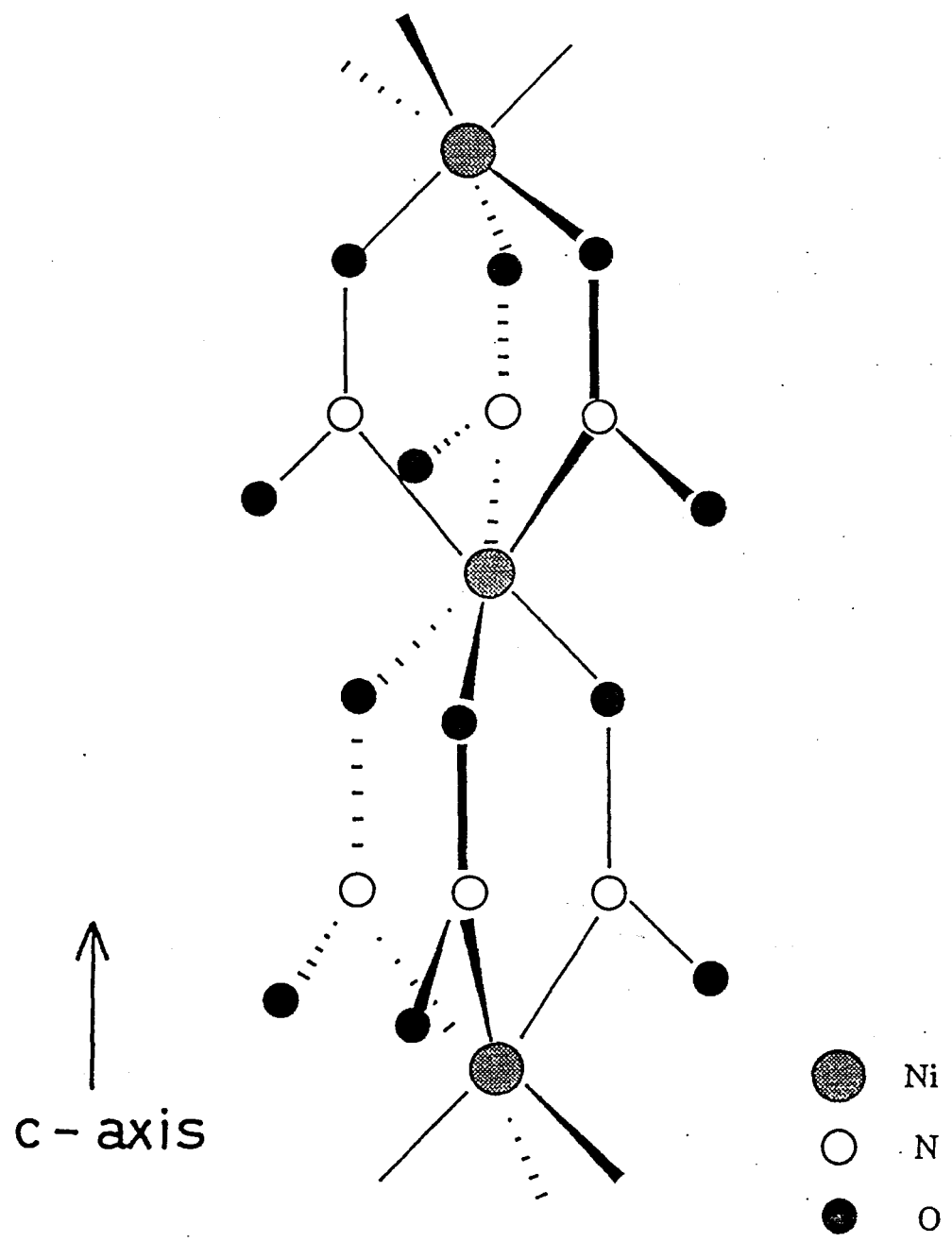


Fig. 7. Schematic view of the chain structure of TMNIN.

### 3-3 NINAZ

Figure 8 shows a schematic view of the chain structure determined by Solans.<sup>22)</sup> NINAZ crystallizes in the orthorhombic system with the lattice constants  $a=15.384 \text{ \AA}$ ,  $b=10.590 \text{ \AA}$  and  $c=8.507 \text{ \AA}$ . Chains consist of nickel cations which are bridged by azido ligand along the c-axis. These chains are well separated from each other by  $\text{ClO}_4$  ions. The Ni-Ni distance is equal to  $5.849 \text{ \AA}$ . Each Ni ion displays a distorted octahedral coordination being linked to four N of two 1,3-propanediamine ligands and two N of the two azido ligands.

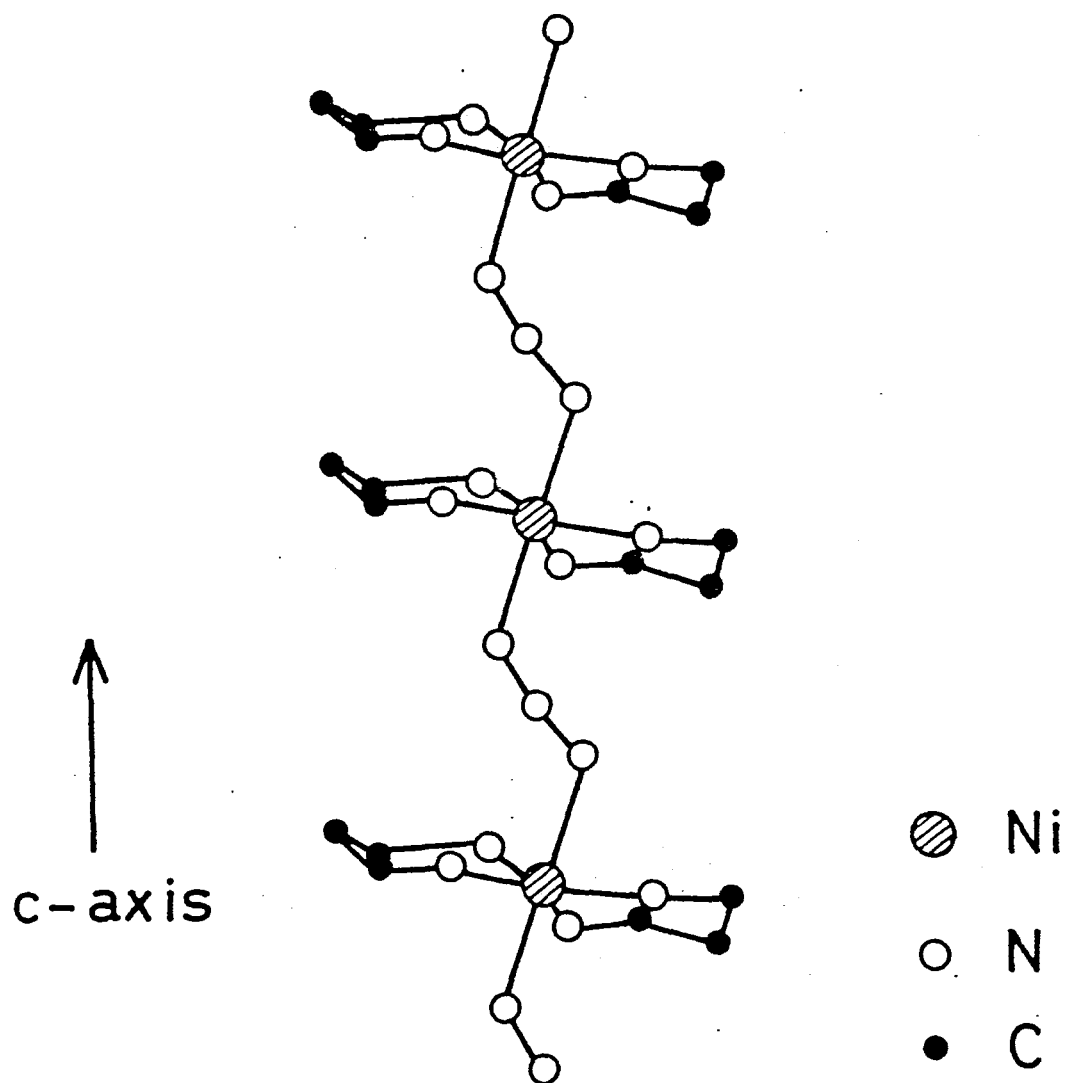
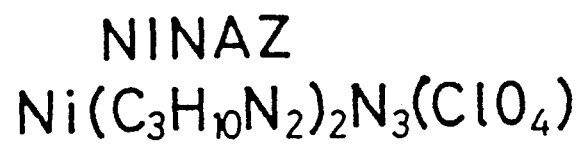


Fig. 8. Schematic view of the chain structure of NINAZ.

## 4. Magnetic properties

### 4-1 Magnetic properties of NENP and NINO

Figure 9 shows the magnetic susceptibility data of single crystal sample of NENP which are obtained by Renard et al. in the temperature range from 1.7 K to 90 K.<sup>16)</sup> The susceptibility shows a round maximum at about 60 K and an exponential decrease in low temperature region. This low temperature behavior of the susceptibility is quite different from a gapless one-dimensional Heisenberg antiferromagnet. Bonner and Fisher<sup>3)</sup> calculated the susceptibility curve of finite size linear chains of  $S=1/2$  with the anisotropic Hamiltonian. The limiting susceptibility curve has the finite value at  $T=0$  K ( $\chi(T=0)/\chi_{\max}=0.69$  for  $S=1/2$ ). At  $T=1.5$  K, still far from  $T=0$  K,  $\chi(T=1.5)/\chi_{\max} \approx 0.1$  which is much smaller than expected value for a gapless chain as shown in Fig. 9. This susceptibility behavior clearly suggests the existence of the Haldane gap. The high temperature susceptibility data are well understood by the theoretically calculated molar susceptibility for  $S=1$  one-dimensional Heisenberg antiferromagnet given by

$$\chi = \frac{N\mu_B^2 g^2}{kT} \left( \frac{2+0.0194X+0.777X^2}{3+4.346X+3.232X^2+5.834X^3} \right), \quad (3)$$

with  $X = |J|/kT$ .<sup>24)</sup> Where  $k$  is the Boltzmann constant,  $N$  the Avogadro number,  $g$  the Landé factor and  $\mu_B$  the Bohr magneton. The intrachain exchange interaction  $J$  of  $-47.5$  K and  $g$ -values with  $g_a=2.23$ ,  $g_b=2.15$  and  $g_c=2.21$  were obtained by

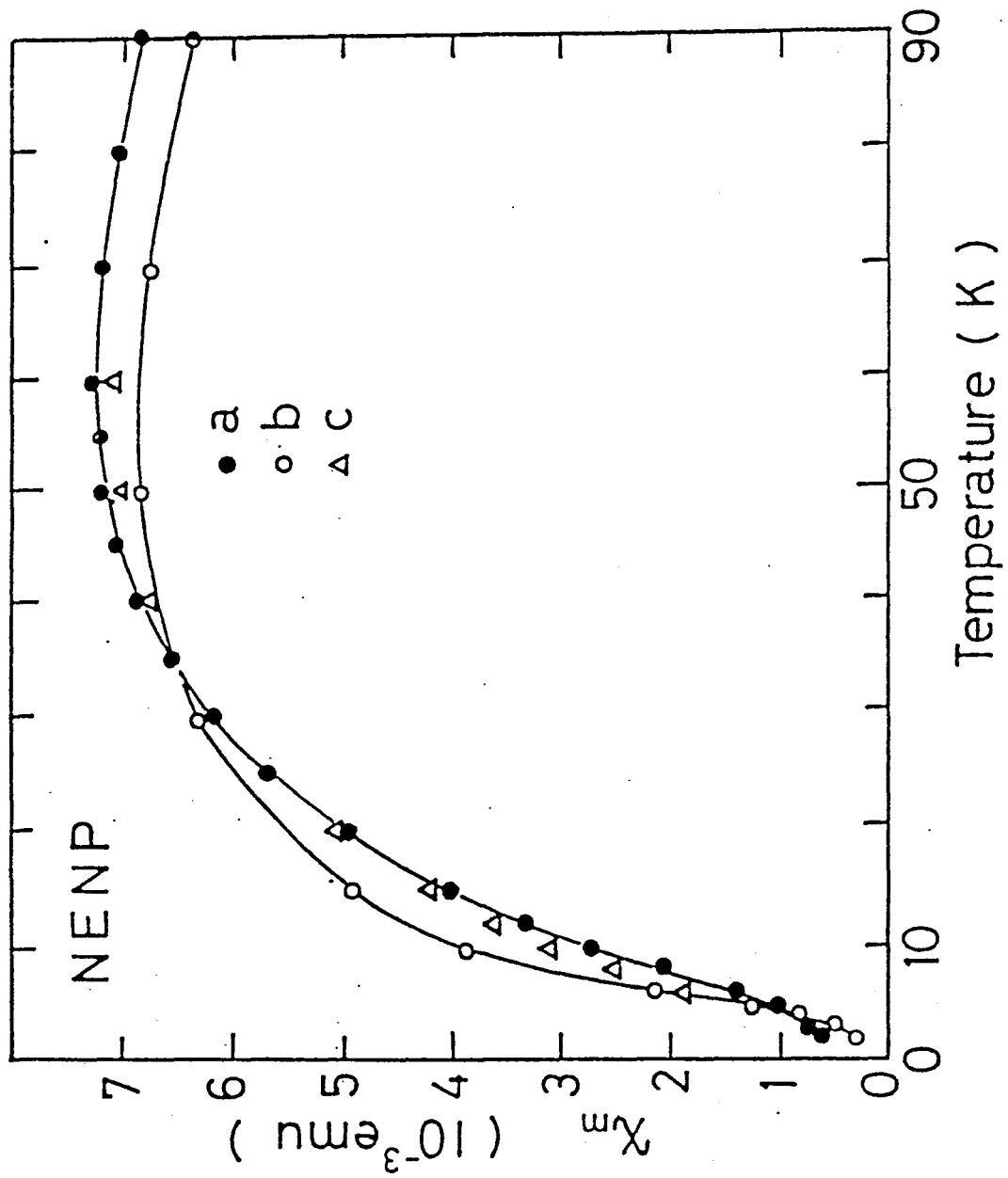


Fig. 9. Temperature dependence of the magnetic susceptibility of NENP along the three crystallographic axes. (ref.16)

Meyer et al.<sup>24)</sup> The positive uniaxial anisotropy term  $DS_z^2$  ( $D>0$ ) exists along the b-axis with an energy of 12 K.<sup>16)</sup>

The magnetic susceptibility data of single crystal samples NENP and NINO used in this experiment are shown in Fig. 10. Similar data to Fig. 9 was obtained for NENP as shown in (a). The magnetic susceptibility of NINO shows the exponential decrease at low temperatures reflecting an energy gap. The least-squares fitting of experimental data to the theoretical calculation (eq. (3)) lead to  $J=-49.9$  K and  $g_a=2.23$ ,  $g_b=2.17$  and  $g_c=2.22$ . Solid lines in Fig. 10 show the theoretical curves with good agreement with the data.

It is noted that there is a crossover in the susceptibility around 35 K in both compounds. This means that the sign of the uniaxial anisotropy changes at this temperature. Another crossover is found around 3 K as shown in Fig. 9. The origin is not clear but this feature largely depends on impurities.

Neutron scattering measurement on NENP were performed by Renard et al.<sup>16)</sup> and they have observed energy gaps near the wave vector  $q=\pi$ . The measurement of scattering in the direction of the chain gives  $E_g^{\parallel}=30$  K and, for the perpendicular direction,  $E_g^{\perp}=14$  K. These two gaps result from the splitting of the Haldane gap of the pure Heisenberg chain by uniaxial anisotropy  $D$ . The  $D$ -value is estimated to be 10 K.

Nuclear magnetic resonance measurements have been done by Gaveau et al.<sup>25)</sup> They measured the nuclear spin-lattice relaxation time  $T_1$  of protons versus temperatures. The remarkable decrease of  $1/T_1$  observed in NENP indicates a drastic reduction of the magnetic fluctuations with decreasing temperature, which

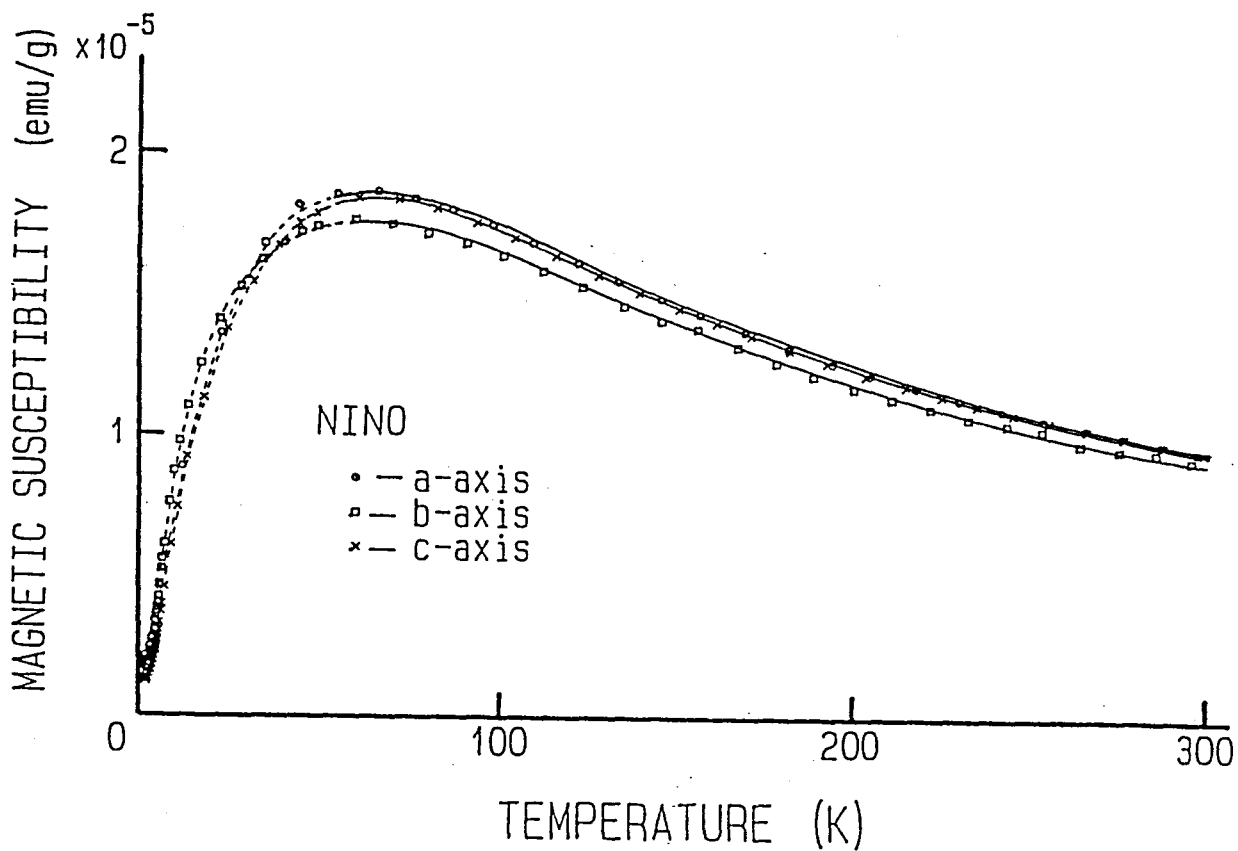
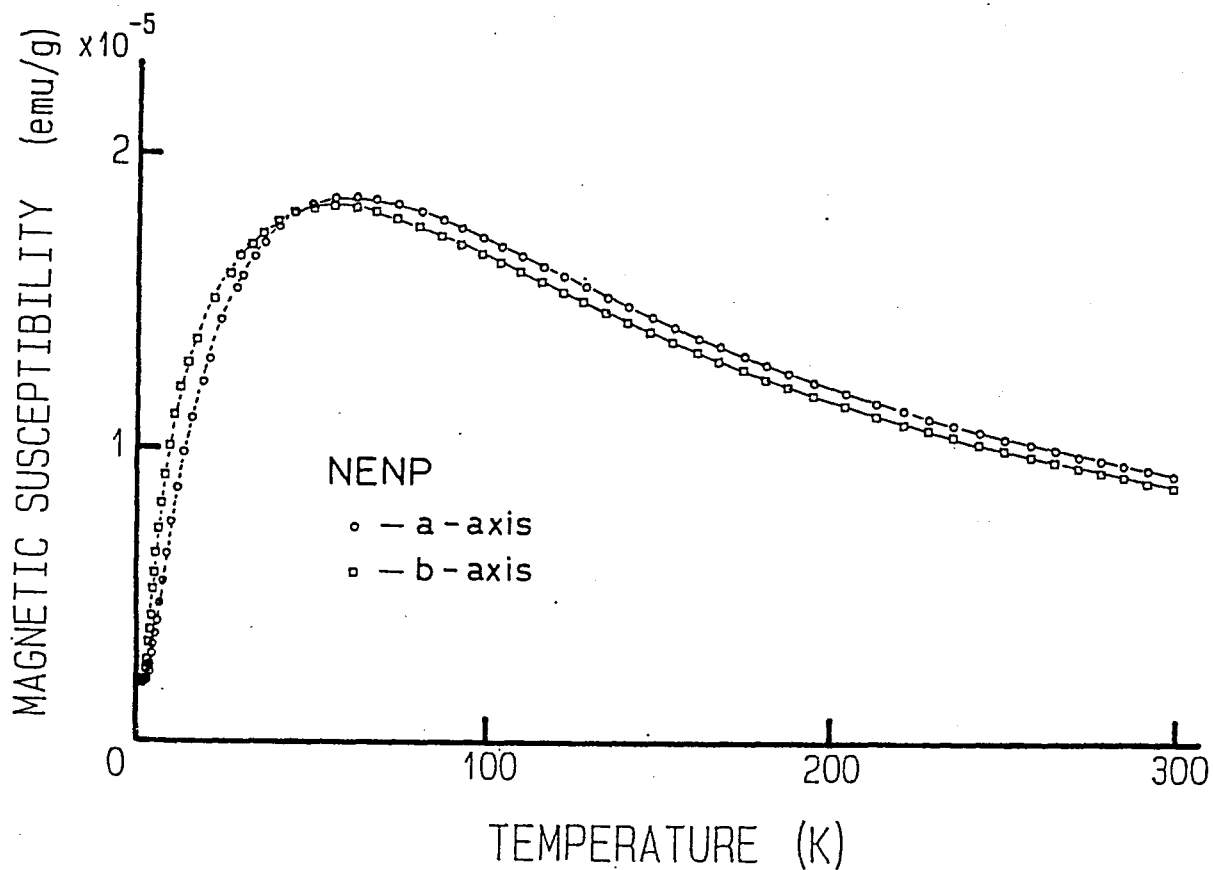


Fig.10. Temperature dependence of the magnetic susceptibility of NENP and NINO. Solid lines show the theoretical curves with good agreement with the data. Broken lines are experimental curves and show satisfactory agreement with the data in ref.16 where the axes of NINO a, b and c should be read c, a and b, respectively.

is consistent with the boson model for the excitations from ground state.<sup>9)</sup>

#### 4-2 Magnetic properties of TMNIN and NINAZ

Magnetic susceptibility datum of powdered sample of TMNIN is shown in Fig. 11. As expected for an antiferromagnetic chain, the susceptibility increases as temperature decreases and shows a round maximum at about 15 K. At the low temperature region, the susceptibility decreases exponentially. The value of  $\chi(T)/\chi_{\max}$  is estimated to be 0.4 at 4.2 K which is much smaller than expected value for gapless chain. Above 20 K, the susceptibility is well understood by the  $S=1$  one-dimensional antiferromagnetic model (eq.(3)) with  $J=-12$  K and  $g=2.25$ .<sup>19)</sup>

Gadet et al. have measured the nuclear spin-lattice relaxation time  $T_1$  of protons versus temperatures in polycrystalline TMNIN. The relaxation rate  $1/T_1$  decreases monotonously with decreasing temperature over two orders of magnitude. This behavior of the proton relaxation in TMNIN is quite different from that in  $S=5/2$  1D-AF TMMC. In TMMC,  $1/T_1$  exhibits a remarkable increase with decreasing temperature due to the antiferromagnetic short-range order. The remarkable decrease of  $1/T_1$  observed in TMNIN indicates a drastic reduction of the magnetic fluctuations with decreasing temperature.

The powder magnetic susceptibility of NINAZ exhibits a broad maximum at about 150 K indicating a strong antiferromagnetic coupling in the chain as shown in Fig. 12. At low temperatures, the susceptibility shows the Curie law dependence probably due to defects or impurities. On the other hand, after subtracting an extrinsic contribution assumed to be proportional to  $1/T$ , a resulting susceptibility shows an exponential decrease at low

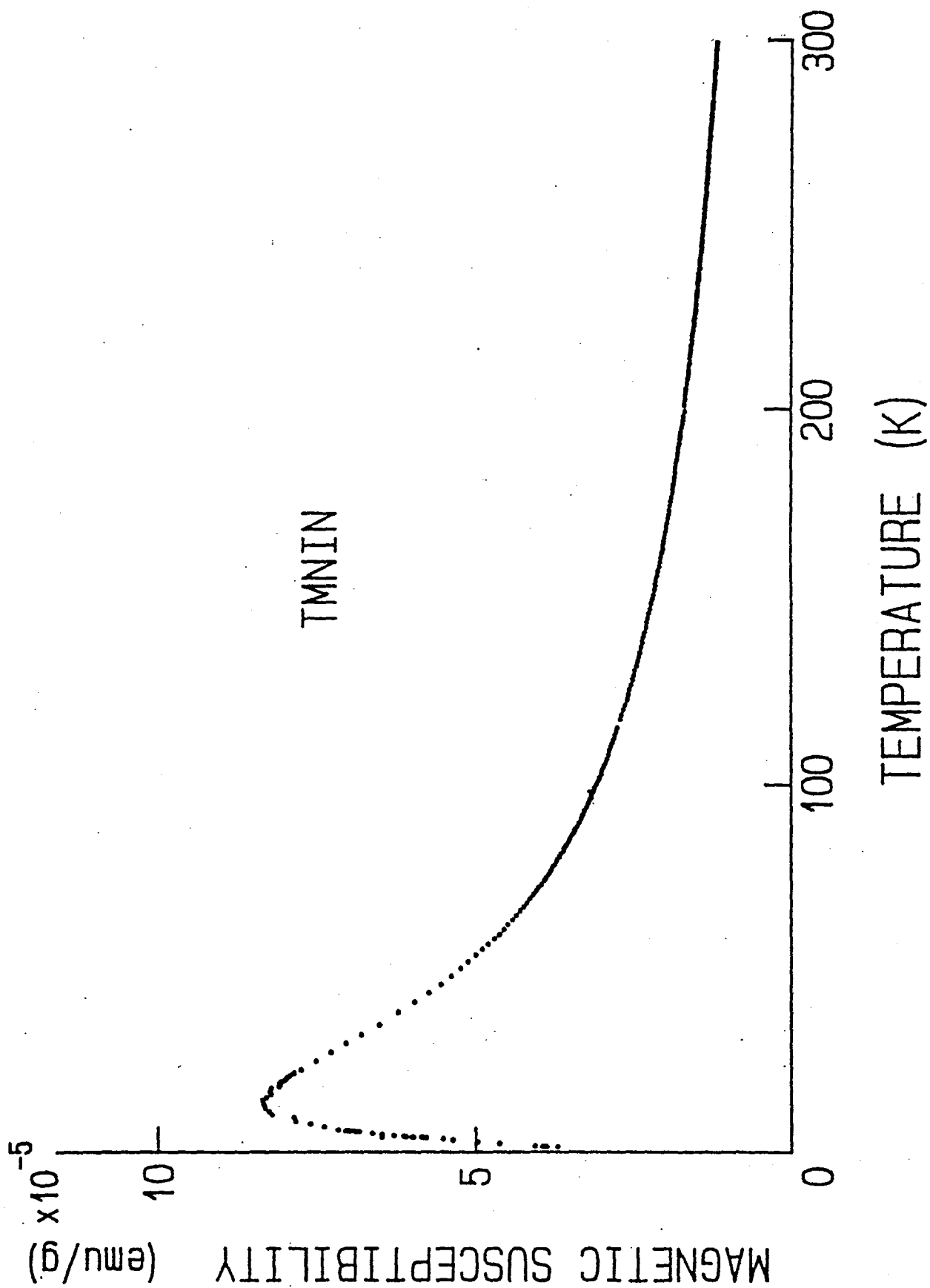


Fig.11. Temperature dependence of the magnetic susceptibility in powdered sample of TMNIN.

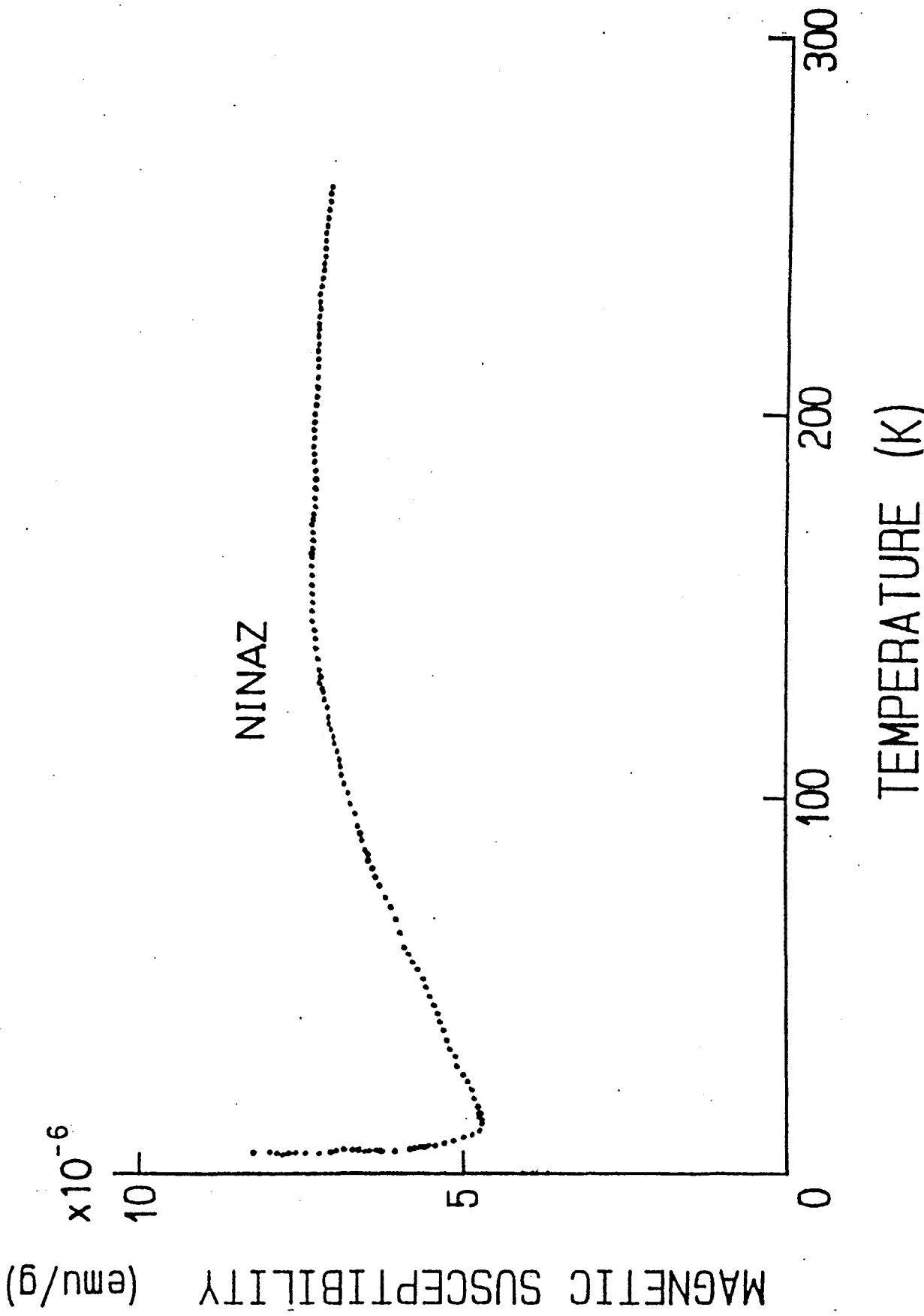


Fig.12. Temperature dependence of the magnetic susceptibility in powdered sample of NINAZ.

temperatures reflecting a clear manifestation of the Haldane gap. The high temperature data can be fitted by the theoretical susceptibility curve (eq. (3)) with  $J = -145 \pm 5$  K.<sup>25)</sup>

## 5. Experimental results and discussions

### 5-1 High field magnetization of NENP and NINO<sup>28)</sup>

The high field magnetizations of NENP<sup>26,27,28)</sup> and NINO<sup>28)</sup> along the three crystalline principal axes a, b and c at temperature 1.3 K are shown in Fig.13. The corresponding differential magnetization curves  $dM/dH$  are shown in Fig.14. No hysteresis has been observed in these curves within the experimental accuracy. A small finite magnetization in low field region along a-axis of NENP probably comes from the paramagnetic impurities. No long range magnetic order or no remarkable change in the magnetization is found at lowest temperature of 0.5 K. Noteworthy feature is that the susceptibility in low field region is almost zero and the magnetization increases sharply at each transition field for all directions of both compounds. This result clearly indicate that an energy gap exists between the singlet ground state and the first excited one and this energy gap is closed by an external magnetic field. The transition field corresponds to the crossover field from the ground state and a sublevel of the excited triplet.

There may be some explanation for the existence of the state of small net moment in low field region of magnetization in NENP and NINO. It is due to (1) the Haldane gap, (2) the existence of the dimerized state formed by exchange alternation, or (3) the existence of a singlet ground state caused by the single ion anisotropy term. The alternation is due either to a permanent distortion of the chain which leads to nonequivalent exchange paths, or to displacements of the nickel ions at low

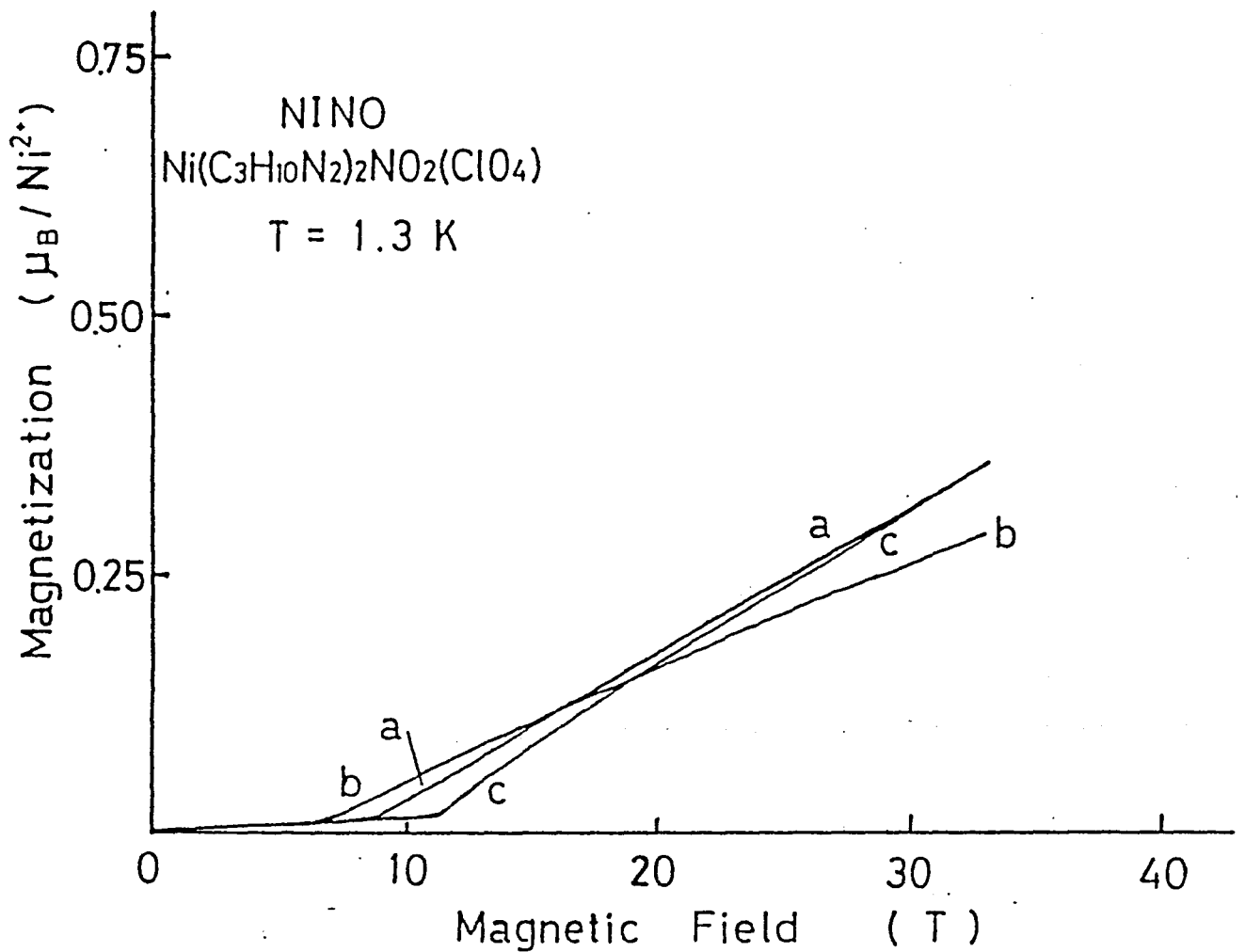
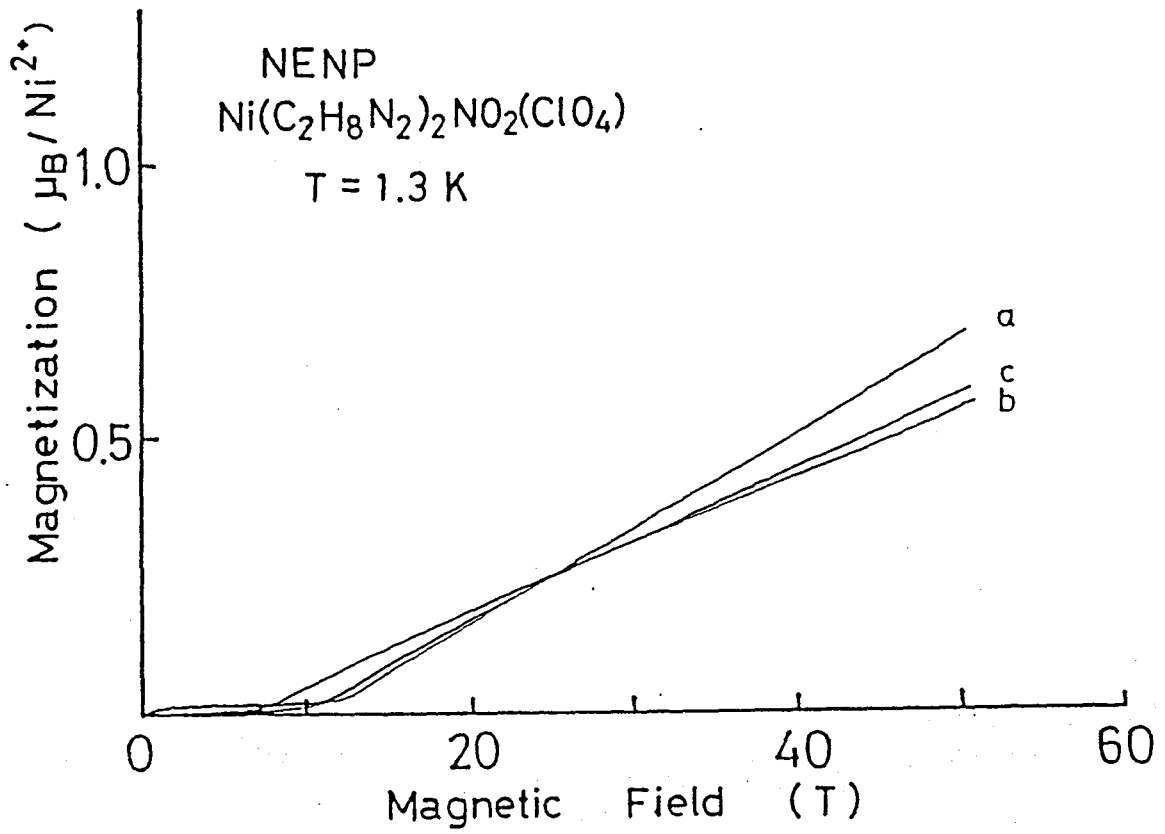


Fig.13. High field magnetization curves along the three crystallographic axes of NENP and NINO at 1.3 K.

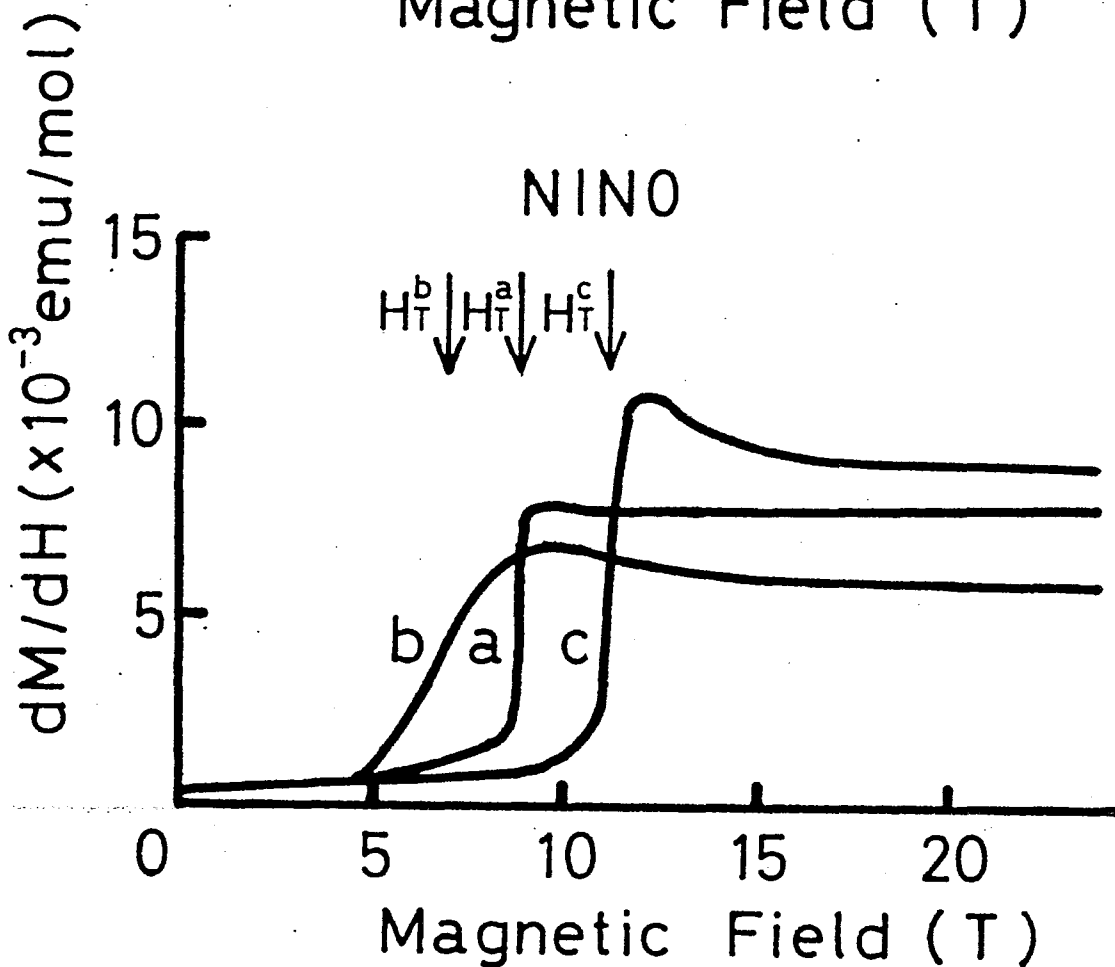
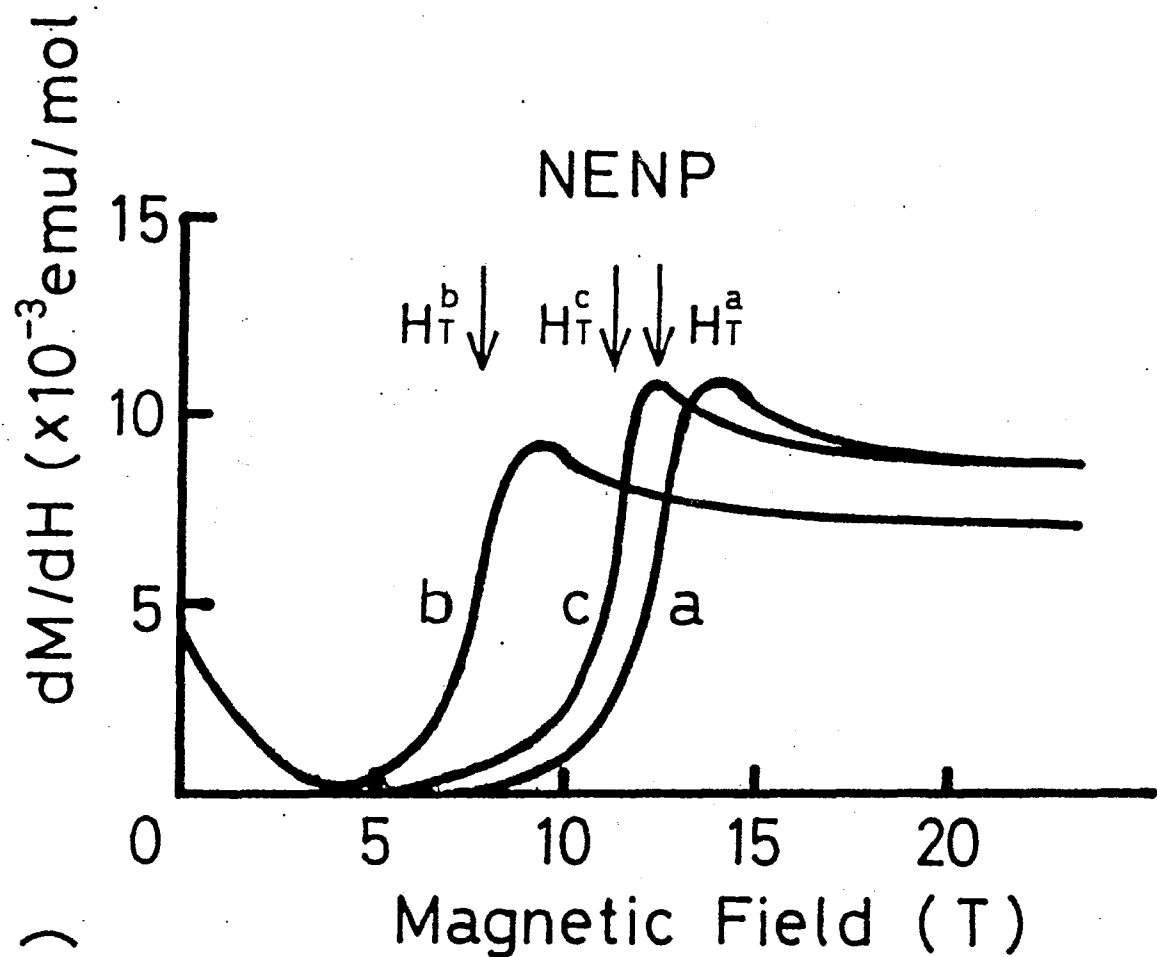


Fig.14. Field derivative curves of magnetization  $dM/dH$  in NENP and NINO.

temperature; spin pierls transition. In this case, the intra-chain exchange interaction energy  $J$  may be high sensitive to the Ni-Ni distance, since the Ni chains appear to be uniform from the crystal structure. In fact,  $J$  is fairly insensitive to the Ni-Ni distance since NENP and NINO have about the same  $J$  value, while the Ni-Ni distances differ by about  $0.1 \text{ \AA}$ . Moreover, if this alternation in the exchange interaction really happen in NENP, it can easily detected its effect, for example, on a distortion of the lattice. However, such an effect has not been observed experimentally. Therefore, we can role out the possibility of the existence of the dimerized state caused by exchange alternation.

Next, it is considered that the existence of a singlet ground state caused by a single ion anisotropy term. The ground state of an  $S=1$  system with large positive  $D$ -value is a singlet ( $S_z=0$ ) and non-magnetic. When  $H$  is applied along the quantization axis, the energy of the excited state with  $S_z=-1$  decreases with increasing field, and at a critical field, it becomes equal to that of the ground state ( $S_z=0$ ). Above this field, this system has a magnetic moment. On the other hand, when  $H$  is applied perpendicular to the quantization axis, this transition dose not happen. Instead, the magnetization gradually develops, because in this case, the crossing of the energy levels dose not occur. From the magnetization data, a sharp transition takes place for all of the principal axes. Therefore, the possibility of the singlet ground state due to the single ion anisotropy term can be rolled out. Then, it is natural to conclude that the state of small net moment observed in low field region of NENP

and NINO is formed by Haldane's mechanism.

Another important point is that the transition fields are anisotropic in both compounds as clearly seen in  $dM/dH$  curves shown in Fig.14. However,  $dM/dH$  curves have a width of about 4 T at each transition field and do not change at the lowest temperature of 0.5 K. Therefore, the transition field is defined at mid-point of  $dM/dH$  as indicated by arrows in Fig.14. The experimental data of the transition field  $H_T$  are determined as follows:  $H_T^a = 12.5$  T,  $H_T^b = 7.8$  T and  $H_T^c = 11.2$  T for NENP and  $H_T^a = 8.9$  T,  $H_T^b = 7.0$  T and  $H_T^c = 11.1$  T for NINO.

The anisotropy of transition fields are explained by assuming a truncated Hamiltonian for the excited triplet with the uniaxial and orthorhombic anisotropy term given by eq.(4). Taking the quantization axis(z-axis) parallel to the chain direction(b-axis), x-axis parallel to c-axis and y-axis parallel to a-axis and assuming that the center of the triplet is located above the ground state with the Haldane gap energy  $E_g$ , eigen energies of eq.(4) are given as follows,<sup>30)</sup>

(a)  $H//$  a-axis

$$W_1^a = E_g + (D + 3E)/3, \quad (5)$$

$$W_2^a = E_g - (D + 3E)/6 - \sqrt{((E - D)/2)^2 + g_a^2 \mu_B^2 H^2}, \quad (6)$$

$$W_3^a = E_g - (D + 3E)/6 + \sqrt{((E - D)/2)^2 + g_a^2 \mu_B^2 H^2}, \quad (7)$$

(b) H// b-axis

$$W_1^b = E_g + D/3 - \sqrt{E^2 + g_b^2 \mu_B^2 H^2}, \quad (8)$$

$$W_2^b = E_g + D/3 + \sqrt{E^2 + g_b^2 \mu_B^2 H^2}, \quad (9)$$

$$W_3^b = E_g - 2D/3, \quad (10)$$

(c) H// c-axis

$$W_1^c = E_g - (D - 3E)/6 - \sqrt{((D + E)/2)^2 + g_c^2 \mu_B^2 H^2}, \quad (11)$$

$$W_2^c = E_g + (D - 3E)/3, \quad (12)$$

$$W_3^c = E_g - (D - 3E)/6 + \sqrt{((D + E)/2)^2 + g_c^2 \mu_B^2 H^2}. \quad (13)$$

The energy  $W_2^a$ ,  $W_1^b$  and  $W_1^c$  decrease as the magnetic field increases and become zero at the transition field  $H_T$ . The transition field for each direction is given by

$$H_T^a = \sqrt{(E_g - 2D/3)(E_g + D/3 - E)} / g_a \mu_B, \quad (14)$$

$$H_T^b = \sqrt{(E_g + D/3 + E)(E_g + D/3 - E)} / g_b \mu_B, \quad (15)$$

$$H_T^c = \sqrt{(E_g - 2D/3)(E_g + D/3 + E)} / g_c \mu_B. \quad (16)$$

The Haldane energy gap  $E_g$  and field crystalline constants  $D$  and  $E$  are obtained by solving the eq. (14)-(16) using experimental data  $H_T$ . The obtained parameters  $E_g$ ,  $D$  and  $E$  and intrachain exchange energy  $J$  and  $g$ -values of NENP and NINO are listed in

	NENP	NINO
J (K)	-47.5 *	-49.9
$g_a$	2.23 *	2.23
$g_b$	2.15 *	2.17
$g_c$	2.21 *	2.22
Eg (K)	16.8	14.2
D (K)	-16.1	-11.5
E (K)	-1.3	2.1

(\* Meyer et al.: Ref.24)

Table I. Magnetic parameters of NENP and NINO.

Table 1. Recently, W Lu et al. <sup>31)</sup> have done far-infrared spectroscopy of NENP in high magnetic field and determined the energy gap  $E_G=17$  K and field crystalline constants  $D=-14$  K and  $E=-0.72$  K for the excited triplet. These values obtained here are in good agreement with their results. Figure 15 shows the energy levels at zero magnetic field and Zeeman splitting of each level. The parameters are those for NENP. The Haldane ground state is shown by zero-energy line and the excited triplet at  $E_G$  splits by  $D$  and  $E$  terms into three singlets at zero magnetic field. One of these levels decreases as the field increases and crosses with the Haldane ground state at  $H_T$ . Therefore, the Haldane ground state is broken at this field and normal antiferromagnetic state appears.

The important point of these results is that the sign of  $D$  in the excited triplet is negative while the sign in the ground state is positive. This discrepancy are explained by a new model of elementary excitation in the Haldane state proposed by Data and Kindo.<sup>18)</sup> They considered the exchange-coupled  $S=1$  spin pair (two-spin-bound state) with positive  $D$  for each spin. The model Hamiltonian is given by

$$H=g\mu_B H(S_1 + S_2) + D(S_{1z}^2 + S_{2z}^2 - 2S(S+1)/3) - 2JS_1S_2. \quad (16)$$

The energy levels are obtained by solving a 9x9 determinant and the diagram for  $H=0$  is shown in Fig.16. For comparison, single-spin levels with the same  $D$ -value are also shown on the left-hand side. The sign of effective  $D$ -value in the triplet of spin-pair

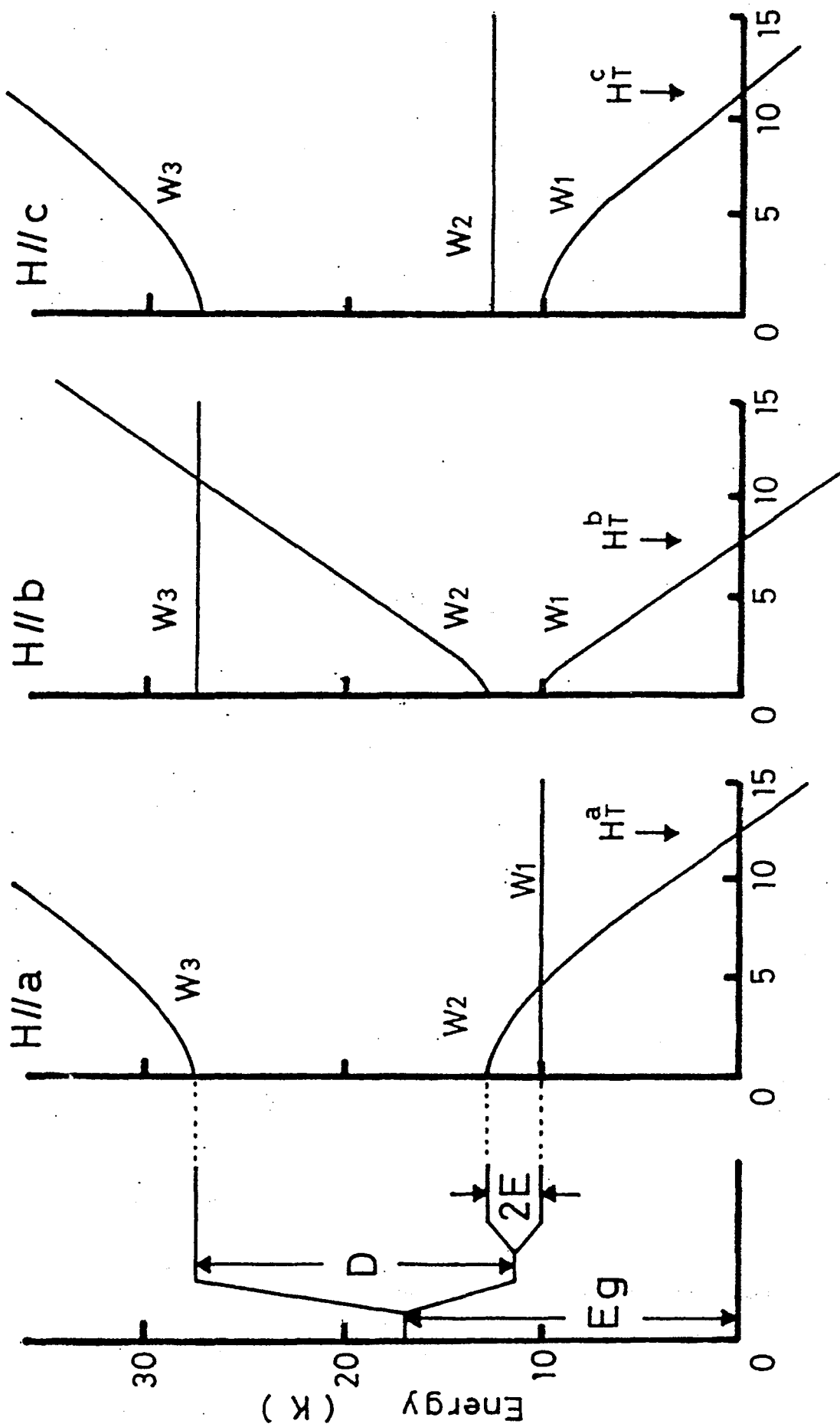


Fig.15. Energy level diagrams of NENP under magnetic field along the three crystallographic axes.

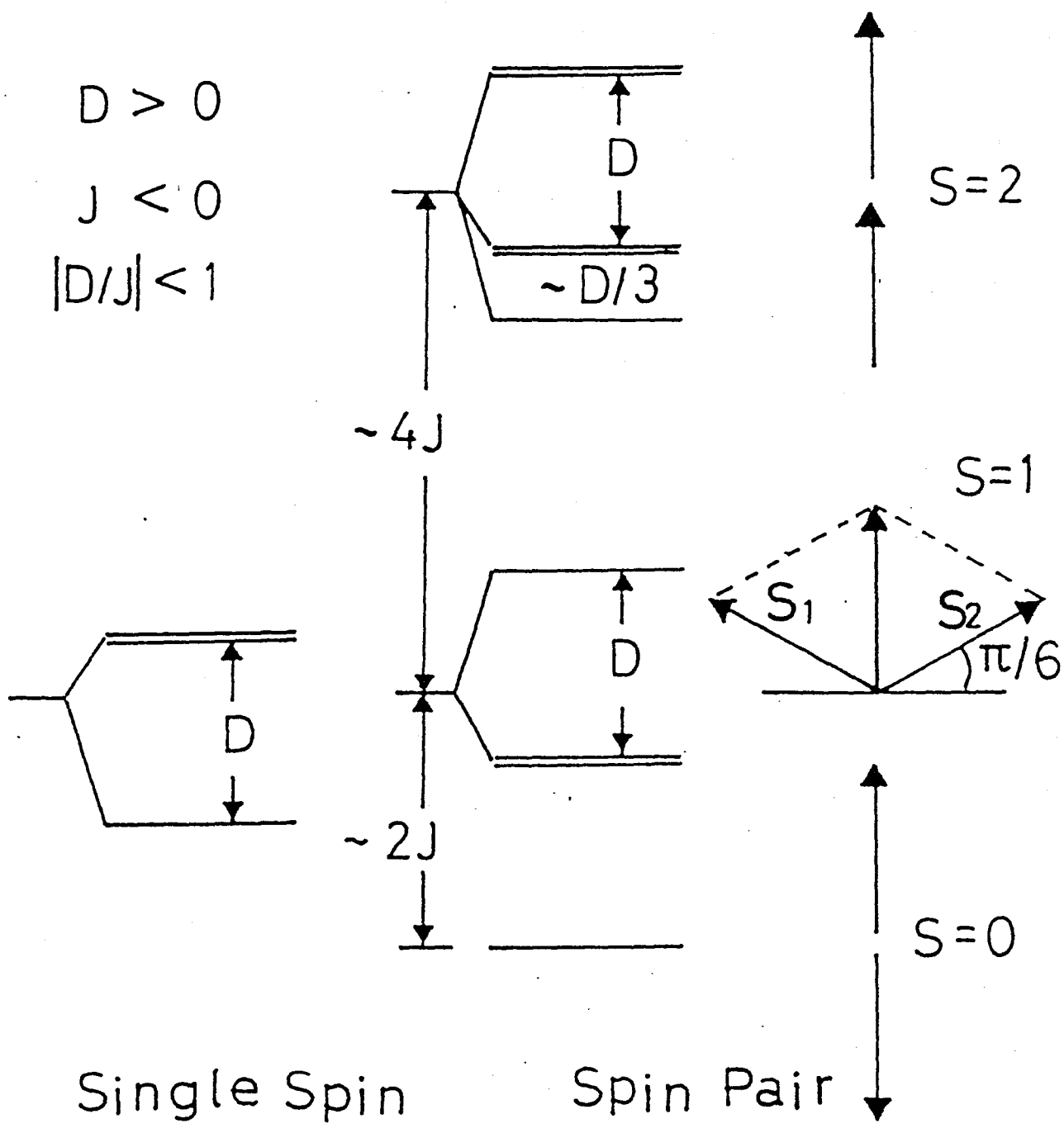
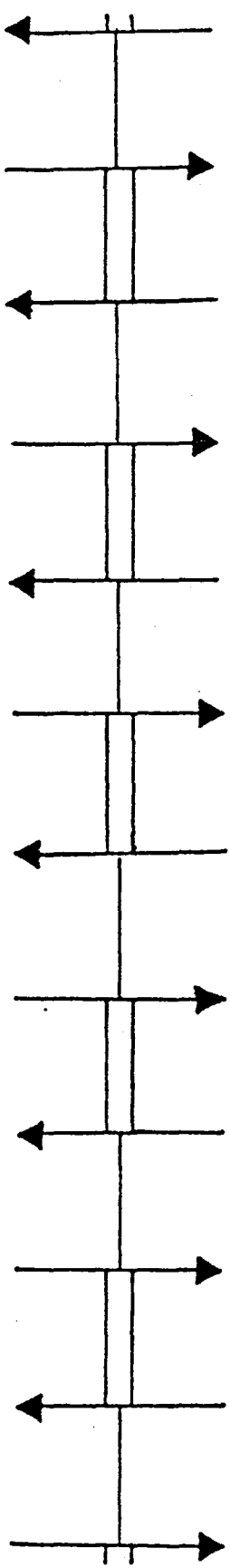


Fig.16. Energy level splittings for single-spin and spin-pair states.

model is negative and has the same magnitude to the D-value in single spin. The physical reason is qualitatively understood by the vector model on the right-hand side of Fig.16. When the resultant spin  $S=1$  points in the z-direction, the main components of  $S_1$  and  $S_2$  are perpendicular to the z-direction so that the effective D-value for the excited triplet with the resultant spin  $S=1$  is negative opposed to that of single spin. Figure 17 shows the vector model of the excited triplet. The Haldane state is schematically given by (a) and the localized two-spin-bound state with the resultant spin  $S=1$  is shown in (b) by a dotted square on the chain. No long tail of the spin-packet is expected because the spin-packet reduces the magnitude of the D-value, which is close to that of the ground state.

Parkinson and Bonner<sup>6)</sup> have done numerical studies on finite-size Heisenberg antiferromagnetic chain. They obtained the magnetization curve for  $S=1$  one-dimensional Heisenberg antiferromagnet at  $T=0$  as shown in Fig.18. This curve is not accurate in low field region where the extrapolation is not completed. Figure 19 shows the comparison of the experimental magnetization curve (solid lines) with the theoretical one (broken lines). The agreement is satisfactory in the high field region above the transition field. The fitting parameters  $|J|=47.5$  K and  $g=2.2$  and  $|J|=49.9$  K and  $g=2.2$  are used for NENP and NINO, respectively. These values of intrachain exchange energy and g-value are in good agreement with those determined from susceptibility measurements.

(a)



(b)

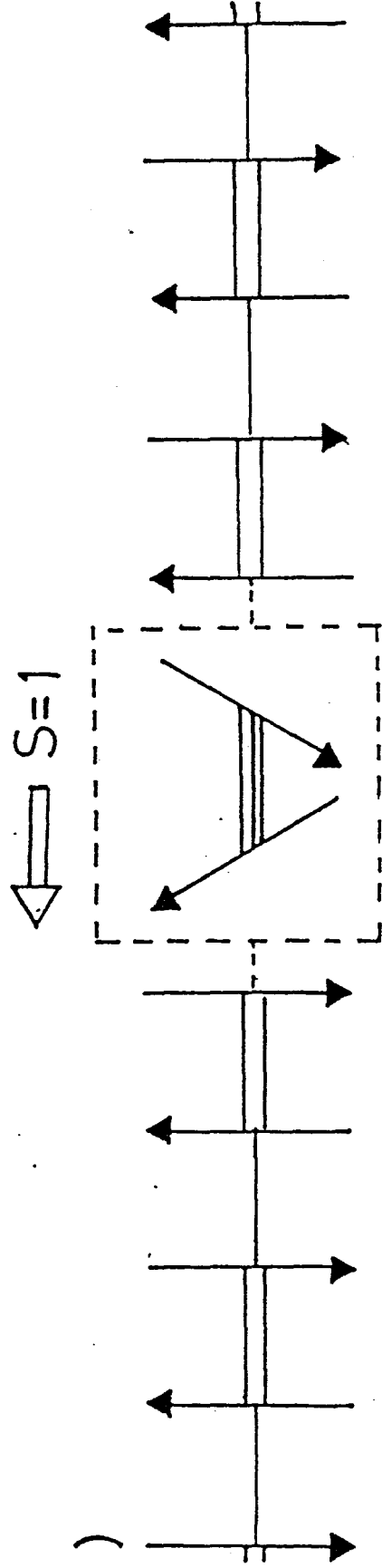


Fig.17. Model scheme of the excited two-spin bound state with the resultant spin  $S=1$ .

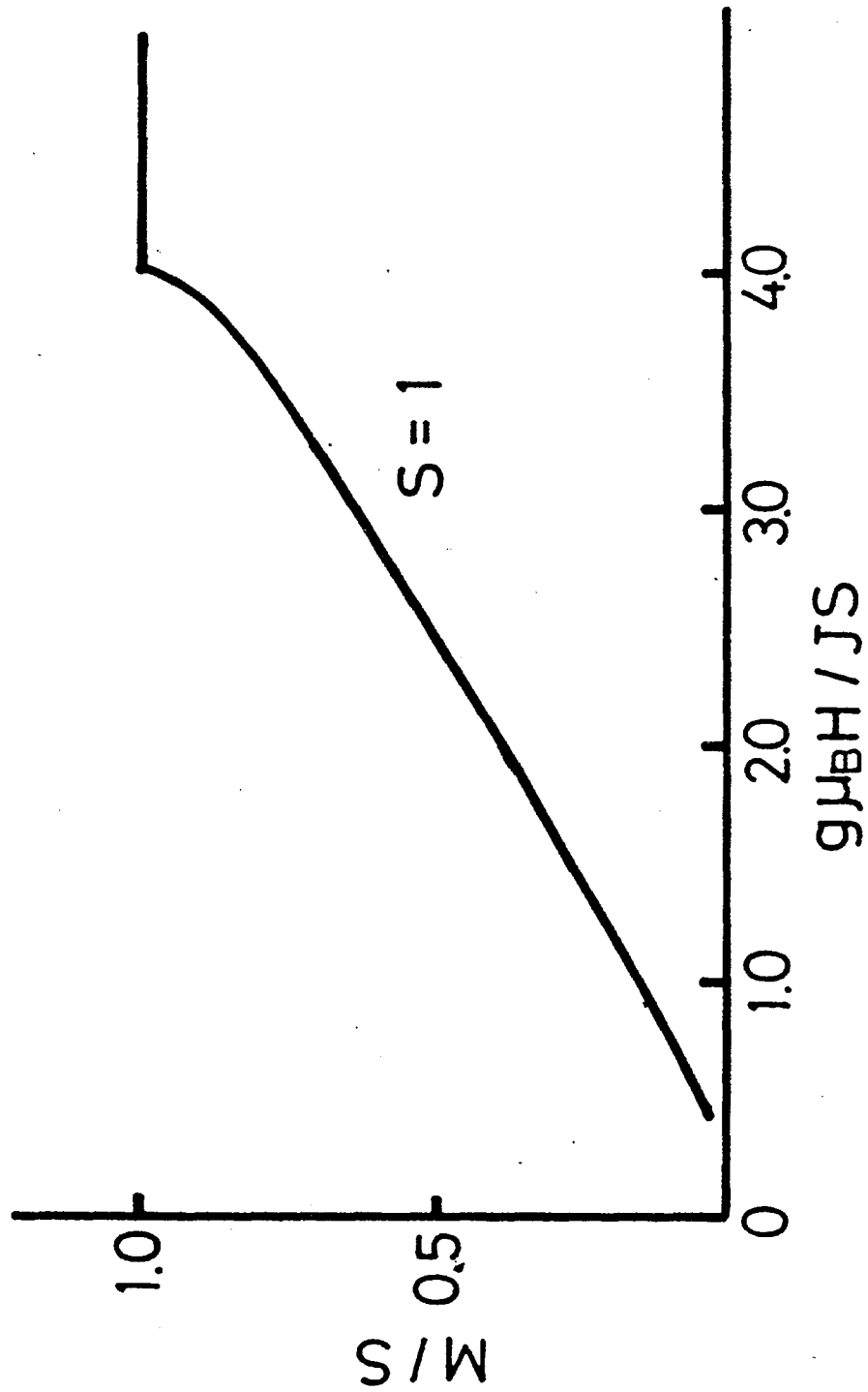


Fig.18. Extrapolated magnetization isotherm for Heisenberg anti-ferromagnetic chains with  $S=1$  at  $T=0$  K. (ref.6)

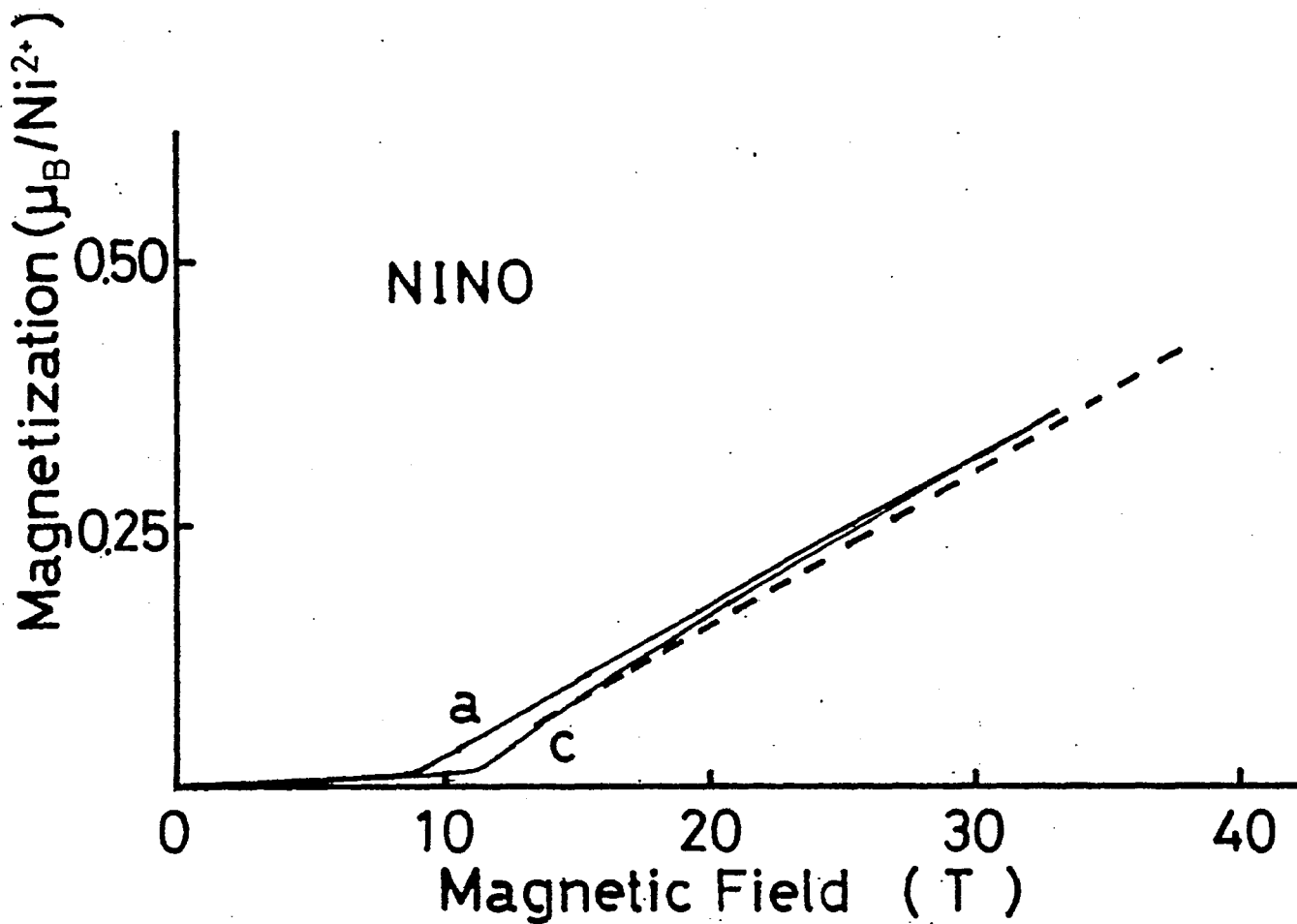
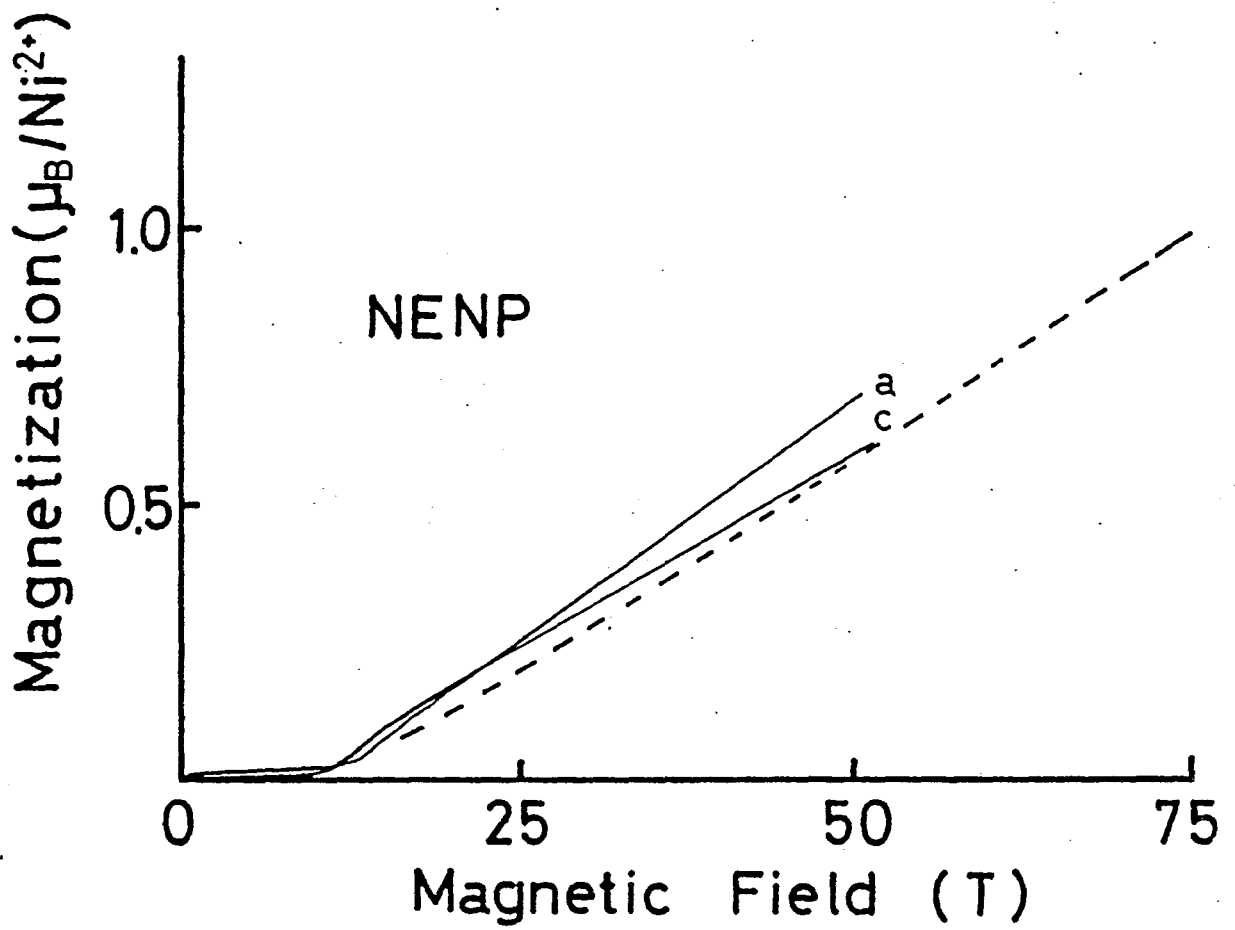


Fig.19. Comparison of the experimental magnetization curves in NENP and NINO with the theoretical curve.  $J=-47.5$  K and  $g=2.2$  in NENP and  $J=-49.9$  K and  $g=2.2$  in NINO are used.

## 5-2 High field magnetization of TMNIN and NINAZ<sup>32)</sup>

Magnetization curves of a powdered sample of TMNIN( $(\text{CH}_3)_4\text{NNi}(\text{NO}_2)_3$ ) up to 4 T at various temperatures are shown in Fig.20. The magnetization is almost linear at 4.2 K but a clear change in the magnetization is found at 0.55 K. The magnetization profile at 0.55 K can be understood by the Haldane gap model as in NENP and NINO. The sudden increase of magnetization around 2.5 T corresponds to the crossover from the nonmagnetic ground state to a sublevel of the excited triplet.

The high field magnetization up to 40 T is shown in Fig.21. The whole magnetization profile of TMNIN is similar to that of one-dimensional Heisenberg antiferromagnet with  $S=1/2$  without the low field region where TMNIN shows the clear evidence of the Haldane gap. The magnetic saturation is found above 30 T and the corresponding theoretical curve for  $S=1$  one-dimensional Heisenberg antiferromagnet given by Parkinson and Bonnar<sup>6)</sup> is shown by a dotted line with the parameters of  $|J|=12$  K and  $g=2.25$ . The agreement is satisfactory without the low field region where the theoretical calculation is not completed. The field derivative of magnetization curve  $dM/dH$  is shown in Fig.22. Sakai and Takahashi have done numerical diagonalizations up to  $N=16$  on the  $S=1$  one-dimensional Heisenberg antiferromagnet.<sup>12)</sup> They obtained the magnetization curve and the field derivative of magnetization curve  $dM/dH$  at thermodynamic limit which indicate an anomaly at  $H_T$ . This theoretical

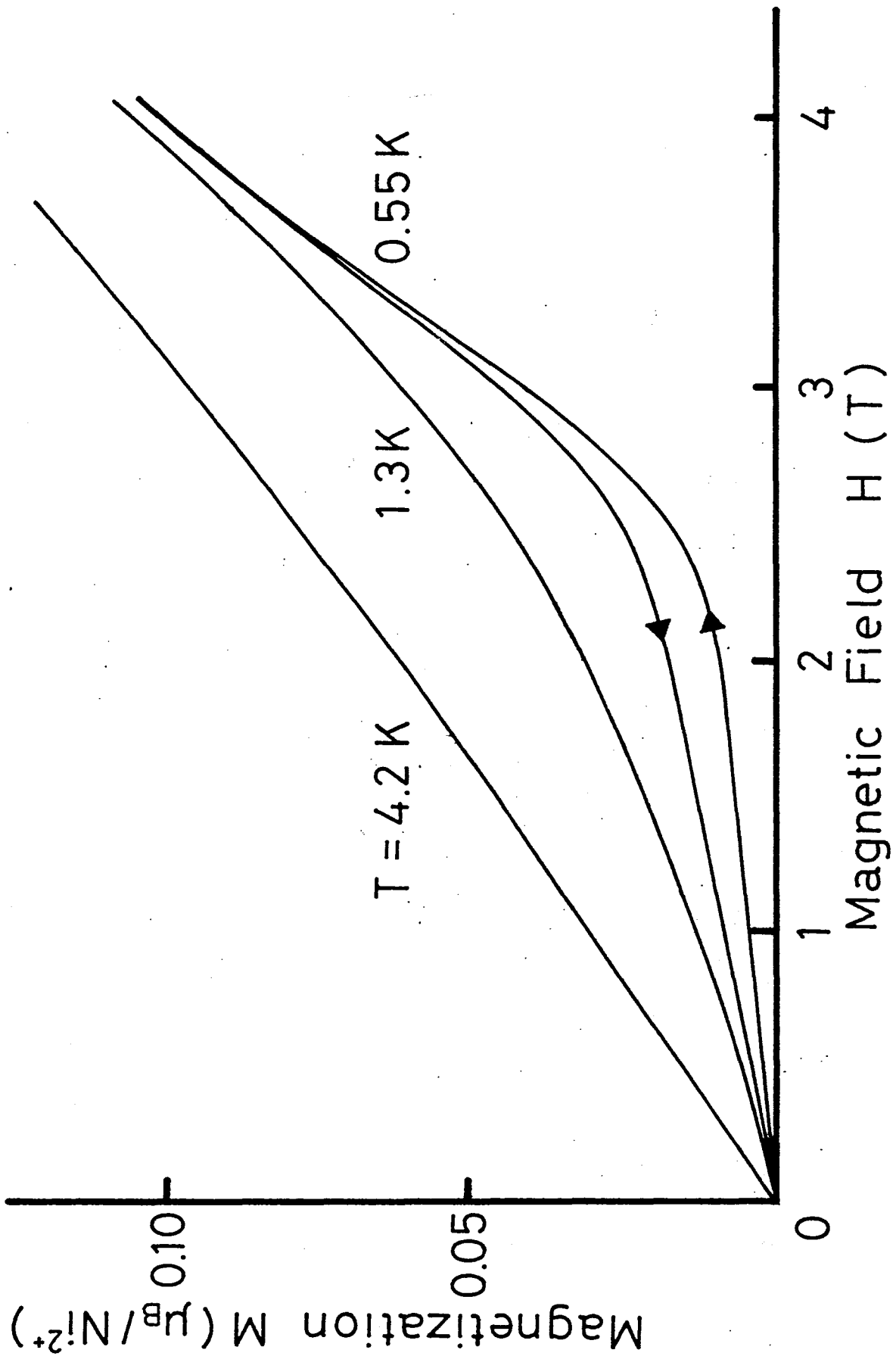


Fig.20. Magnetization of TMNIN in pulsed magnetic field up to 4 T at various temperatures.

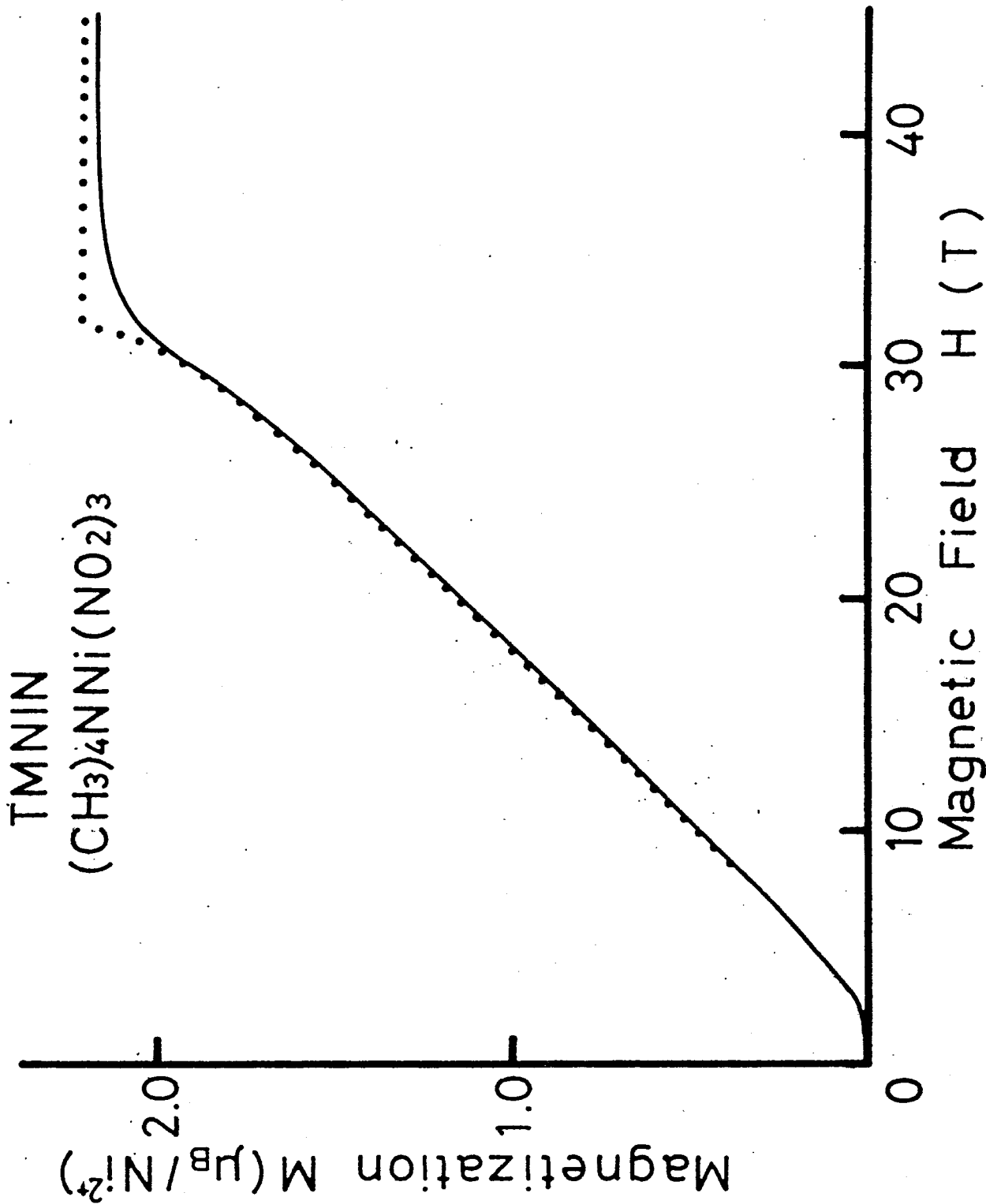


Fig. 21. High field magnetization curve of TMNIN at 0.55 K. Dotted line shows the theoretical curve given by ref. 6 with the parameters  $J=-12$  K and  $g=2.25$ .

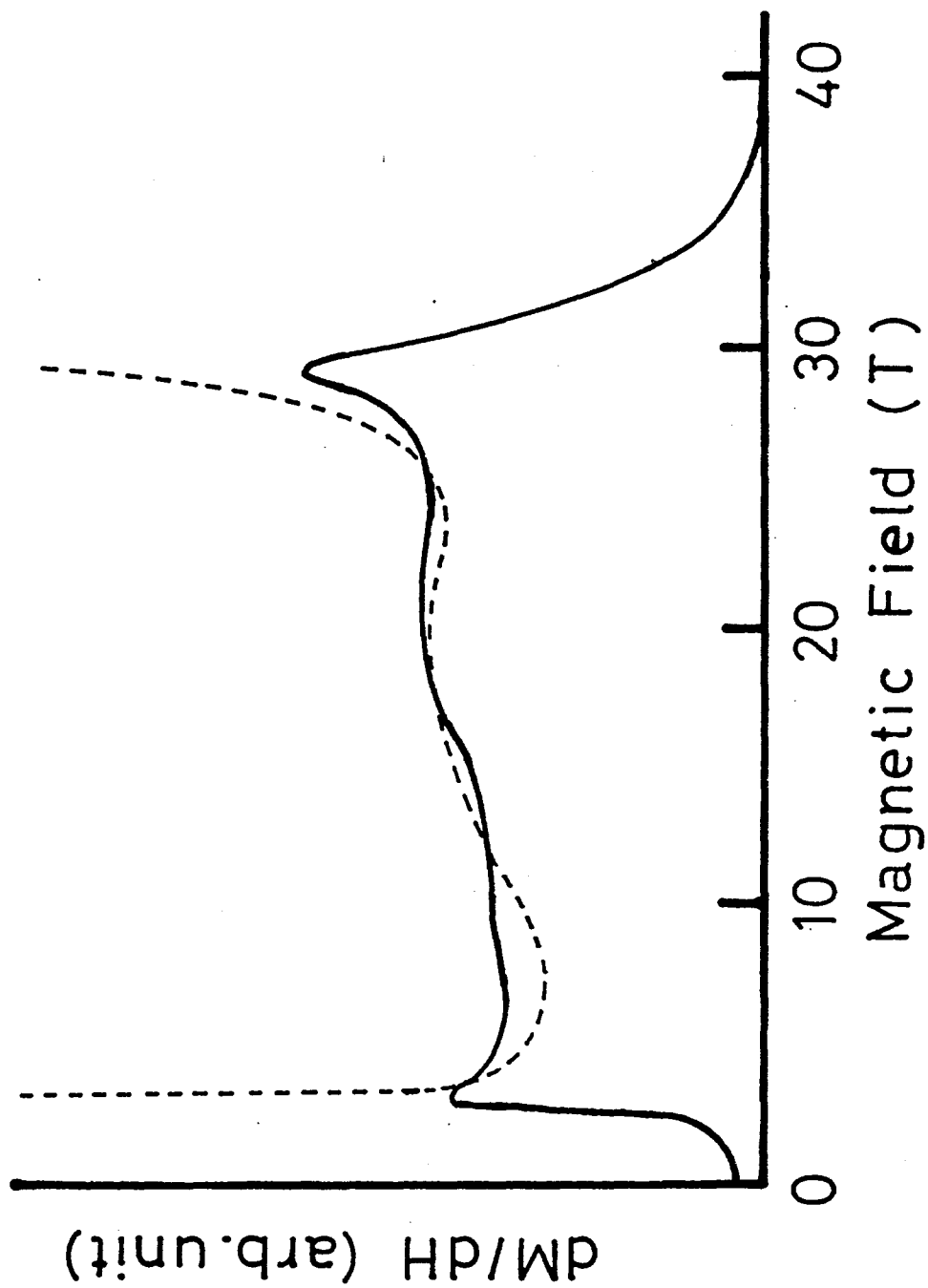


Fig.22. Field derivative of magnetization curve  $dM/dH$  of TMNIN. Broken line is the theoretical curve given by Sakai and Takahashi. (ref.12)

$dM/dH$  curve given by Sakai and Takahashi is also shown in Fig.22 by a broken line. The experimental curve is nicely in accord with the theory. Therefore, it is concluded that TMNIN has the nature of ideal  $S=1$  one-dimensional Heisenberg antiferromagnet. The transition field is defined as 2.7 T from the  $dM/dH$  curve and the corresponding energy gap  $E_g = g\mu_B H_T$  is estimated to be 4.1 K.

Figure 23 shows the high field magnetization of powdered sample of NINAZ at 1.3 K. A small parasitic magnetization in low field region probably comes from defects or impurities. The increase of magnetization which indicates the Haldane gap quenching appears at the transition field  $H_T=30$  T. The  $g$ -value of NINAZ is not known, therefore we use  $g=2.20$  as the average value for  $Ni^{2+}$  ion in Haldane gap materials. The large Haldane gap  $E_g=44.3$  K is obtained reflecting the large intrachain exchange energy.

TMNIN can be regarded as the ideal Heisenberg system, because this compound has very small anisotropy<sup>19)</sup> and the obtained magnetization and field derivative of magnetization are nicely in accord with the theory. Therefore, the energy gap of TMNIN determined here is considered to be close to the real Haldane gap. On the other hand, NINAZ may have relatively large anisotropy as is in NENP and NINO. So that the energy gap of NINAZ obtained from the magnetization of powdered sample may be slightly smaller than that will be obtained from single crystal sample.

The obtained relations between the Haldane gap energy  $E_g$  and the intrachain exchange energy  $J$  of NENP ( $E_g=0.35|J|$ ),

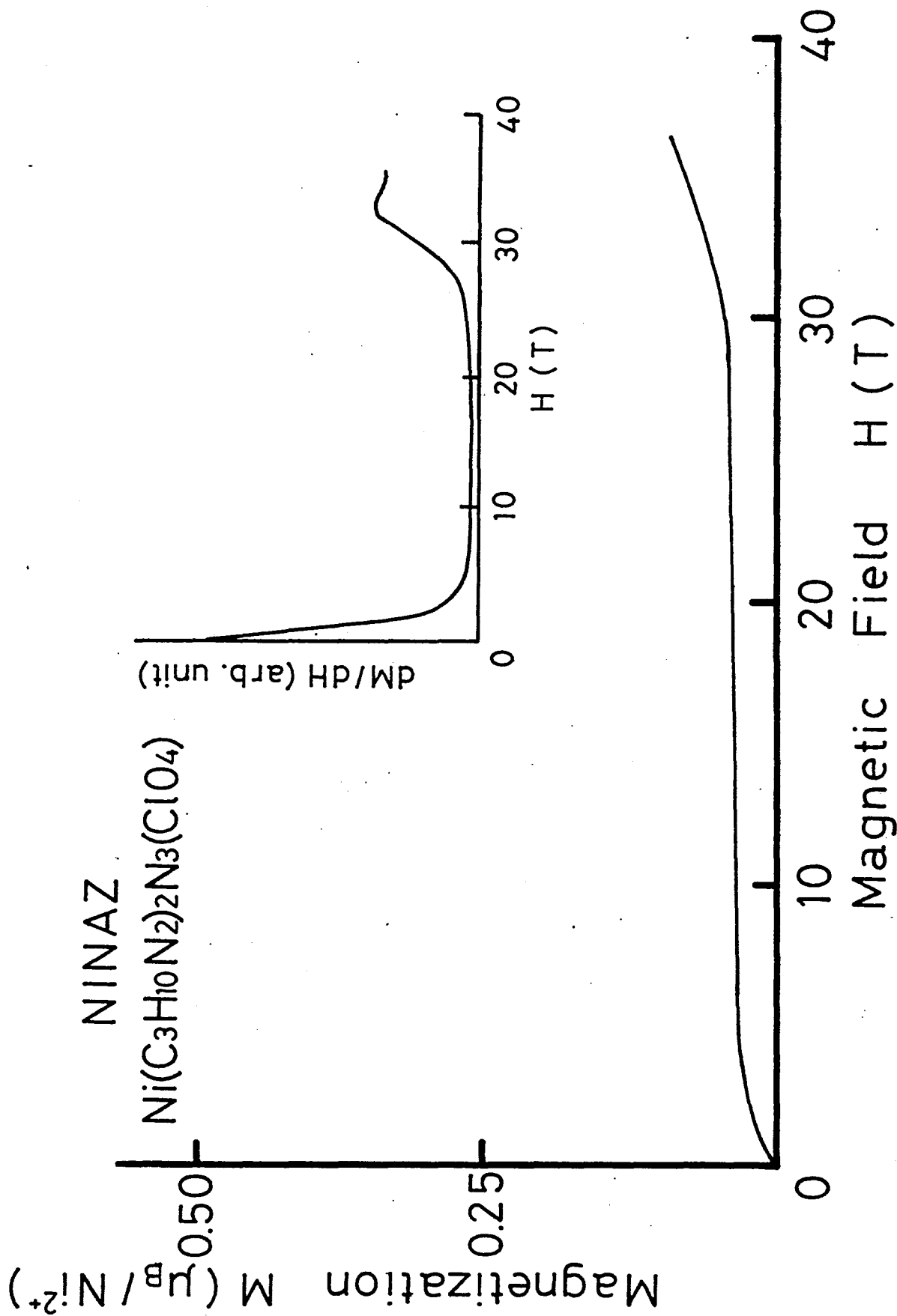


Fig.23. High field magnetization and  $\text{dM/dH}$  curve of NINAZ at 1.3 K.

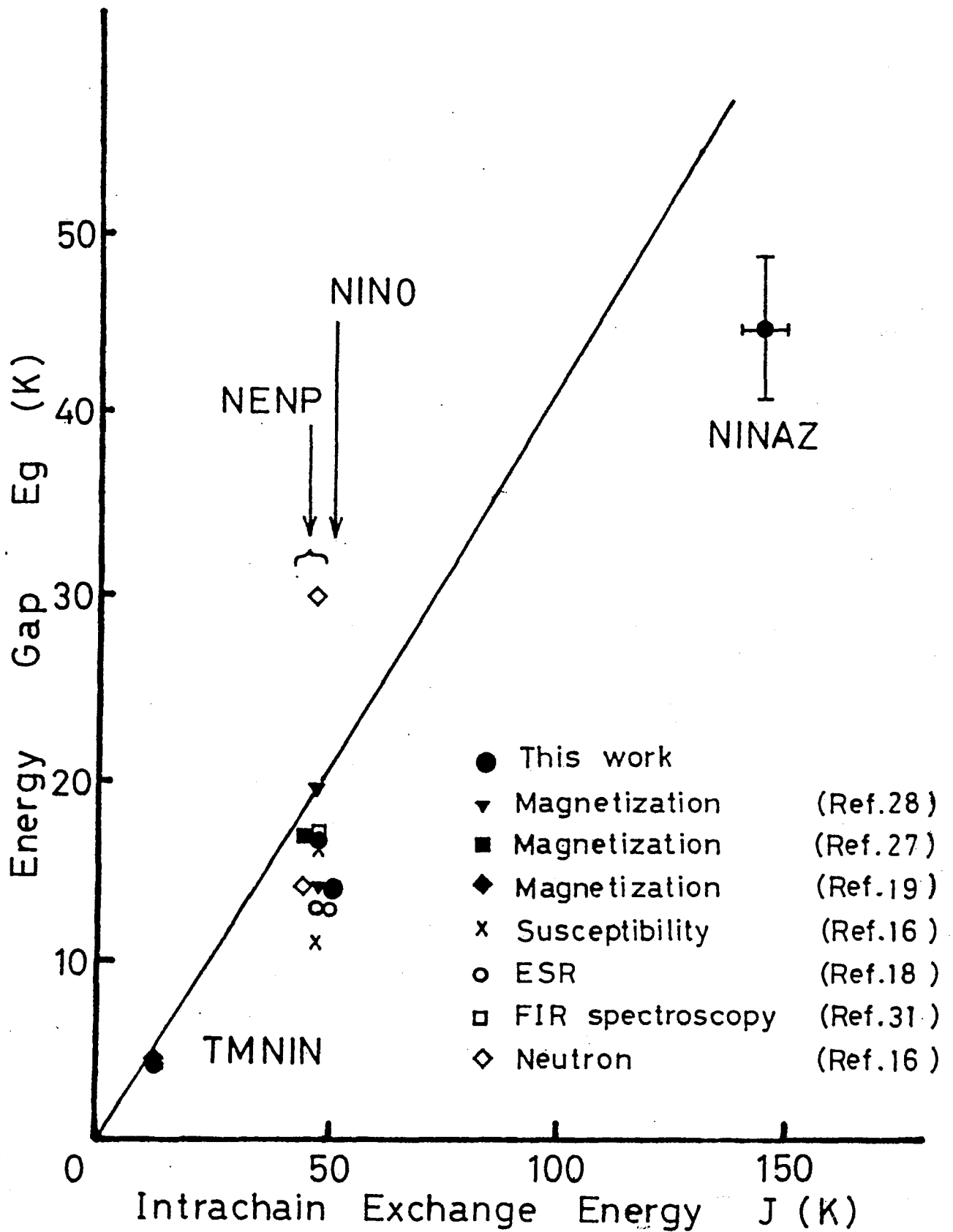


Fig.24. Relation between the Haldane gap energy and the intrachain exchange energy of several  $S=1$  quasi-one dimensional Heisenberg antiferromagnets obtained from various measurements. Two values of the energy gap of NENP(ref.16,28) was determined for respective field directions parallel and perpendicular to  $b$ -axis. Solid line is the theoretical value of  $E_g=0.41|J|$ .

NINO( $E_g=0.29|J|$ ), TMNIN( $E_g=0.34|J|$ ) and NINAZ( $E_g\approx 0.31|J|$ ) in this work are indicated in Fig.24. Those from other various measurements are also shown. Almost all of these data can be understood by the expression  $E_g=(0.35 \pm 0.05)|J|$  which is close to the theoretical value of  $E_g=0.41|J|$ .<sup>7)</sup> This confirms us that these materials are one-dimensional Heisenberg antiferromagnets and have the Haldane gap which is proportional to the intrachain exchange energy.

## 6. Conclusion

The magnetic susceptibility and magnetization measurements were performed on  $S=1$  one-dimensional Heisenberg antiferromagnets. The susceptibility of NENP and NINO clearly show the existence of the Haldane gap. The intrachain exchange energy  $J$  and  $g$ -values of NINO are obtained from susceptibility data. The high field magnetizations of single crystal samples NENP and NINO strongly support the existence of the Haldane gap and this gap are quenched by external magnetic fields at each transition field. The transition field corresponds to the crossover field from the ground state to a sublevel of the excited triplet. The anisotropy of the transition field is explained by introducing the crystalline field constants  $D$  and  $E$  for the excited triplet. The Haldane gap energy  $E_g$  and the crystalline field constants  $D$  and  $E$  of NENP and NINO are determined from magnetization measurements. The obtained parameters are in good agreement with those from recent ESR and far-infrared spectroscopy measurements. Even though the Haldane gap originate from many body effect, the anisotropy of the transition field of NENP and NINO is well explained by the simple energy level scheme discussed here.

TMNIN and NINAZ are specially designed to obtain a material which has different  $J$ -value from NENP and NINO. The susceptibility of TMNIN shows a round maximum at about 15 K and falls down rapidly as temperature decreases. The susceptibility in the high temperature region are well understood by the Curie-Weiss model for  $S=1$  one-dimensional Heisenberg antiferromagnet

with  $J=12$  K and  $g=2.25$ . The magnetization of TMNIN in the low field region is understood by the Haldane gap model as in NENP and NINO. High field magnetization shows the saturation behavior above 30 T and this magnetization process is well understood by the theoretical magnetization curve of  $S=1$  one-dimensional Heisenberg antiferromagnet. Whole profile of the magnetization curve are obtained for the first time in TMNIN.

The magnetic susceptibility of NINAZ exhibits a broad maximum at about 150 K indicating a strong antiferromagnetic coupling in the chain. The high temperature data of the susceptibility can be understood by a theoretical susceptibility curve with  $J=145$  K. The magnetization of NINAZ also shows the existence of the Haldane gap. The large Haldane gap is obtained reflecting the large intrachain exchange energy  $J$ .

The obtained results are compared with those of other various measurements and the relation between the Haldane gap energy and intrachain exchange energy is obtained to be  $E_g=(0.35\pm 0.05)|J|$  which is close to the theoretical value of  $E_g=0.41|J|$ .

## REFERENCES

- 1) F.D.M. Haldane : Phys. Rev. Lett. 50(1983)1153.
- 2) H. Bethe : Z. Phys. 71(1931)205.
- 3) J.C. Bonner and M.E. Fisher : Phys. Rev. A135(1964)640.
- 4) R. Botet and R. Jullien : Phys. Rev. B27(1983)613.
- 5) R. Botet, R. Jullien and M. Kolb : Phys. Rev. B28(1983)3914.
- 6) J.B. Parkinson and J.C. Bonner : Phys. Rev. B32(1985)4703.
- 7) M.P. Nightingale and H.W.J. Blöte : Phys. Rev. B33(1986)659.
- 8) I. Affleck, T. Kennedy, E.H. Lieb and H. Tasaki : Phys. Rev. Lett. 59(1987)799.
- 9) I. Affleck : Phys. Rev. B41(1990)6697.
- 10) M. Takahashi : Phys. Rev. Lett. 62(1989)2313.
- 11) H. Tasaki : Phys. Rev. Lett. 64(1990)2066.
- 12) T. Sakai and M. Takahashi : Phys. Rev. B43(1991)13383.
- 13) W.J.L. Buyers, R.M. Morra, R.L. Armstrong, M.J. Hogan, P. Gerlach and K. Hirakawa : Phys. Rev. Lett. 56(1986)371.
- 14) M. Steiner, K. Kakurai, J.K. Kjems, D. Petitgrand and R. Pynn: J. Appl. Phys. 61(1987)3953.
- 15) J.P. Renard, M. Verdaguer, L.P. Regnault, W.A.C. Erkelens, J. Rossat-Mignod and W.G. Stirling : Europhys. Lett. 3(1987)945.
- 16) J.P. Renard, M. Verdaguer, L.P. Regnault, W.A.C. Erkelens, J. Rossat-Mignod, J. Ribas, W.G. Stirling and C. Vettier : J. Appl. Phys. 63(1988)3538.
- 17) M. Steiner, K. Kakurai, J.K. Kjems, D. Petitgrand and R. Pynn: J. Appl. Phys. 61(1987)3953.
- 18) M. Date and K. Kindo : Phys. Rev. Lett. 65(1990)1659.

- 19) V. Gadet, M. Verdaguer, V. Briois, A. Gleizes, J.P. Renard, P. Beauvillain, C. Chappert, T. Goto, K. Le Dang and P. Veillet : Phys. Rev. B44(2)(1991)705.
- 20) T. Sakakibara, H. Mollmoto, M. Motokawa and M. Date : *High Field Magnetism*, M. Date ed. (North-Holland, Amsterdam, 1983), P.299.
- 21) T. Yosida, M. Morita and M. Date : J. Phys. Soc. Jpn. 57(1988)1428.
- 22) V. Gadet, M. Verdaguer, J.P. Renard, J. Ribas, C. Biaz, M. Montfort, X. Solans, C.P. Landee, J.P. Jamet, A. Dworkin : to be submitted to J. Am. Chem. Soc.
- 23) C.Y. Weng : Ph.D. Thesis, Carnegie Institute of Technology (1968)
- 24) A. Meyer, A. Gleizes, J. Girerd, M. Verdaguer and O. Kahn : Inorg. Chem. 21(1982)1729.
- 25) P. Gaveau, J.P. Boucher, L.P. Regnault and J.P. Renard: Europhys. Lett. 12(1990)1135.
- 26) J.P. Renard, L.P. Regnault and M. Verdaguer : J. de Phys. 49(1988)C8-1425.
- 27) K. Katsumata, H. Hori, T. Takeuchi, M. Date, A. Yamagishi and J.P. Renard : Phys. Rev. Lett. 63(1989)86.
- 28) Y. Ajiro, T. Goto, H. Kikuchi, T. Sakakibara and T. Inami : Phys. Rev. Lett. 63(1989)1424.
- 29) T. Takeuchi, M. Ono, H. Hori, T. Yosida, A. Yamagishi and M. Date : to be published in J. Phys. Soc. Jpn. 61(1992).
- 30) T. Haseda and M. Date : J. Phys. Soc. Jpn. 13(1958)175.

31) W. Lu, J. Tuchendler, M. von Ortenberg, J. P. Renard: Phys. Rev. Lett. 67(1991)3716.

32) T. Takeuchi, H. Hori, T. Yosida, A. Yamagishi, K. Katsumata, J.P. Renard, V. Gadet, M. Verdaguer and M. Date : to be published in J. Phys. Soc. Jpn. 61(1992).

## PART II

### EXTENSION OF THE HIGH FIELD MAGNETISM TO THE BIOLOGICAL SYSTEMS

#### ABSTRACT

An extension of the high field magnetism to the biological systems is shown with a special interest in the diamagnetic orientation of the biological macro-molecules under static magnetic field. Human blood materials, fibrinogen-fibrin fiber system, red blood cell, blood platelet are tested and unexpectedly large diamagnetic orientation is found. The order parameter of these materials are evaluated both by the light transmission and microscopic observations and they are analyzed by the extended theory of the diamagnetic orientation with diamagnetic anisotropy model.

## 1. Introduction

In 1855, Faraday found diamagnetism with wood, ivory, beef, mutton, etc..<sup>1)</sup> However, diamagnetic anisotropy of the biological systems was first reported after about one century by Lansdale and Arnold et al. on cellulose materials.<sup>2,3)</sup> Since then variety of biological materials have been investigated in magnetic fields. Typical example of the magnetic field effect on biological systems is seen in magnetotactic bacteria.<sup>4)</sup> The magnetotactic bacteria in sediments orient and swim along magnetic field direction toward the specified pole because it has a chain of single domain particles of magnetite.

It is well known that molecules having anisotropic diamagnetic susceptibility such as benzene and nitrobenzene are oriented in an applied magnetic field. The orientation is usually detected by the magnetic birefringence, i.e., the Cotton-Mouton effect.<sup>5,6)</sup> Extensive studies of magnetic orientation in pulsed magnetic field up to 30 T (Tesla) have been done by Yamagishi et al.<sup>7,8)</sup> and the diamagnetic Curie-Weiss law has been found in many organic liquids. However, the order parameter induced by the magnetic field is of the order of  $10^{-6}$  due to the fact that the field induced energy is far below the thermal energy at room temperature.

In some macro-molecules, however, considerable degrees of the orientation are expected if the molecules consist of many aligned radicals having diamagnetic anisotropy. Typical examples are seen in the biological macro-molecules and the diamagnetic orientation under static magnetic field has been inves-

tigated for various materials. The magnetic orientation of retinal rod outer segments,<sup>9,10)</sup> chloroplasts,<sup>11)</sup> photosynthetic algae and bacteria,<sup>12,13)</sup> purple membranes<sup>14)</sup> and nucleic acids<sup>15)</sup> have been attributed to the diamagnetic anisotropy of the macro-molecular origin.

Lipid tubules, which are straight hollow cylinders consisting of lipid bilayers, has been investigated in a magnetic field.<sup>16)</sup> The tubules were found to orient with their long axes parallel to the field direction. This result shows that the lipid molecules are oriented with their long hydrocarbon chains normal to the applied magnetic fields.

The first half part of this paper shows the theoretical treatment of the diamagnetic orientation of macro-molecules. It is shown that a full orientation is easily achieved when the diamagnetic biological molecules aggregate in the magnetic field, if they aggregate keeping their diamagnetic principal axes along the field direction. A typical result is given by the polymerization of fibrinogen under a magnetic field.

The last half part of this paper shows that red blood cells (RBC) and blood platelets are oriented by static magnetic fields. The molecular origin of diamagnetic anisotropy of RBC and blood platelets are also discussed.

## 2. Theory

Let us now consider a rod-like macro-molecule in a magnetic field with anisotropic diamagnetic susceptibilities  $\chi_{\parallel}$  and  $\chi_{\perp}$  along the directions parallel and perpendicular to the rod axis, respectively, as shown in Fig. 1. The field-induced energy  $U$  is given by<sup>7)</sup>

$$U = -(H^2/2)(\chi_{\perp} + \Delta\chi\cos^2\theta), \quad (1)$$

and the order parameter  $\langle m \rangle$  is defined with usual manner as<sup>8)</sup>

$$\begin{aligned} \langle m \rangle &= \langle 3\cos^2\theta - 1 \rangle / 2 \\ &= \frac{1}{2} \frac{\int_0^{\pi} (3\cos^2\theta - 1) \exp(-U/kT) \sin\theta \, d\theta}{\int_0^{\pi} \exp(-U/kT) \sin\theta \, d\theta}, \end{aligned} \quad (2)$$

where  $\theta$  is the angle between a magnetic field  $H$  and the rod axis,  $\Delta\chi = \chi_{\parallel} - \chi_{\perp}$  and  $kT$  is the thermal energy. Equation (2) is simply expressed as

$$\langle m \rangle = \frac{3}{4\alpha} \left( \frac{e^{\alpha}}{I} - 1 \right) - \frac{1}{2}, \quad (3)$$

where  $I$  and  $\alpha$  are given by

$$I = \int_0^1 \exp(\alpha t^2) dt, \quad (4)$$

$$\alpha = \Delta\chi H^2 / 2kT. \quad (5)$$

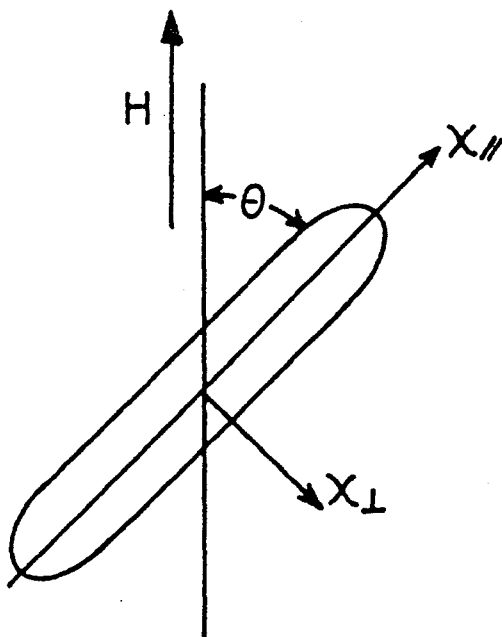


Fig. 1. A rod-like macro-molecule in a magnetic field.  $\chi_{\parallel}$  and  $\chi_{\perp}$  are the magnetic susceptibilities parallel and perpendicular to the molecular axis.  $\theta$  is the angle between the field and the molecular axis.

For the cases  $\alpha \ll 1$  (low field and/or high temperature limit) and  $\alpha \gg 1$  (high field and/or low temperature limit), eq.(3) is expanded as follows:

$$\alpha \ll 1, \quad \langle m \rangle = \frac{2\alpha}{15} \left( 1 + \frac{2}{21} \alpha \right), \quad (6)$$

$$\alpha \gg 1, \quad \langle m \rangle = 1 - \frac{3}{2\alpha} \left( 1 + \frac{1}{2\alpha} \right). \quad (7)$$

The first term of eq.(6) was obtained by Langevin<sup>6)</sup> (dotted line in Fig. 2) and it shows a quadratic dependence on H as generally seen in the Cotton-Mouton coefficients for organic liquids. The crossing point of the dotted line ( $\langle m \rangle = 2\alpha/15$ ) with the line of  $\langle m \rangle = 1$  gives  $\alpha = 15/2$ . Equation (3) shows the saturation behavior and gives  $\langle m \rangle = 0.8$  for  $\alpha = 15/2$  obtained above. That is, the condition  $\Delta\chi H^2/15kT = 1$  gives 80% magnetic orientation of the molecules. This condition is used to estimate the field intensity required for nearly full orientation. The whole curve corresponding to equation (3) has been calculated and is shown in Fig. 2 by a solid line.

A new unit to express the magnitude of diamagnetic anisotropy is defined, because usual emu value for molecules is too small and inconvenient. The new unit is defined by expressing  $\Delta\chi$  reduced to that of a typical diamagnetic anisotropy in benzene molecule.  $\Delta\chi$  of benzene is  $9.91 \times 10^{-29}$  emu<sup>17)</sup> and it is defined as one  $D_B$  (diamagnetic benzene). Therefore,  $\Delta\chi$  in the unit of  $D_B$  means the value of benzene equivalent and it is easy to evalu-

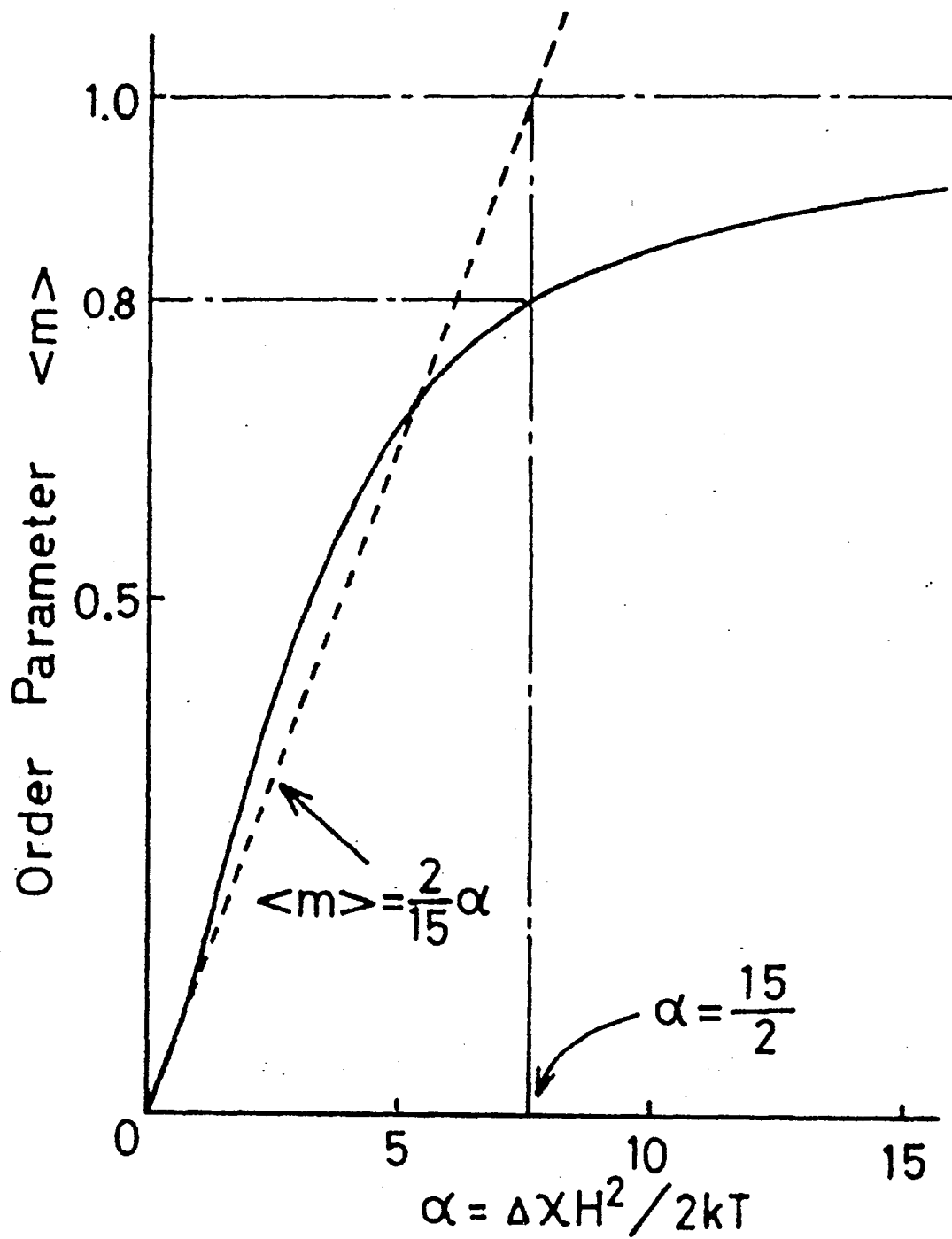


Fig. 2. Order parameter  $\langle m \rangle$  as a function of  $\alpha = \Delta\chi H^2 / 2kT$ . The full and the dashed lines are given by eq. (3) and the first term of eq. (6), respectively. 80% orientation is obtained at  $\alpha = 15/2$ , which is obtained as the crossing point of  $\langle m \rangle = 2\alpha/15$  and  $\langle m \rangle = 1$ .

ate with reference to benzene.

Figure 3 shows field dependencies of the order parameter for various values of  $\Delta\chi$ . For example,  $\Delta\chi=10^{-21}$  emu is about  $10^7 D_B$  which is equivalent to  $10^7$  benzene molecules aligned in the same direction at the field of 6 T.

When N molecules aggregate with their diamagnetic principal axes along the same direction,  $\Delta\chi$  in eqs. (1)-(7) should be replaced by  $N\Delta\chi$ . When N becomes large enough, a large magnetic anisotropy energy is expected and  $\alpha \gg 1$  is easily satisfied even at low magnetic field. In such case, the corresponding order parameter  $\langle m \rangle$  reaches the saturated value even at 1 T.

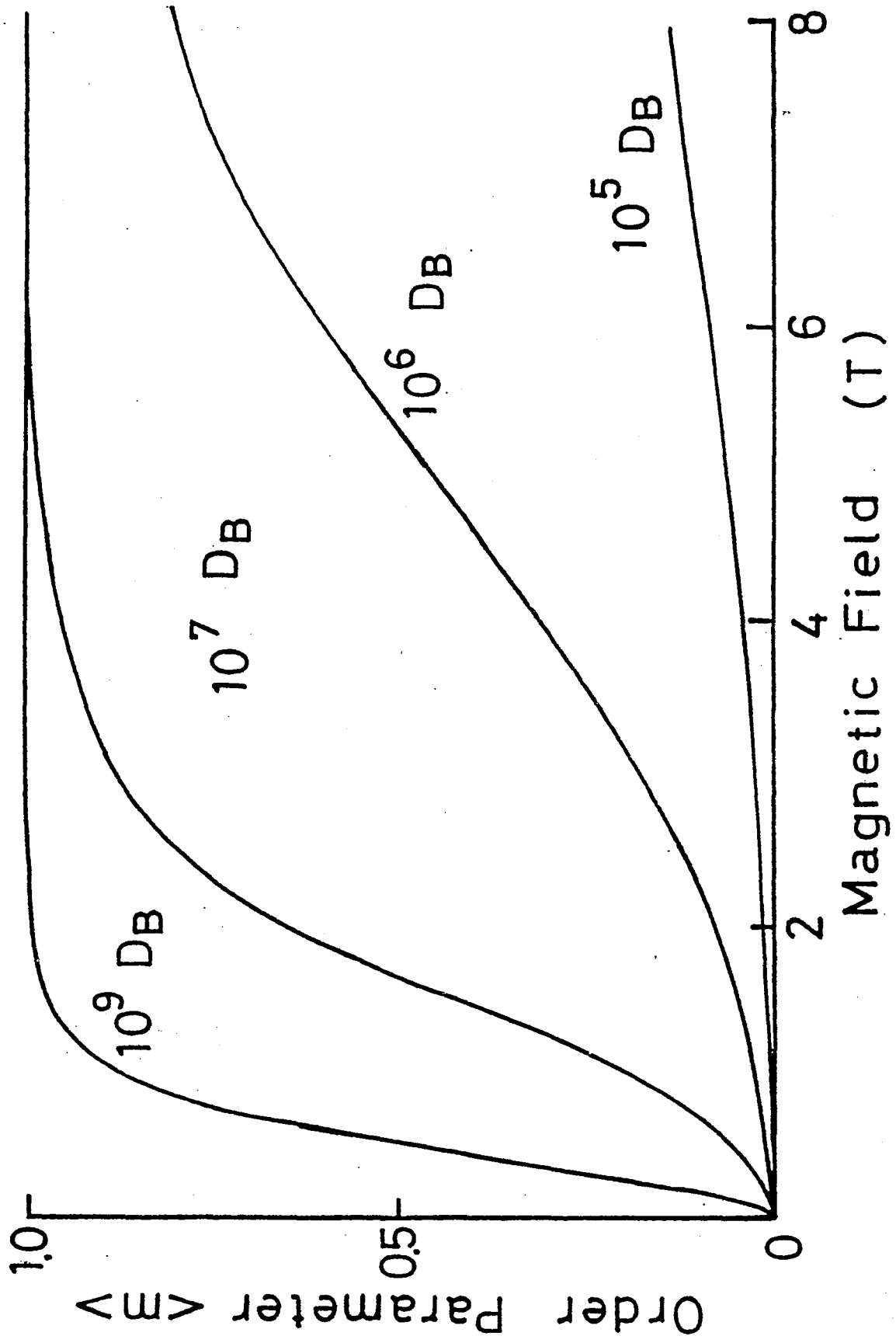


Fig. 3. Theoretically calculated order parameter  $\langle m \rangle$  as a function of magnetic field for various values of  $\Delta\chi$ .

### 3. Experimental procedures

Experiments of magnetic orientation in biological systems were carried out at the Low Temperature Center, Osaka University. Figure 4 shows the experimental set-up. A static magnetic field up to 8 T are produced by a superconducting magnet, which has room temperature experimental space of 6 cm in diameter and 20 cm in length. The inhomogeneity of the field strength is less than 1% in the experimental space. An iron-core electromagnet is also used to demonstrate the magnetic orientation of fibrin in a field as low as 1 T. Two quartz sample cells of  $1 \times 1 \times 4.5 \text{ cm}^3$  are put in copper tubes and their temperatures are controlled at about 24 °C by flowing water from a thermal bath. One cell is in the magnet and the other is out of it for comparison. He-Ne laser light is used to monitor the optical transmissivity.

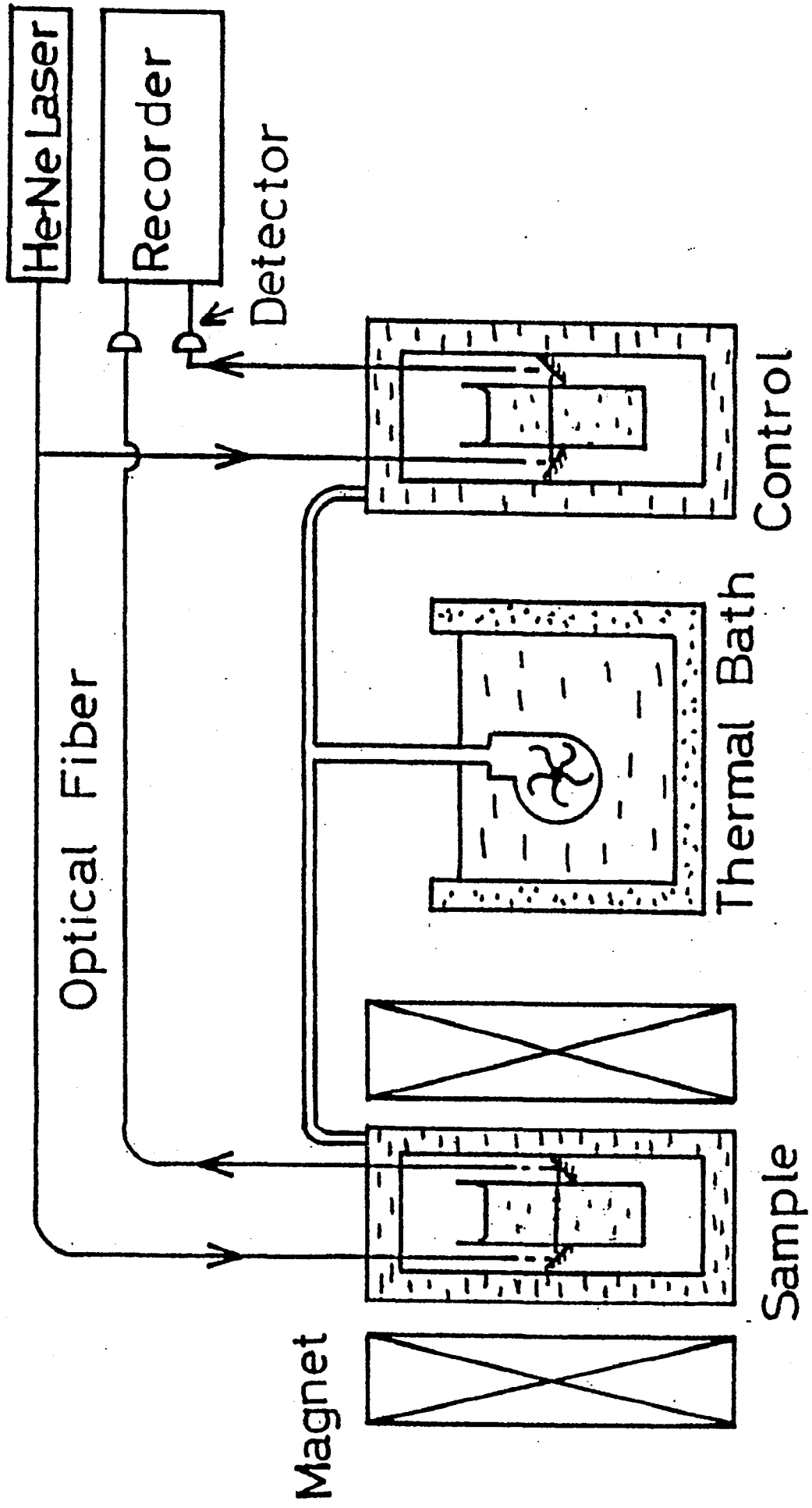


Fig. 4. Experimental set-up for the investigation of magnetic orientation of biological systems in a static magnetic field.

#### 4. Polymerization of fibrinogen in high magnetic fields<sup>18-20)</sup>

##### 4-1 Structure of fibrin fiber and sample preparation

A human blood material, fibrinogen, one of the plasma proteins has a molecular weight of 340,000 and bent rod form of about 90 Å and 450 Å in diameter and length, respectively as shown in Fig. 5. Fibrinogen is known to polymerize into fibrin fiber<sup>21)</sup> and the magnetic field effect on the polymerization has been reported.<sup>22)</sup> Fibrinogen contains  $N_{\text{peptide}}=666$  planar peptide bonds in the  $\alpha$ -helices keeping their diamagnetic axes along the helical axis and the helix makes a coiled-coil, as shown in Fig. 6.<sup>23)</sup>

A planar peptide has diamagnetic anisotropy  $\Delta\chi_{\text{peptide}}=9 \times 10^{-2}D_B$ .<sup>24)</sup> The diamagnetic anisotropy of  $\alpha$ -helix have been calculated by Worcester<sup>25)</sup> and it is expressed as  $\Delta\chi_{\alpha\text{-helix}}=N\Delta\chi_{\text{peptide}}/2$ , where  $N$  is the peptide number contained in a  $\alpha$ -helix. The diamagnetic anisotropy of a half of fibrinogen  $\Delta\chi_{\text{half}}$  can be calculated from above equation by taking a diamagnetic principal axes parallel to the molecular axes.<sup>25)</sup>

$$\Delta\chi_{\text{half}}=(N_{\text{peptide}}/2)\times(\Delta\chi_{\text{peptide}}/2)\times 0.98=(15\pm 1)D_B, \quad (8)$$

here 0.98 is the constant coming from  $\alpha$ -helix makes coiled-coil structure. As fibrinogen has bent rod structure, total diamagnetic anisotropy of fibrinogen is expressed as

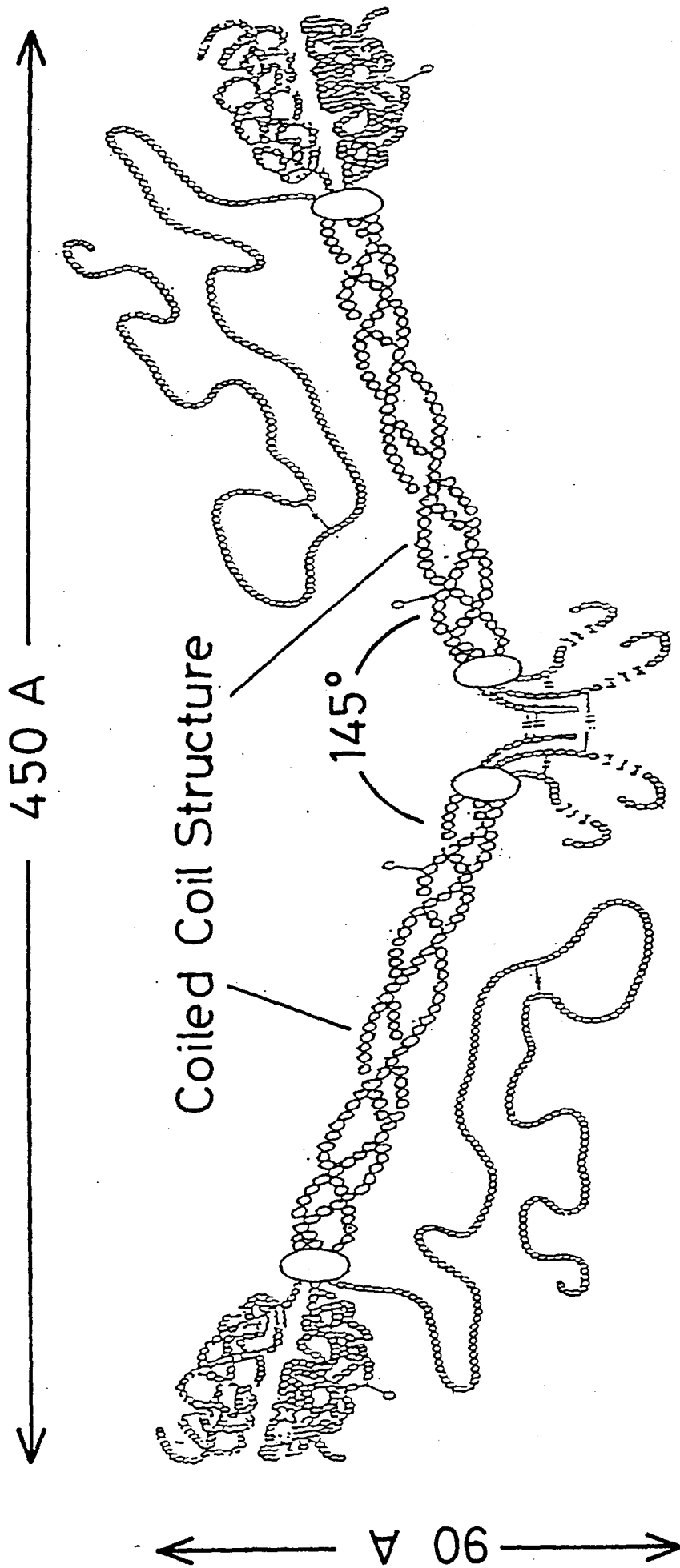
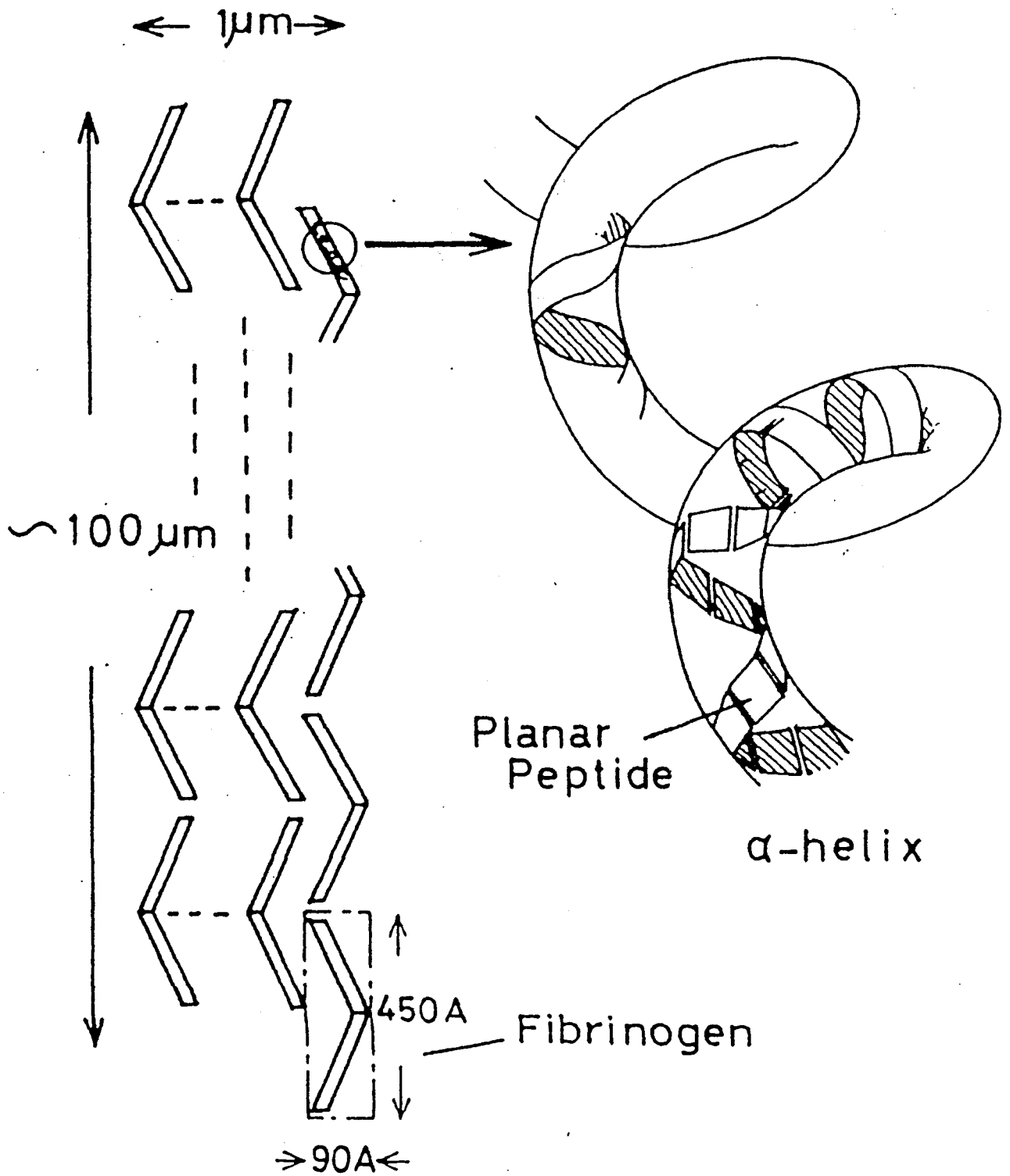


Fig. 5. Schematic views of fibrinogen. Anisotropic diamagnetic susceptibility of the molecule originates from coiled-coil structure of  $\alpha$ -helices.



## Fibrin Fiber

Fig. 6. Schematic views of fibrin fiber. The detailed structure is shown successively. The anisotropic diamagnetic susceptibility originates from peptide bonds contained in  $\alpha$ -helix.

$$\Delta\chi_{\text{fibrinogen}} = 2 \times (3 \cos^2((180-145)/2) - 1) \times \Delta\chi_{\text{half}} / 2 \quad (9)$$

$$= (26 \pm 2) D_B.$$

The average size of polymerized fibrin fibers is about 1  $\mu\text{m}$  in diameter, 100  $\mu\text{m}$  in length and the rod contains about  $10^7$  monomers of the fibrinogen. The value of  $N\Delta\chi$  of a fibrin fiber is about  $2.6 \times 10^8 D_B$  so that it is expected that the some degree of magnetic orientation can be obtained even in a field as low as 1 T from Fig. 3.

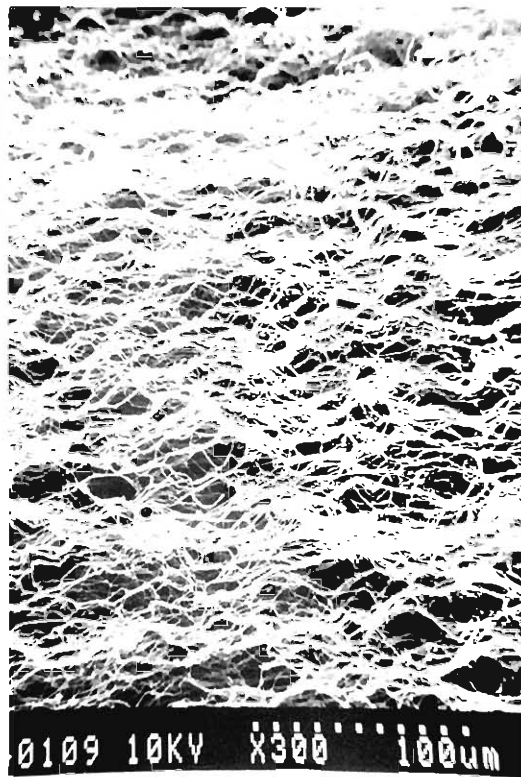
The solution of bovine plasminogen free fibrinogen (500 mg/dl) in the buffer (Tris-HCl 0.5 M, pH7.5, NaCl 0.03 M) and the solution of human thrombin (0.25 units/ml) in the same buffer are mixed at the ratio of 13:1 just before the experiment.

#### 4-2 Experimental results and discussion

Fibrin gels polymerized in magnetic fields are fixed and dehydrated by using glutaraldehyde solution and ethanol and then dried for observation by means of a scanning electron microscope (SEM). Examples of SEM images of the fibrin fibers which were polymerized (a) in a magnetic field of  $H=8$  T and (b) without a magnetic field  $H=0$  are shown in Fig. 7. A clear magnetic field effect is seen in these photographs. Figure 8 shows the light transmissivity and the degree of polarization as a function of time. The optical transmissivity decreases as polymerization proceeds because the light scattering cross-section increases as the molecular size increases. The scattering cross-section also depends on the polarization of light, parallel or perpendicular to the molecular axis.<sup>25)</sup> Therefore, the degree of orientation is estimated by monitoring the degree of polarization of the transmitted light which can be normalized with the data of full orientation. The degree of polarization is defined as

$$P=(T_{\perp} - T_{\parallel})/(T_{\perp} + T_{\parallel}), \quad (10)$$

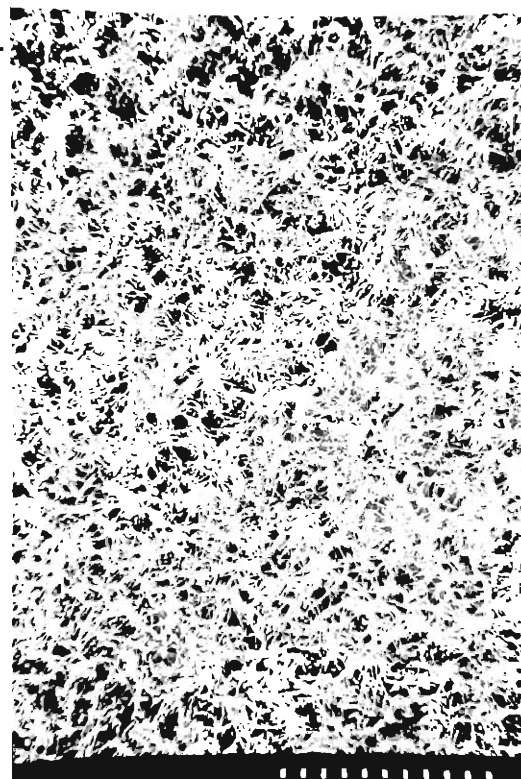
where  $T_{\parallel}$  and  $T_{\perp}$  are the transmissivities for the light polarized parallel and perpendicular to the field direction, respectively. Defining an average light scattering cross-section  $\sigma_0$  for randomly oriented fibers and scattering cross-sections  $\sigma_{\parallel}$  and  $\sigma_{\perp}$  for the light polarized parallel and perpendicular to the molecular axis, respectively, we can express the transmissivities  $T_{\parallel}$  and  $T_{\perp}$  as



(a)



$H = 8 \text{ T}$



(b)

$H = 0$



100  $\mu\text{m}$

Fig. 7. Scanning electron microscope images of fibrin gels, (a) polymerized in 8 T field and (b) control (zero field). The field direction is shown by an arrow.

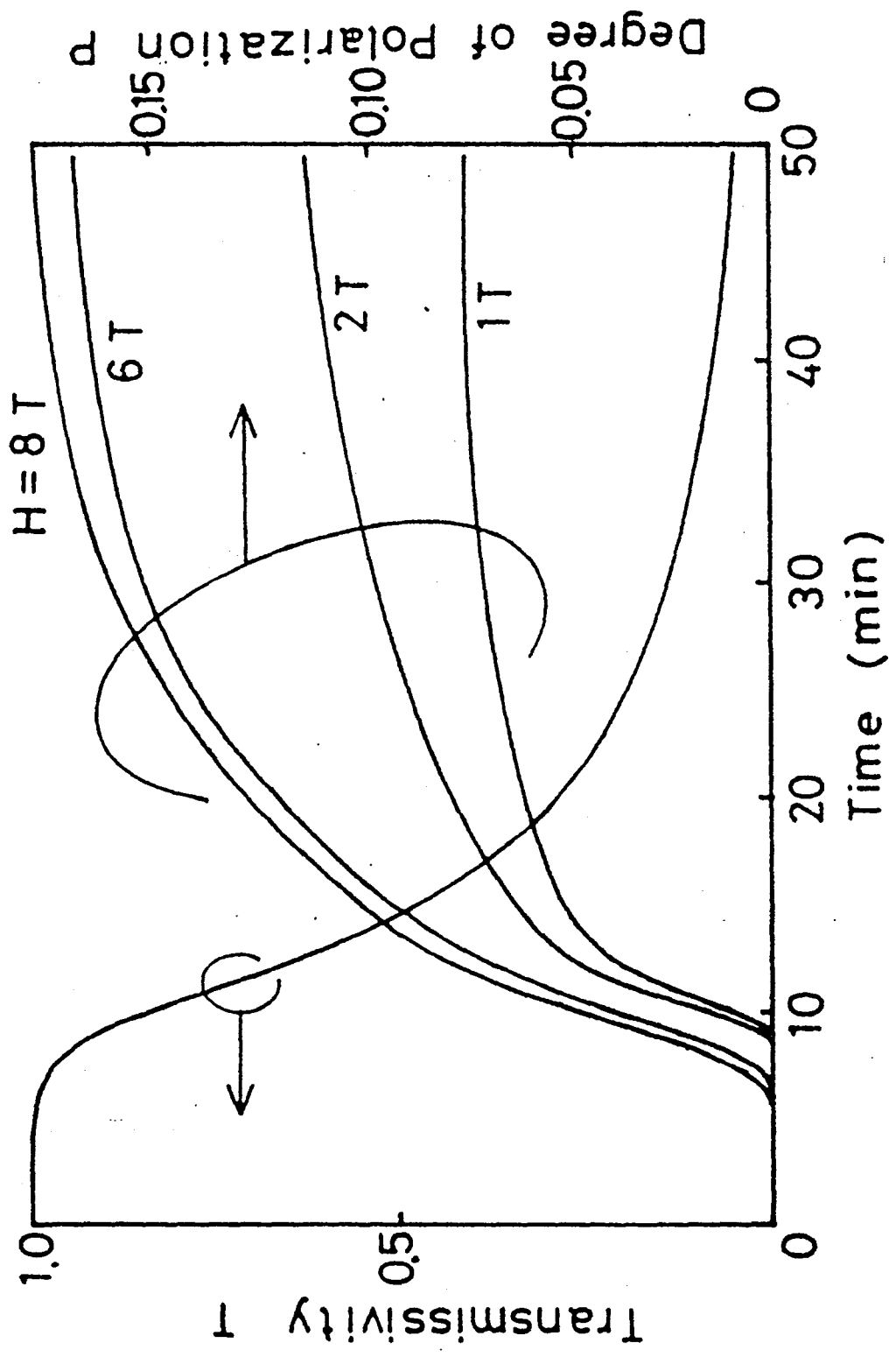


Fig. 8. Light transmissivity (T) and degree of polarization (P) of transmitted light as functions of polymerization time.

$$T_{\parallel} = \exp\{-(d/N_0)(\sigma_{\parallel}n_o + \sigma_o n_r)\}, \quad (11)$$

$$T_{\perp} = \exp\{-(d/N_0)(\sigma_{\perp}n_o + \sigma_o n_r)\}, \quad (12)$$

where  $d$  is an optical path length of the sample. The numbers of fibers per unit volume,  $N_0$ ,  $n_r$  and  $n_o$  are defined as the total number of fibers  $N_0 = n_r + n_o$ , the number of fibers randomly oriented in all directions and the number of fibers magnetically oriented in the field direction, respectively. When no magnetic field is applied, the fibers are distributed in all directions, so that  $n_r = N_0$ ,  $n_o = 0$  and  $T_{\parallel} = T_{\perp}$ .  $n_o/N_0$  denotes the degree of orientation of the fibers. Equations (10)-(12) give the relation between  $P$  and  $n_o/N_0$  as

$$\exp\left(\frac{d\Delta\sigma n_o}{N_0}\right) = \frac{1 + P}{1 - P}, \quad (13)$$

where  $\Delta\sigma = \sigma_{\parallel} - \sigma_{\perp}$ . As almost 100% orientation is attained at the field of 8 T (Fig. 7),  $n_o/N_0$  is evaluated to be 1. From Fig. 8,  $P = 0.17$  is obtained at the field of 8 T. These values give  $d\Delta\sigma = 0.34$ . Equations (11) and (12) may not be correct in the region of high density of fiber. However, equation (13) can be used to estimate the degree of orientation of the fibers in various magnetic field strength. One of results is shown in Fig. 9. The curve could be changed depending on the condition of chemical reactions, that is, density of solution, thrombin concentration, temperature, pH and so on. The important point is that considerable orientation ( $n_o/N_0 = 0.44$  in Fig. 9) of the

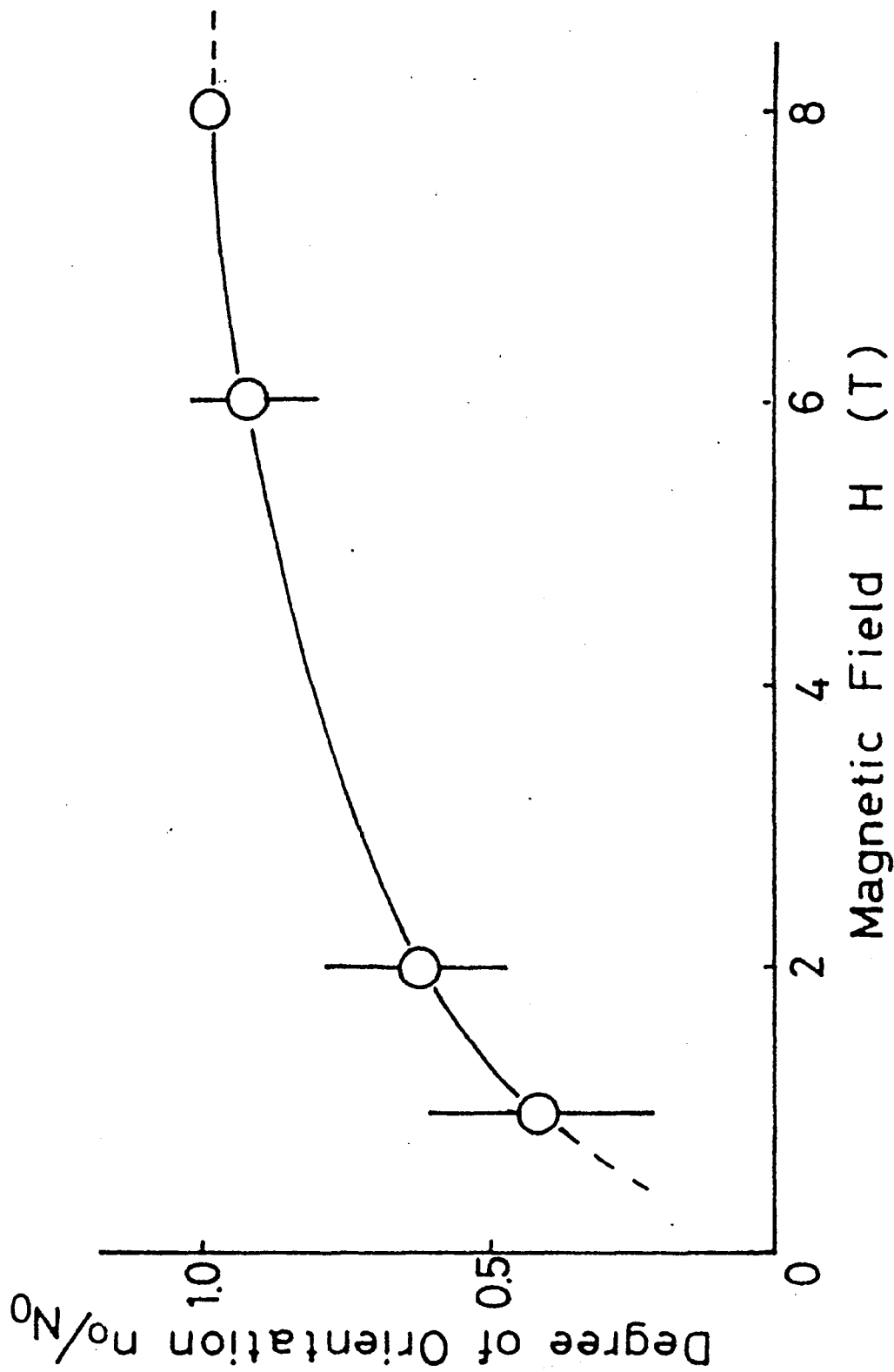


Fig. 9. Degree of orientation of fibers  $n_0/N_0$  as a function of magnetic field  $H$ . The method of estimation is shown in the text. Considerable orientation is obtained even in a field as low as 1 T.

fibers is obtained even in 1 T.

Figure 10 shows the time development of  $N$ , the number of fibrinogens in a fiber, during the course of polymerization. The number of  $N$  is calculated as follows. Using the average light scattering cross-section  $\sigma_0$  which depends on the molecular size, the transmissivity  $T$  of a dilute solution of the fibers is given by

$$T = \exp(-n\sigma_0), \quad (14)$$

where  $n$  is the number of fibers per unit volume and is assumed constant through the clotting process.  $n=10^6 \text{ mm}^{-3}$  is obtained by dividing the initial fibrinogen concentration by the number of fibrinogen molecules in a fiber at the final stage. For a rod-like molecule,  $\sigma_0$  is given by<sup>26)</sup>

$$\sigma_0 = 19.2 \left[ \frac{\pi a(m-1)}{\lambda} \right]^2 al, \quad (15)$$

where  $a$  and  $l$  are radius and length of the rod, respectively.  $\lambda$  is the wave length of the light and  $m$  the ratio of refractive indices of the fiber and the buffer solution. Using equations (14) and (15) and assuming that  $m=1.05$  and that the fiber grows with a similar form ( $l=200a$ ), the size  $a$  can be obtained as a function of time. The number of fibrinogens in a rod is expressed as

$$N = \pi a^2 \times 200a / v, \quad (16)$$

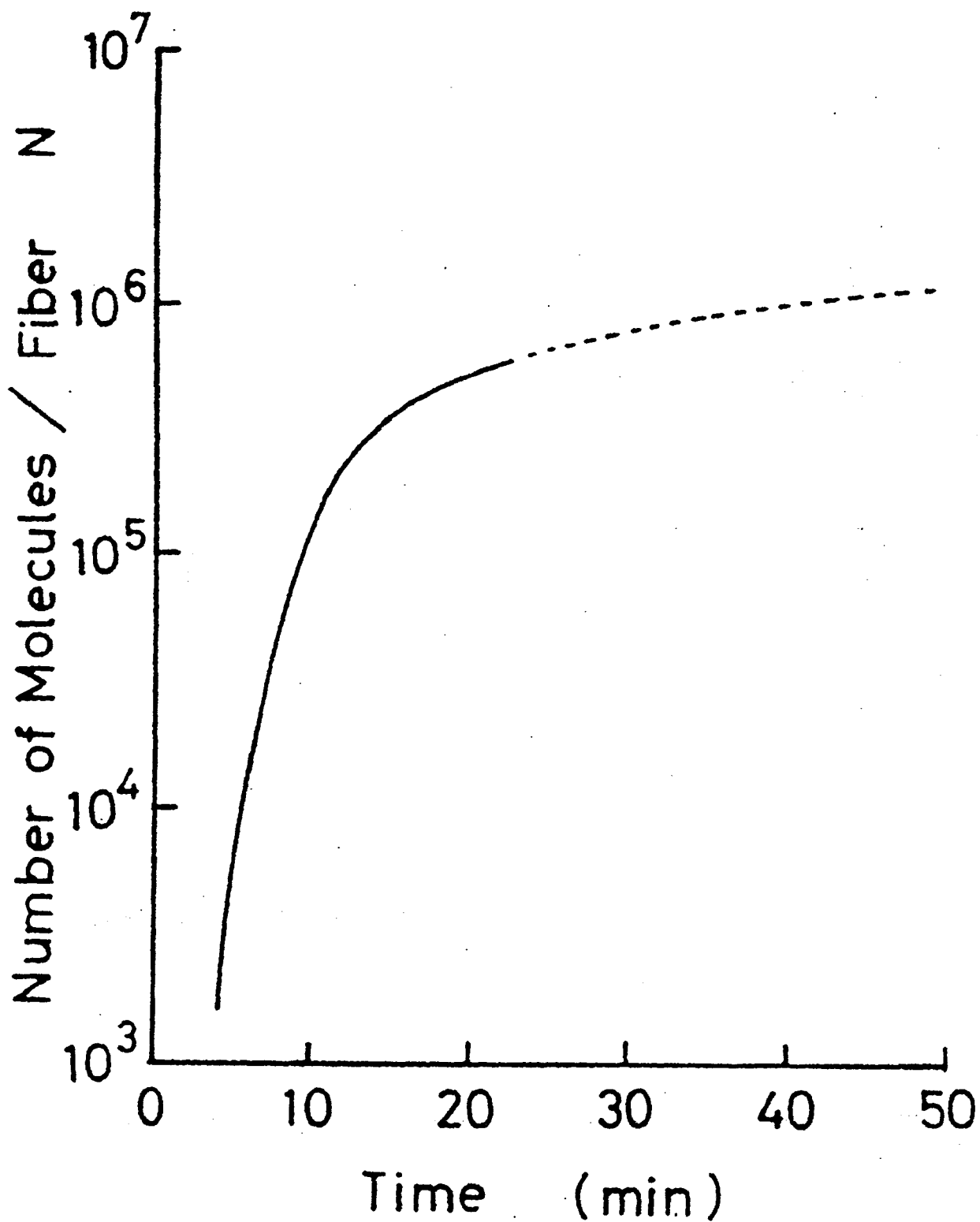


Fig.10. The fibrinogen number  $N$  aggregated in a fibrin fiber as a function of time. In the first 10 min, the fiber grows rapidly and  $N$  becomes  $10^5$  which is large enough for the magnetic energy to overcome the thermal energy.

where  $v=3 \times 10^{-6} \mu\text{m}^3$  is the volume of a fibrinogen.

The calculation may not be accurate for the high concentration region of fibers and N-value in this region is shown by a dotted curve in Fig.10. The number N shows a rapid increase in the first 15 minutes up to about  $5 \times 10^5$  and in the final stage the fiber has about  $10^6-10^7$  fibrinogens. This implies that the fundamental structure of orientation of the fiber is formed in the first 20 minutes and that the magnetic field is probably less effective in the later period of the reaction process because the liquid becomes too viscous to rotate.

Even if the field is turned off during the course of clotting, oriented fibers are obtained when large enough fibers have been grown. The degree of orientation depends on the field-off time (the time when fields are turned off). It takes a few minutes to turn off fields (about 15 minutes from 8 T to zero), so that the samples are taken out of the magnet at the field-off time. A typical example is shown in Fig.11 for an applied magnetic field of 4 T. One sample is pulled out of the magnet at time A. The polarization curve traces  $c \rightarrow d \rightarrow a$  and finally degree of polarization becomes zero. The other sample is taken out of the magnet at the time B and the polarization curve becomes  $c \rightarrow d \rightarrow e \rightarrow b$ . The final product shows almost the same degree of orientation as gels fully grown up in the field. A sample pulled out a few minutes later than A shows partial orientation. These results imply that the important time duration to obtain oriented gels is 15-20 minutes under the conditions of Fig.11. During this period, the size of fibers are large enough for the magnetic energy to overcome the thermal energy so that

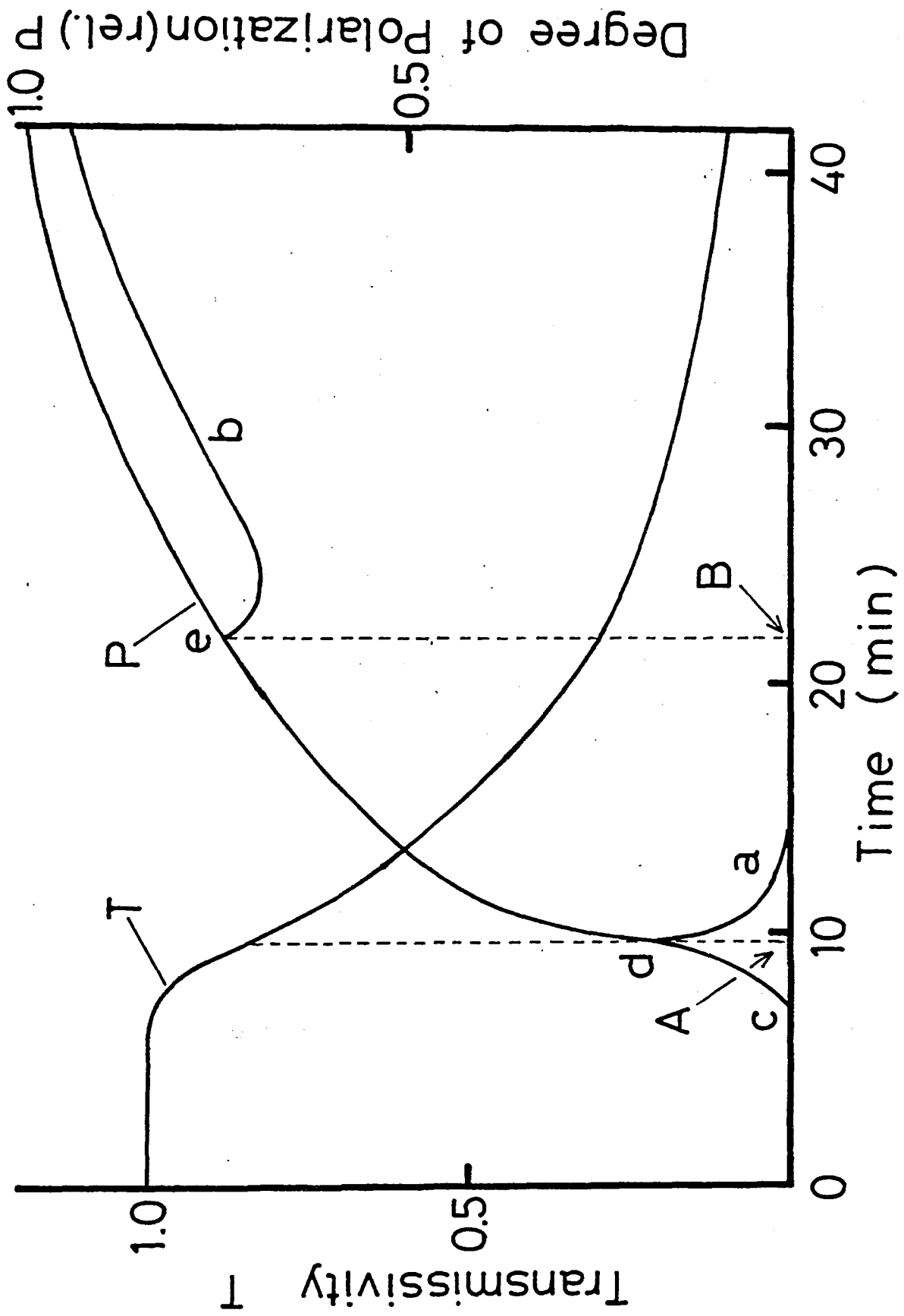
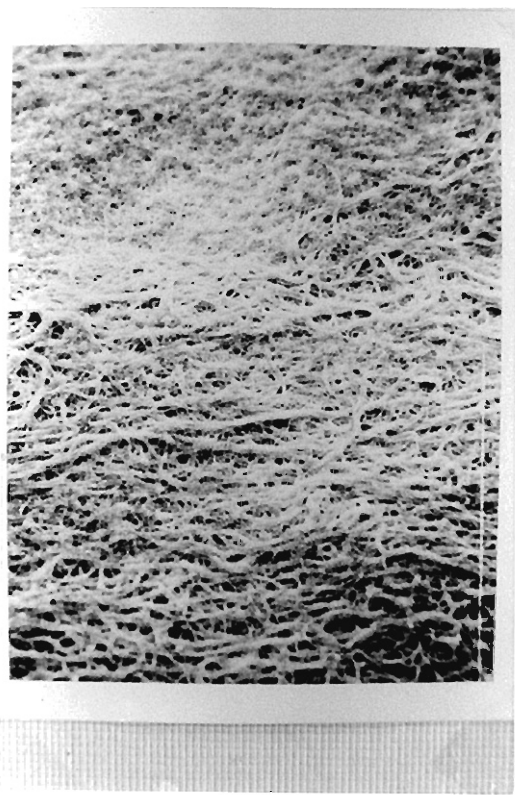


Fig.11. Light transmissivity (T) and the degree of polarization (P) as a function of polymerization time. One sample is taken out of the magnetic field at time A and the other at B. In the former case, the degree of polarization traces c→d→a and finally goes to zero.

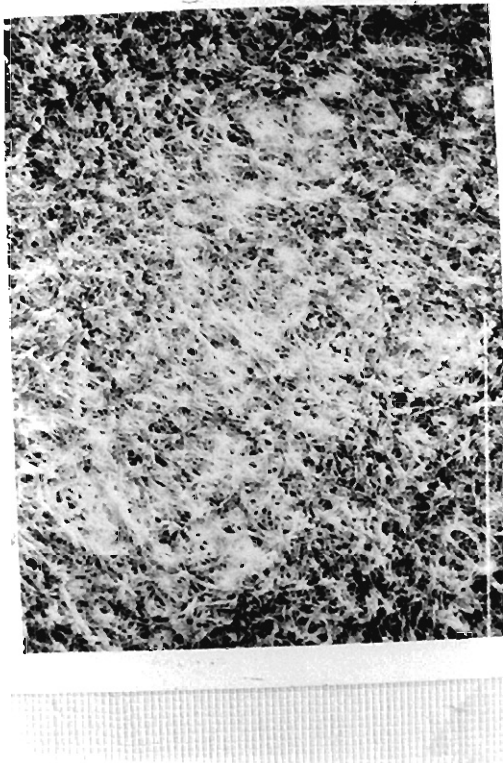
they can rotate magnetically, and not too large to be disturbed in their rotation by neighboring large fibers.

To demonstrate magnetic orientation of a fibrin fiber in 1 T, polymerization was carried out in a magnetic field produced by an iron-core electromagnet with pole-piece spacing of 100mm. SEM photographs of clotted gels are shown in Fig.12(a) and (b), corresponding to samples in a magnetic field of 1 T and in zero field, respectively. Considerable orientation is seen even in 1 T (Fig.12(a)) as expected from the polarization measurements. However, after precise examination of the photograph, it seems that some areas exist with considerably oriented fibers and some with randomly oriented fibers.



(a)

→  
 $H = 1 \text{ T}$



(b)

$H = 0$

←→  
100  $\mu\text{m}$

Fig.12. SEM images of clotted fibrin fibers. (a) A sample clotted in a field of 1 T and (b) a control without magnetic field ( $H=0$ ). Considerable orientation is seen in (a).

## 5. Blood cells in high magnetic fields

### 5-1 Materials and experiments

There are many materials in human blood with various forms and structures. In this section, two materials, red blood cell (RBC) and blood platelet are investigated under high magnetic field, because the sizes and shapes are well defined in blood and quantitative analysis is available in these materials.

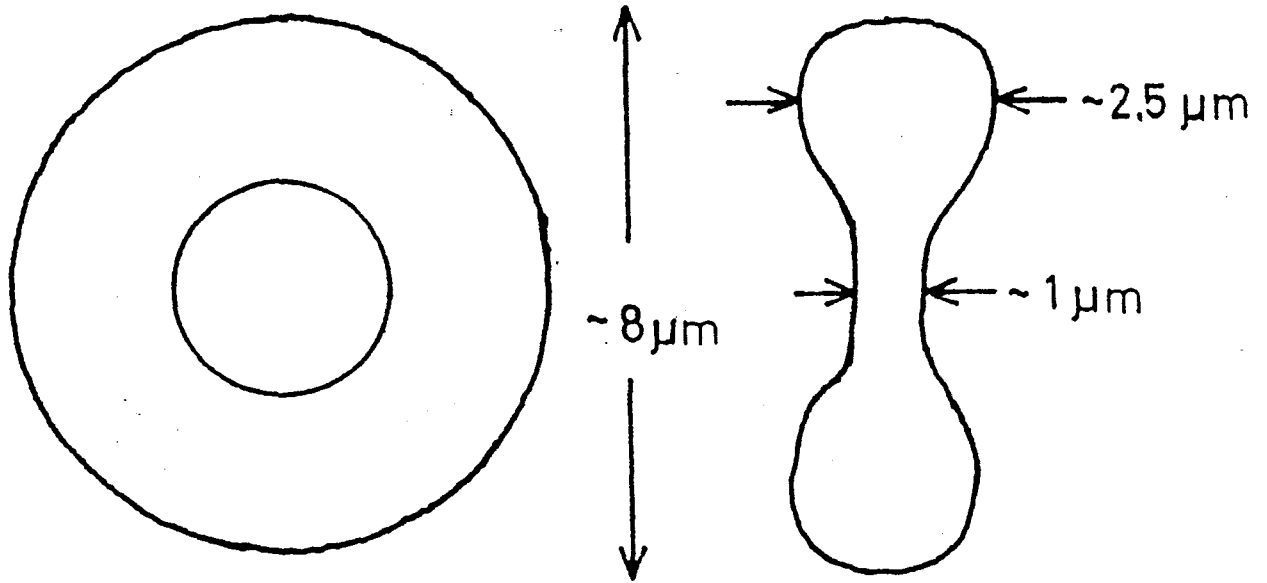
Figure 13 shows schematic drawings of the shapes of RBC and blood platelet with their sizes. RBC have a biconcave discoid shape with a diameter of about 8  $\mu\text{m}$  and thickness of about 2.5  $\mu\text{m}$ . Blood platelets are normally biconvex disk shaped with a diameter of about 2.5  $\mu\text{m}$  and thickness of about 0.6  $\mu\text{m}$ . RBC are covered with cell membrane consisted of aligned lipid molecules and contain hemoglobins which amounts to 95% of the total proteins and hemoglobins have diamagnetic and paramagnetic nature depending on their spin states.

It is well known that hemoglobin has Fe ions and the oxidation-deoxidation-reaction is one of the most important biochemical reactions in the human body. There are several valence states of the Fe ion and they are listed in Table 1. Except OXY-hemoglobin with the low spin state of  $\text{Fe}^{2+}$ , the materials are paramagnetic as are seen in Table. 1.

The solidified red blood cells, in which hemoglobin molecules are solidified, are also investigated to see the effect of hemoglobin motion.

Blood platelets are covered with cell membrane consisted of

Red Blood Cell



Blood Platelet

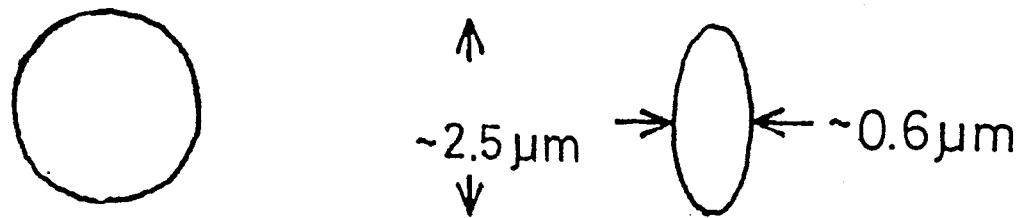


Fig.13. Schematic drawings of red blood cell and blood platelet.

Normal red blood cell			
$Fe^{2+}$		$Fe^{3+}$	
High Spin	Low Spin	High Spin	Low Spin
S=2	S=0	S=5/2	S=1/2
DEOXY-	OXY-	METH-	METL-

Solidified red blood cell	
$Fe^{3+}$	
High Spin	Low Spin
S=5/2	S=1/2
SMETH-	SMETL-

Table I. Various kinds of RBC investigated in this experiment.

the ordered lipid molecules. However, there are no paramagnetic molecules inside. The solidified blood platelets, in which proteins are solidified, are also investigated.

Whole venous blood from healthy volunteers was diluted into 1/10 in concentration with 3.8% sodium citrate. It was centrifuged at 1500g for five minutes to remove plasma and buffy coat. After washing with an isotonic buffered saline solution (90 mM NaCl, 5 mM KCl, 5.6 mM glucose, 50 mM Na-phosphate, pH7.5), RBC were suspended in the buffer and used as OXY-RBC, while DEOXY-RBC were prepared with 25 mM  $\text{Na}_2\text{S}_2\text{O}_4$  into suspension of OXY-RBC and nitrogen gas was flushed around the sample cell during experiment. METH-RBC were prepared by oxidizing OXY-RBC with  $\text{NaNO}_2$  (20 mM). Then, they were washed five times and suspended in an isotonic buffered saline of pH5.7. METL-RBC were obtained by treating the METH-RBC with KCN, then washed three times with the isotonic buffer at pH7.4.

SMETH- and SMETL-RBC were prepared by treating OXY-RBC with glutaraldehyde (coagulant of protein) and then with  $\text{NaNO}_2$  for SMETH-RBC and KCN for SMETL-RBC.

The suspension of blood platelets was prepared by the following way. Freshly drawn venous blood was centrifuged for fifteen minutes. The platelet rich plasma was obtained and then they were washed and suspended in isotonic saline solution. Solidified blood platelets were prepared by treating normal blood platelet with glutaraldehyde.

For morphological observation, RBC and blood platelets were suspended isotonic buffered solution with 8% of gelatin.

Samples in a magnetic field of 8 T and controls out of the field were kept at 35 °C for first ten minutes. After obtaining full orientation, sample temperature was decreased to about 15 °C to fix the cells in the gelatin gel. The gel containing RBC was sliced in planes normal and parallel to the field direction and observed by a optical microscope. On the other hand, the gel containing blood platelets was dried and sliced for electron microscopic observation.

A degree of orientation of particles having uniaxial shape like rod or spheroid is expressed by using the order parameter  $\langle m \rangle = \langle 3\cos^2\theta - 1 \rangle / 2$  as shown in the earlier section. As spheroidal biological cells show anisotropic scattering cross sections,<sup>26,27)</sup> the degree of orientation is monitored by observing transmitted light of cell suspension.

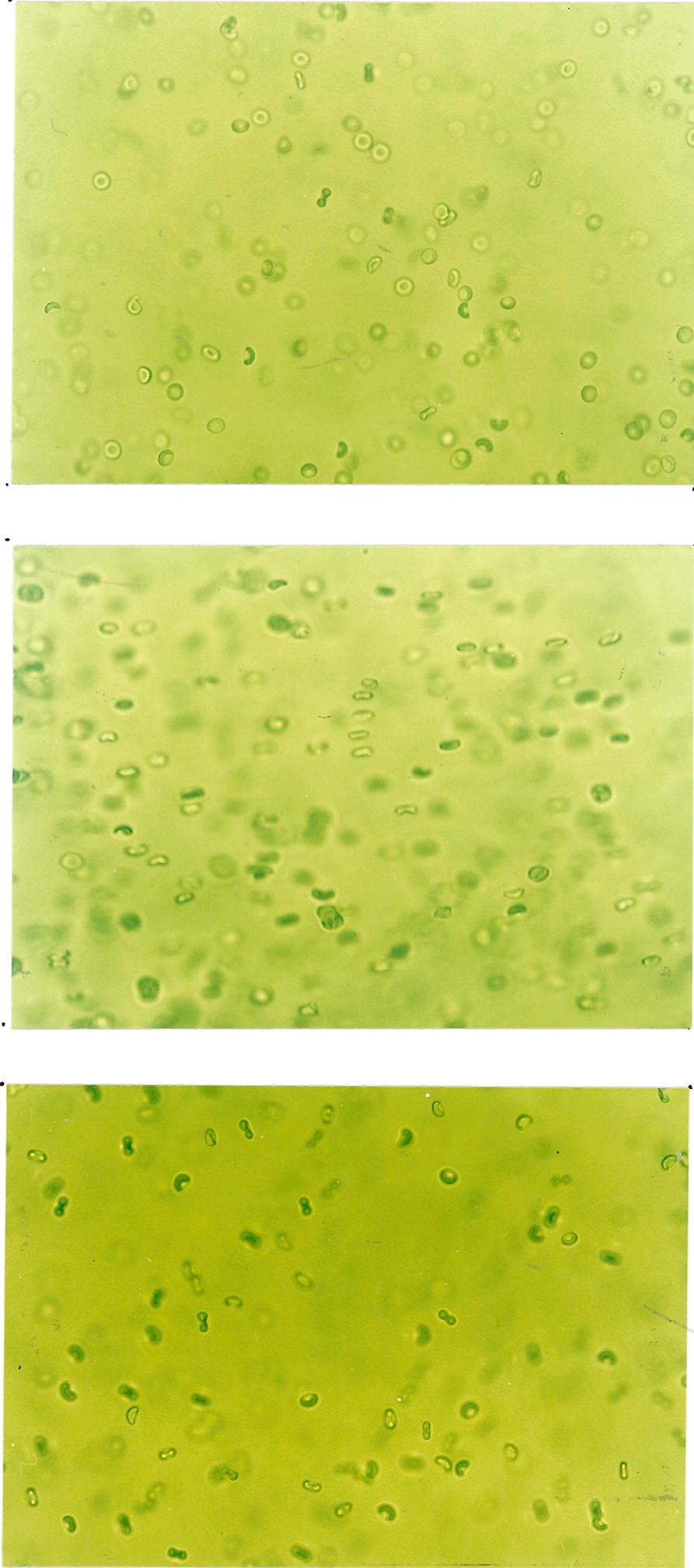
## 5-2 Magnetic orientation of red blood cells

Observation of the magnetic orientation by an optical microscope was done for examining how various kinds of RBC are oriented in the magnetic field. Figure 14 shows the optical microscopic photographs of OXY-RBC with oxygenated hemoglobin ( $S=0$ ). Figure 14(a) and (b) shows the cells gelled in a magnetic field of 8 T normal to the paper and in the direction indicated by an arrow, respectively. (c) is the control, that is gelled without a magnetic field. RBC in (c) are randomly oriented. Figure (a) shows in a field normal to the paper, all cells seem their disk plane normal to the paper and there seems no cells with their disk plane normal to the field in (b). These fact implies that they orient with their disk planes parallel to the magnetic field. DEOXY-, METH- and METL-RBC are also observed to orient in the same manner.

In solidified RBC, however, the magnetic orientation is opposite to those in normal RBC. Figure 15 show the result of optical microscopic observation of solidified RBC. All cells look like circles in Fig.15(a) in a field normal to the paper, while the side view of the circles are seen in Fig.15(b). This means that solidified RBC are oriented with their disk plane normal to the field. No big change is found for the opposite orientation in the high- and low-spin state.

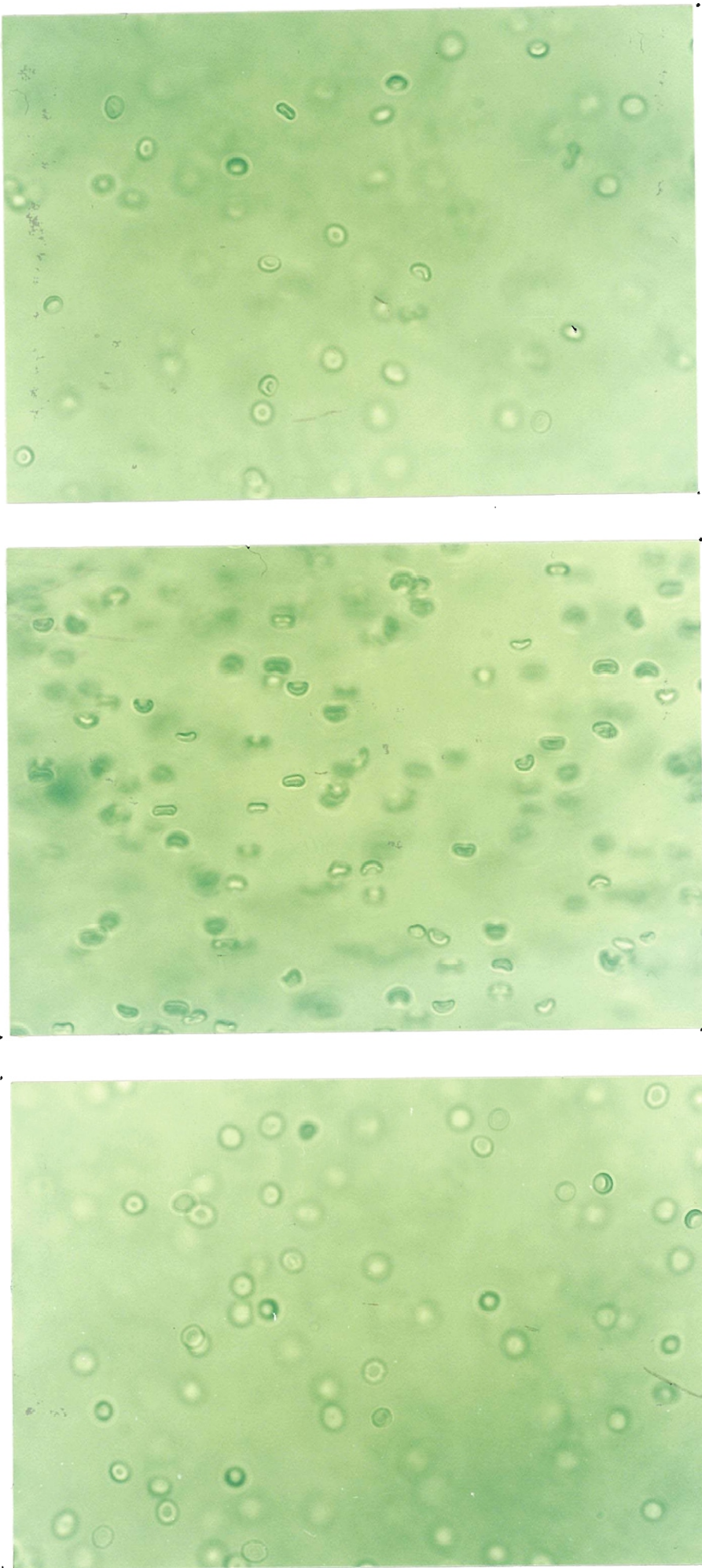
Figure 16 shows the magnetic field effect for SMETH-RBC without cell membrane. It is seen that the cells orient to be their disk plane normal to the field.

The degree of orientation is also monitored by observing



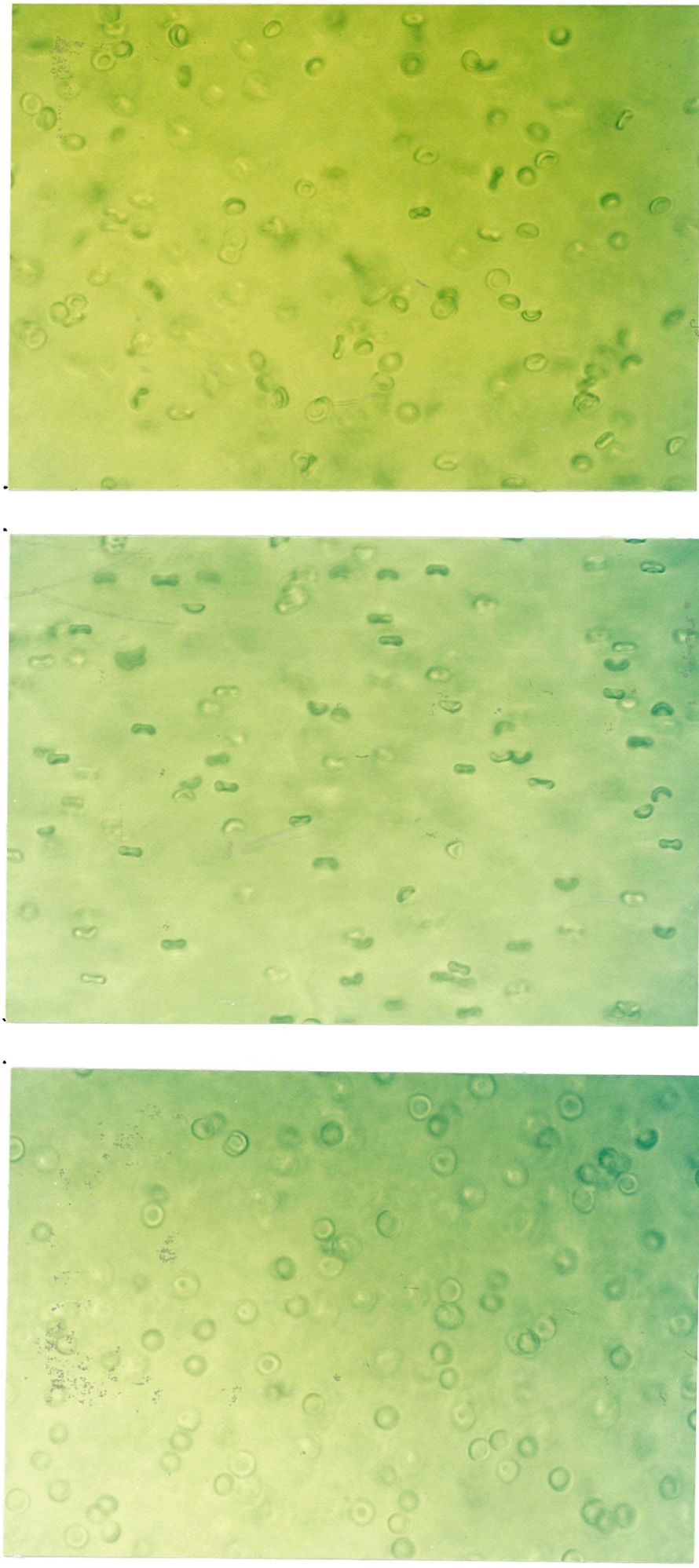
(a)  $\odot$   $H = 8 \text{ T}$        $\uparrow$   $H = 8 \text{ T}$       (c)  $H = 0$

Fig.14. Optical microscopic photographs of red blood cells. (a) and (b) shows the cells gelled in a magnetic field of 8 T normal to the paper and in the direction indicated by an arrow, respectively. (c) is the control gelled without a magnetic field.



(a)  $\odot$   $H = 8 T$  (b)  $\longrightarrow$   $H = 8 T$  (c)  $H = 0$

Fig.15. Optical microscopic photographs of solidified red blood cells in a field of 8 T applied (a) normal to the paper and (b) horizontally indicated by an arrow. (c) is the control.



(a)  $\odot$   $H = 8 T$  (b)  $\longrightarrow$   $H = 8 T$  (c)  $H = 0$

Fig.16. Optical microscopic photographs of solidified red blood cells without their bilayer lipid membrane in a field of 8 T applied (a) normal to the paper and (b) horizontally indicated by arrow. (c) is the control.

the optical transmittances of the cell suspension with and without magnetic field. Figure 17 shows the change of transmission as a function of the magnetic field for two kinds of RBC with diamagnetic OXY-RBC and paramagnetic DEOXY-RBC. No significant differences are found between data for both RBC and this means that the magnetic orientation of normal RBC is caused mainly by their diamagnetic susceptibility of the membrane. The diamagnetic anisotropy of these RBC is obtained as  $\Delta\chi = 8 \times 10^6 D_B / \text{cell}$  comparing these data with the theoretical curve and  $\Delta\chi$  for METH- and METL-RBC are obtained as  $4 \times 10^6 D_B / \text{cell}$ .

Examples of the magnetic orientation of SMETH-RBC is shown in Fig.18. A large opposite orientation are found. This is consistent with the results of the observation by an optical microscope. The magnetic orientation curves show sample dependence probably due to the concentration dependence of MET-hemoglobin in SMETH-RBC.

The origin of the opposite orientation of solidified RBC may be explained by introducing an order of hemoglobins in the cell when it is solidified. The mean ratio of the cell membrane versus the ingredient is about 1/70. Therefore, a large change in the net  $\Delta\chi$  is expected if there is considerable coherent arrangement of hemoglobin molecule in a cell. Both the paramagnetic and diamagnetic anisotropy can be considered for the ingredients but the details are difficult to estimate.

The numerical evaluation of anisotropic diamagnetic susceptibility  $\Delta\chi$  of normal OXY- and DEOXY-RBC is done by the following model. The  $\Delta\chi$  of normal RBC mainly comes from cell mem-

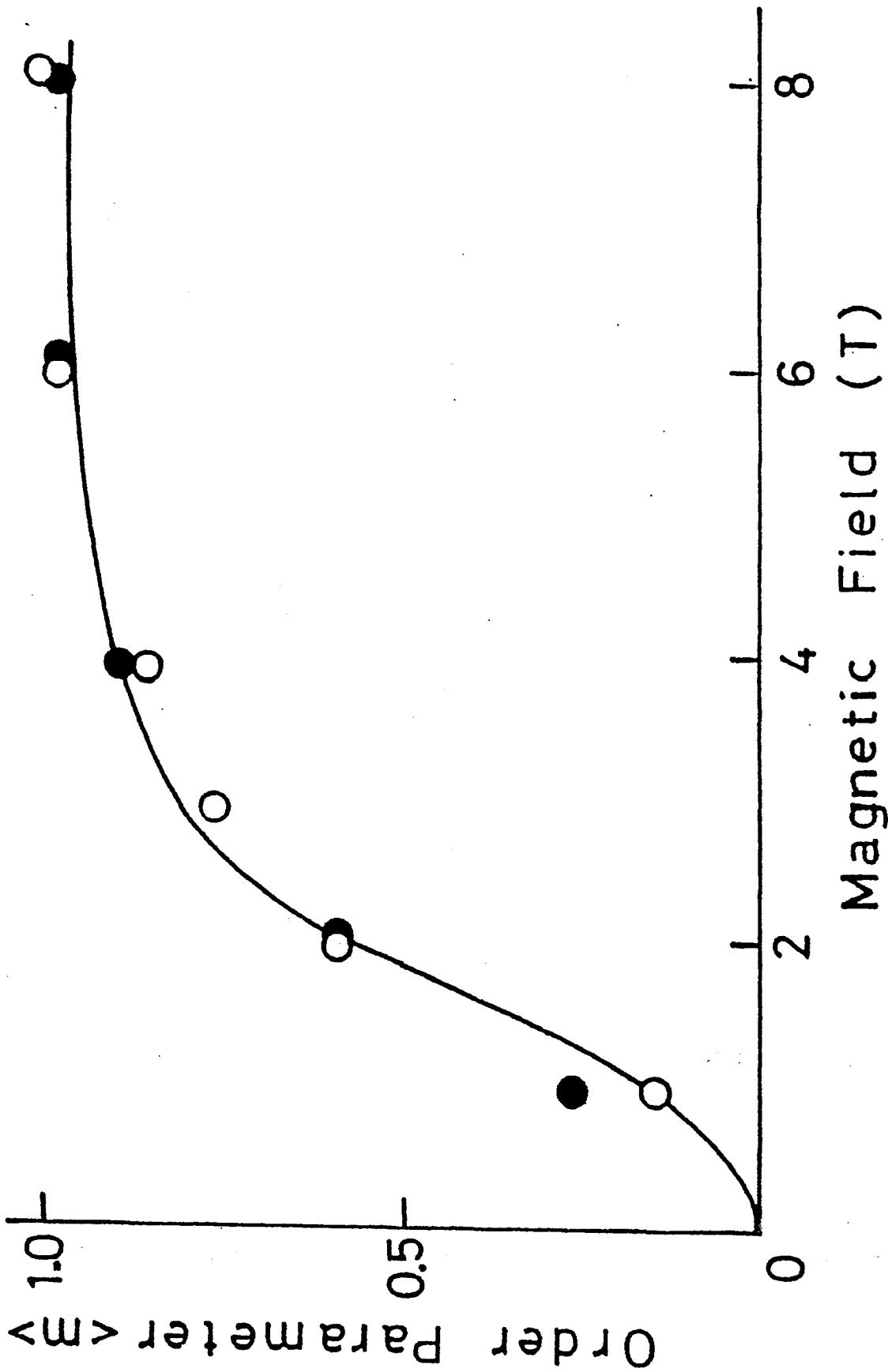


Fig.17. Magnetic orientation of OXY- (open circles) and DEOXY-red blood cells (closed circles) which contain diamagnetic and paramagnetic hemoglobin, respectively.

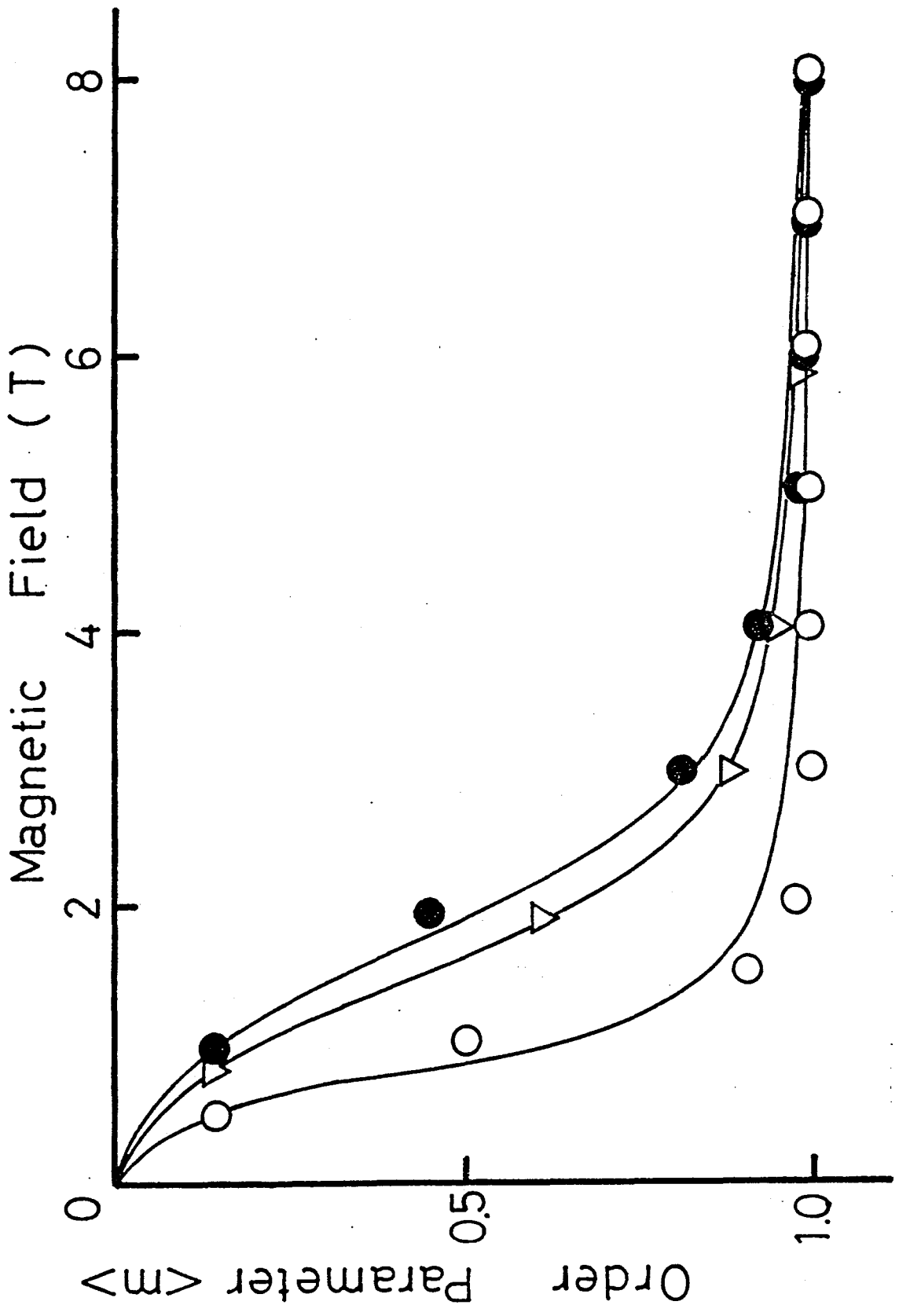


Fig.18. Magnetic orientation of solidified red blood cells (SMETH-RBC). These curves show sample dependence in SMETH-RBC.

brane, because hemoglobins are freely movable in the cells. The proteins in membrane are considered to be randomly directed and its contribution is neglected here. However, a lipid molecule in membrane has diamagnetic anisotropy of  $\Delta\chi_{\text{lipid}}=(9\pm 1)\times 10^{-2}D_B^{16}$ ) and is oriented with its hydrocarbon chains normal to the magnetic field. A number of them are aggregated to make a bilayer membrane with their long hydrocarbon chains normal to the membrane surface. The schematic views of lipid molecule and bilayer membrane are shown in Fig.19.

The number of lipid molecules in membrane is about  $N_{\text{lipid}}=3\times 10^8$ . It is assumed that RBC to be a disk with a concentric hole and its outer diameter, thickness, hole diameter and its depth are to be 7.5, 2.5, 2 and 2  $\mu\text{m}$ , respectively, as shown in Fig.20. The lateral areas  $S_1$  (disk planes) and  $S_2$  defined in Fig.20 are 88.4  $\mu\text{m}^2$  and 71.5  $\mu\text{m}^2$ , respectively. It is assumed that the lipid molecules are distributed uniformly in these area. The  $\Delta\chi$  of normal RBC is given by

$$\begin{aligned}\Delta\chi &= N_{\text{lipid}} \times \Delta\chi_{\text{lipid}} \times (S_1 - S_2/2)/(S_1 + S_2) \\ &= (9\pm 1)\times 10^6 D_B / \text{cell}.\end{aligned}\tag{17}$$

This is compared with the experimental value,  $\Delta\chi=8\times 10^6 D_B/\text{cell}$ . They show good agreement in spite of rough estimation so that it may be concluded that the origin of  $\Delta\chi$  in normal RBC is mainly attributed to membrane lipid molecules. This is also consistent with the optical microscopic observation because lipid molecules tend to orient normal to the field.

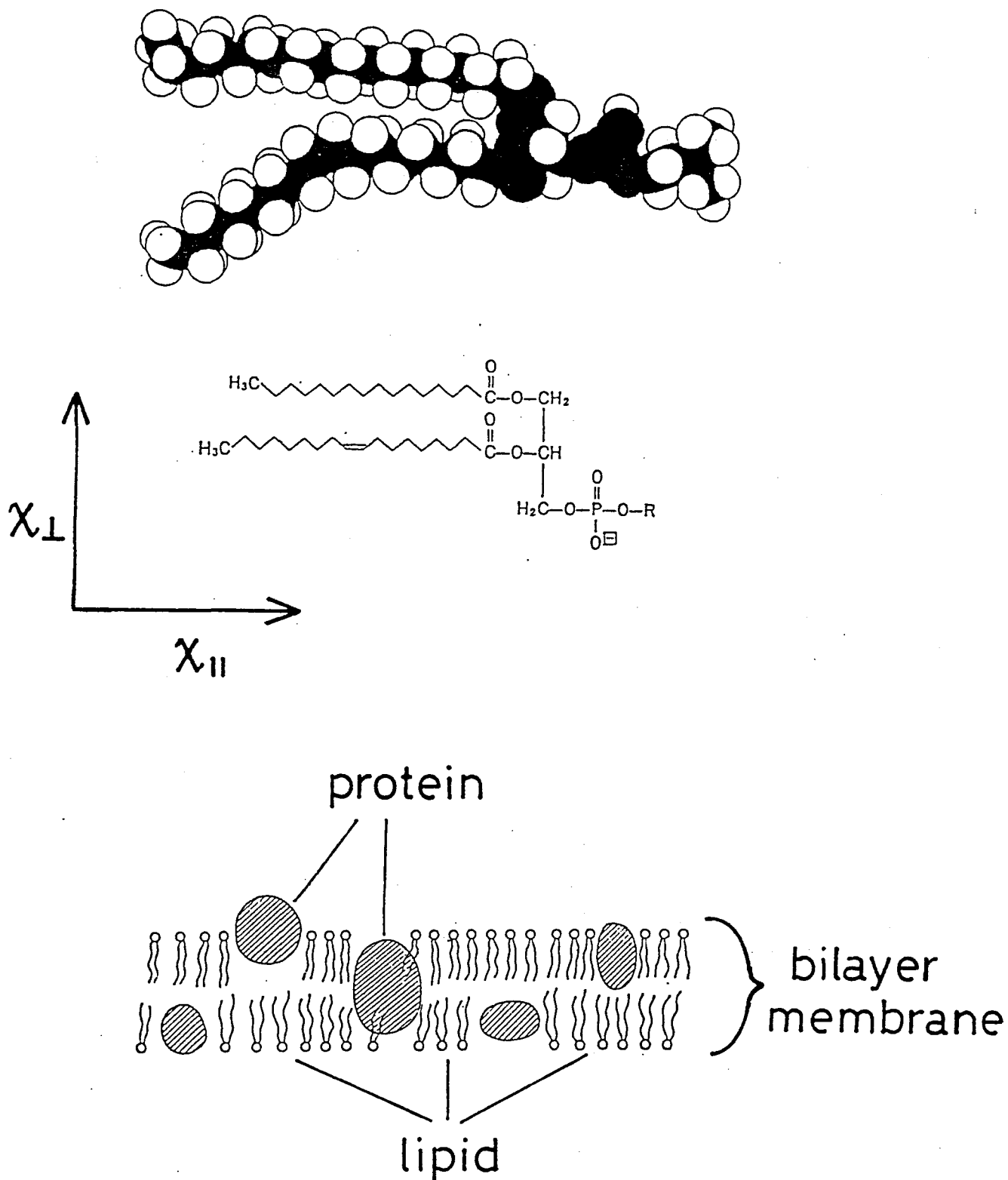


Fig.19. Schematic views of lipid molecule and bilayer membrane. The lipid molecule has the anisotropic diamagnetic susceptibility and is oriented with their hydrocarbon chains normal to the magnetic field.

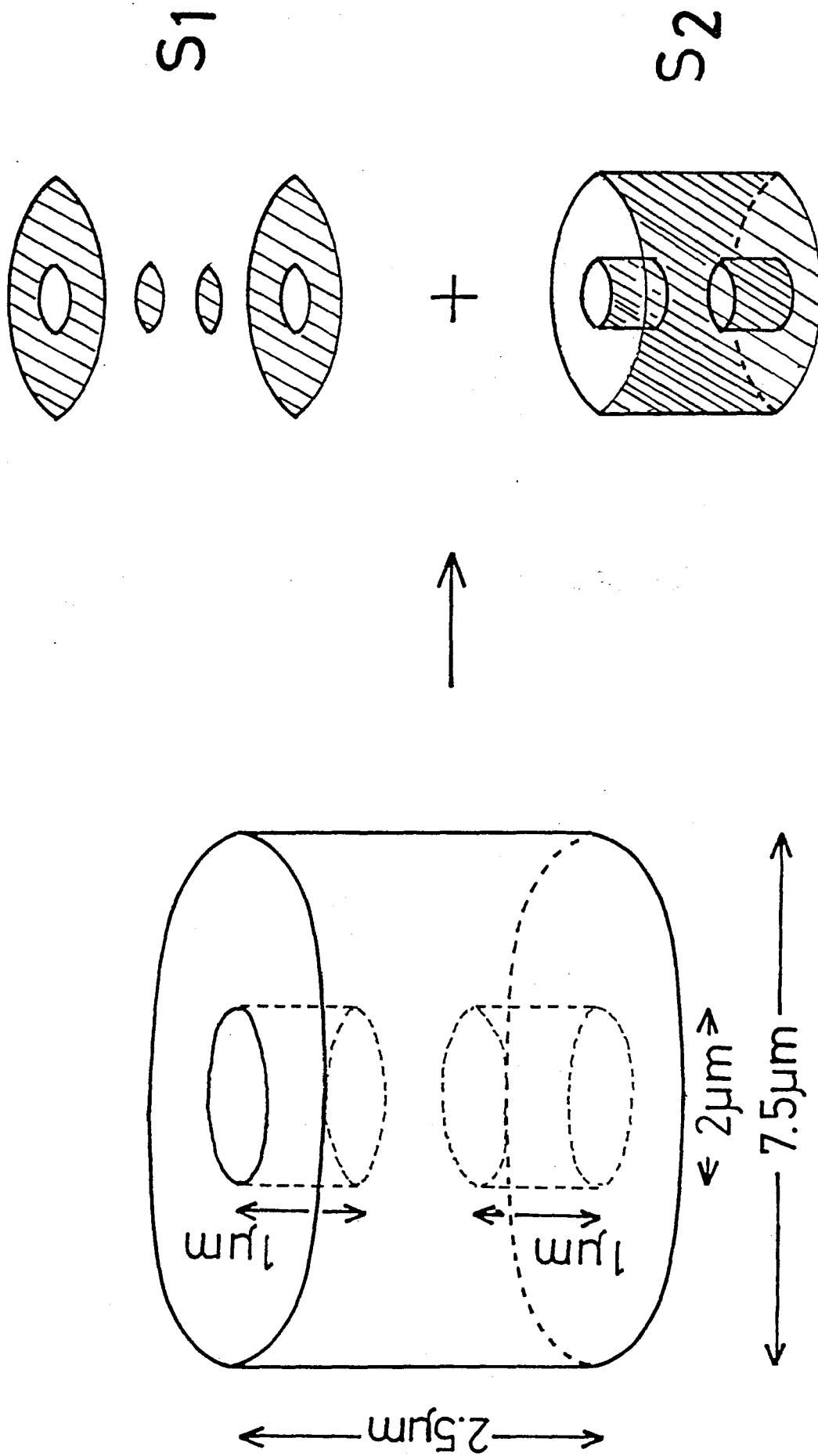


Fig. 20. A model shape of red blood cell. The lateral areas  $S_1$  and  $S_2$  are indicated by the oblique lines in the right hand figures.

### 5-3 Magnetic orientation of blood platelets

Figure 21 and 22 show the results of optical microscopic observation and SEM images of blood platelets, respectively. All cells look like ellipses in Figs. 21(a) and 22(a) in a field normal to the paper. The side view of ellipses are seen in Fig. 21(b) and there seems no cells with their disk plane normal to the field. It is found from these experiments that blood platelets orient with their disk plane parallel to the field.

Figure 23 shows the experimental results of transmission measurements and the theoretically calculated  $\langle m \rangle$  curve for blood platelets.  $\Delta\chi = 1.2 \times 10^7 D_B / \text{cell}$  is obtained experimentally.

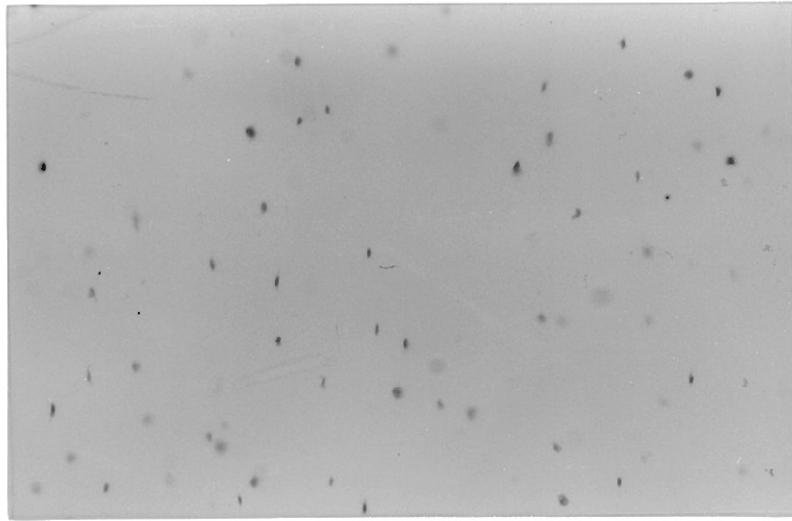
The effect of solidification of proteins is examined in blood platelets. The solidified blood platelets are also oriented with their disk plane parallel to the field and have the same  $\Delta\chi$  of normal blood platelets in contrast with the case of RBC.

The value of  $\Delta\chi$  in blood platelet is 1.5 times larger than that of OXY- or DEOXY-RBC even though blood platelet has a smaller size than RBC as shown in Fig. 13. The contribution of diamagnetic anisotropy of bilayer lipid membrane to the  $\Delta\chi$  of a blood platelet can be evaluated by the same way in RBC. It is  $(0.13 \pm 0.01) \times 10^7 D_B / \text{cell}$  by assuming a disk shape with diameter of  $2.5 \mu\text{m}$  and thickness of  $0.6 \mu\text{m}$ . This value of the  $\Delta\chi$  of membrane is about one order smaller than that of blood platelet. Therefore, the large  $\Delta\chi$  of blood platelet can not be explained by the lipid membrane.

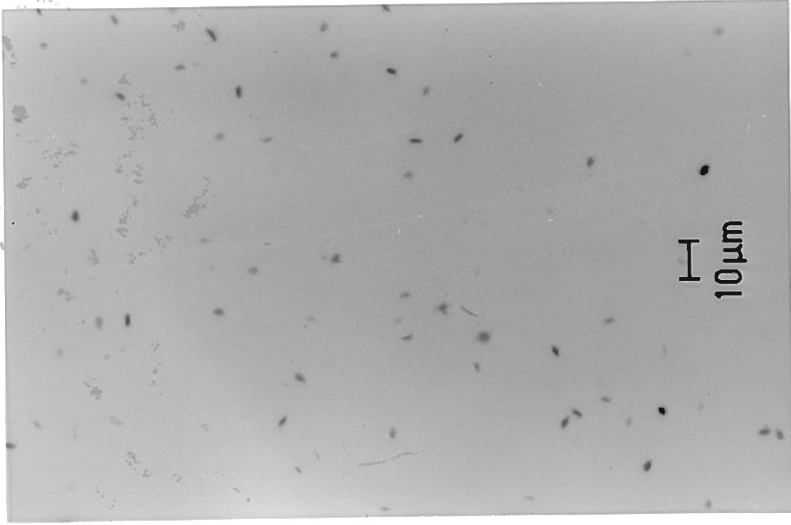
It is known that blood platelets have highly directed



(a)  $\odot$   $H = 8 T$

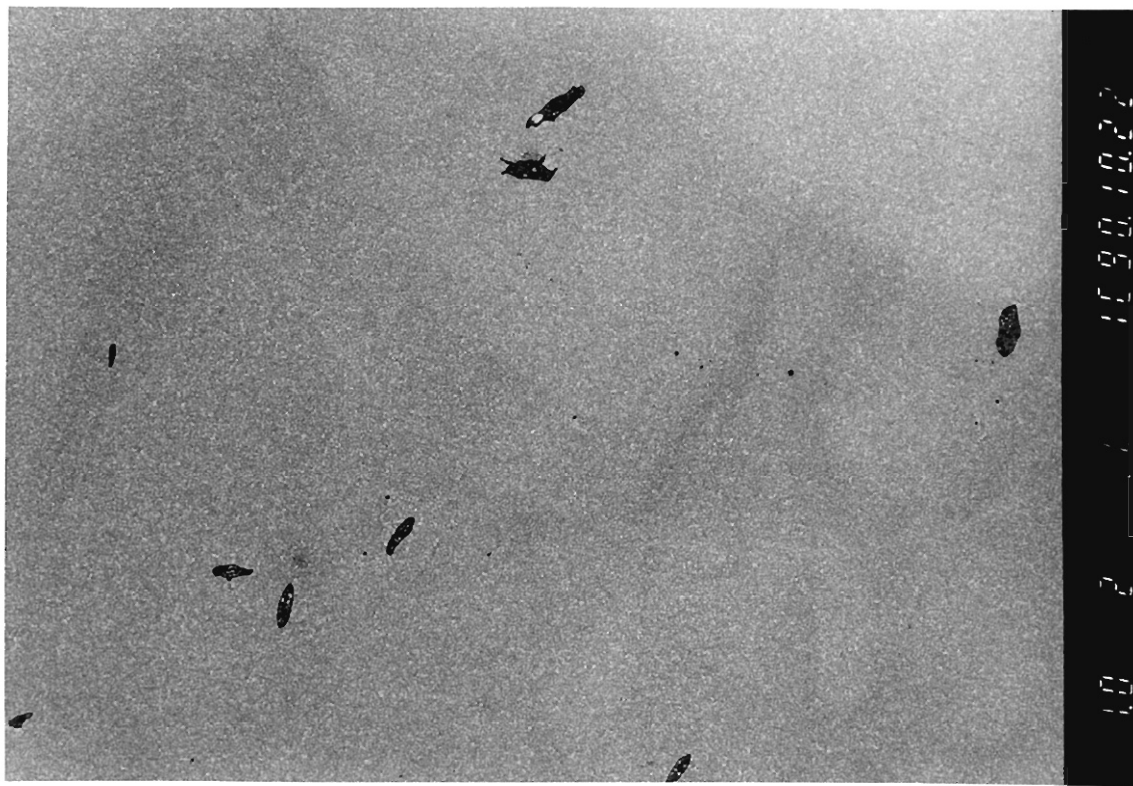


(b)  $\longrightarrow$   $H = 8 T$



(c)  $H = 0$

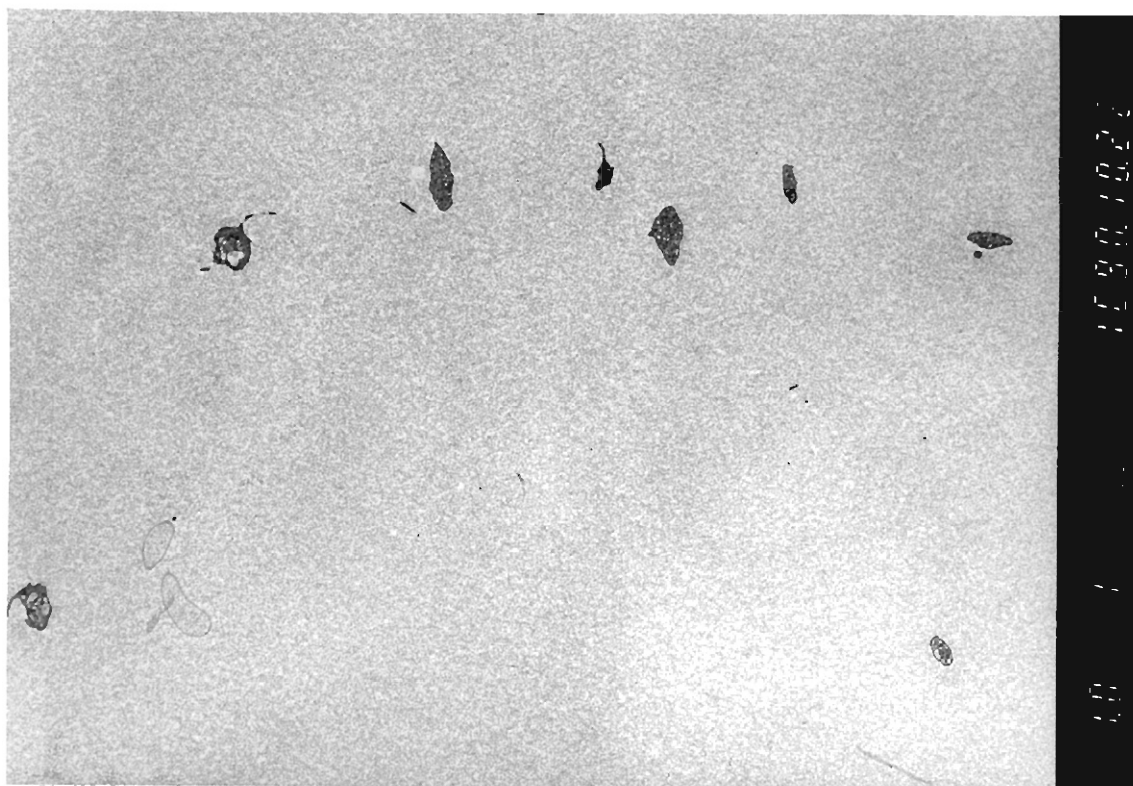
Fig.21. Optical microscopic photographs of blood platelets in a magnetic field of 8 T applied (a) normal to the paper and (b) horizontally indicated by an arrow. (c) is the control gelled without the field.



(a)

⊙

H=8 T



(b)

H=0

Fig.22. Scanning electron microscope images of blood platelets (a) in a magnetic field of 8 T applied normal to the paper and (b) out of magnetic field.

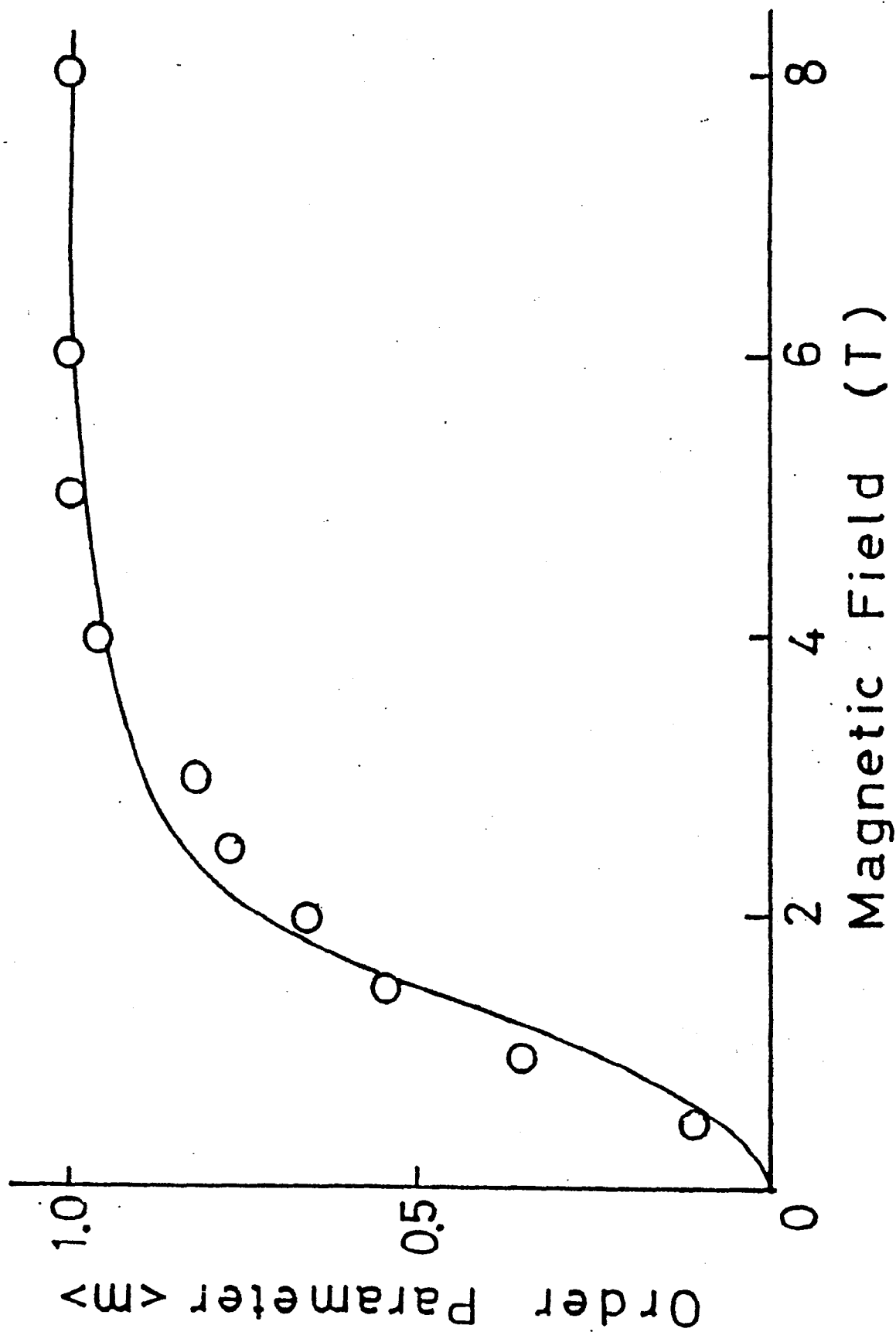


Fig.23. Magnetic orientation of blood platelets.

fibrous protein, microtubules, in the cell as shown in Fig.24. Microtubules serve as cell's cytoskeleton and exist about 15 turns in blood platelet. They are hollow tubes of protein with an outer diameter of 24 nm and consist of  $\alpha\beta$  tubulin dimers, aligned head to tail as shown in Fig.25. The dimers have a molecular weight of about 100,000. The tertiary structure of tubulin dimers has not been obtained.

The polymerization of tubulin dimers extracted from the brain of a cow is investigated in the magnetic field of 1 T. Examples of transmission electron microscopic photographs of the microtubules are shown in Fig.26. Almost all of the microtubules polymerized in a magnetic field are aligned to the field direction which is indicated by an arrow in (a). This result shows that microtubules have large anisotropic diamagnetic susceptibility.

As microtubules have coaxial form in blood platelet and tend to orient parallel to the field, they make blood platelet orient with its disk plane parallel to the field. Therefore, microtubules probably have important contribution to the  $\Delta\chi$  of blood platelet in addition to that of membrane.

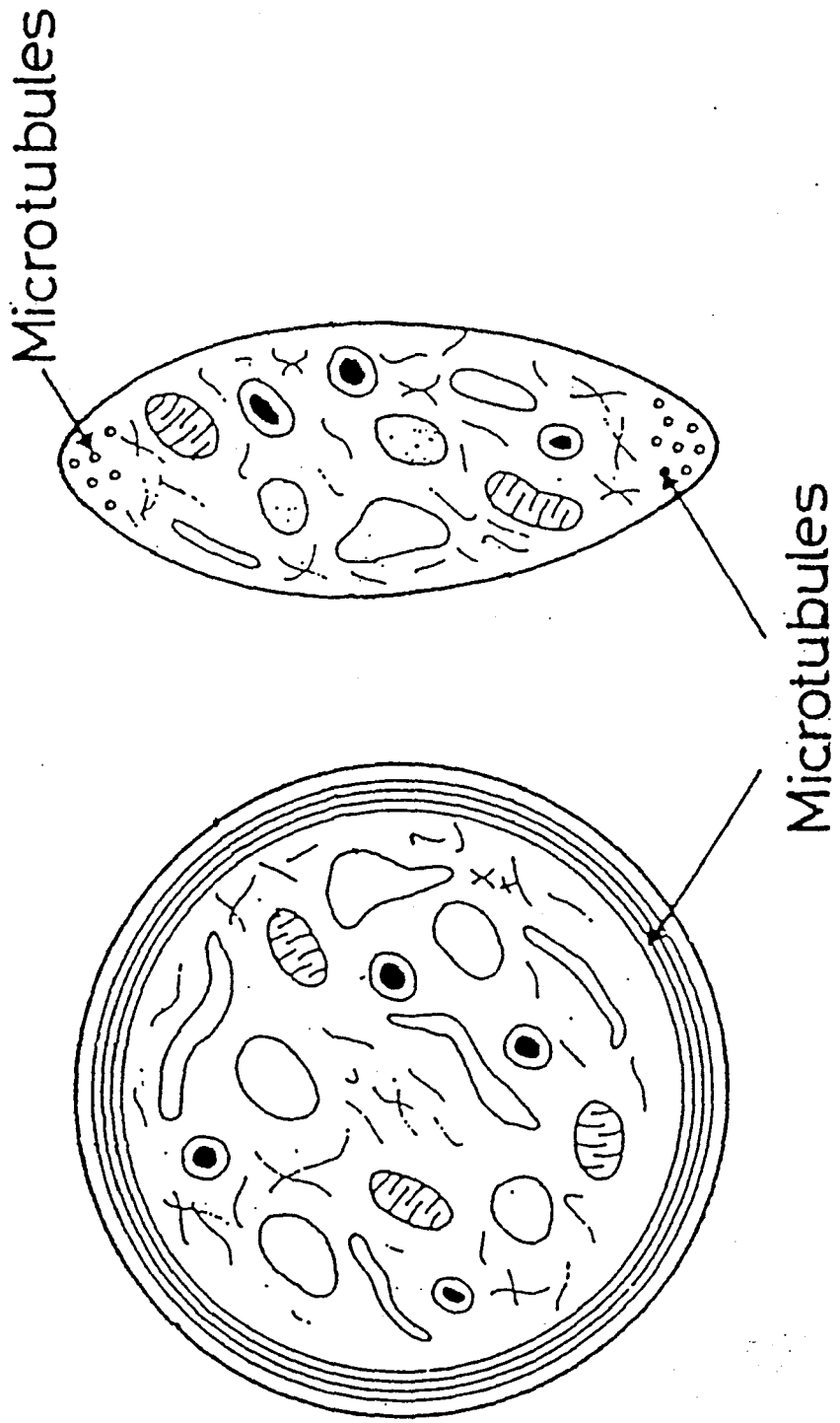


Fig.24. Schematic drawings of blood platelet and Microtubules. Microtubules is a cytoskeleton of blood platelets.

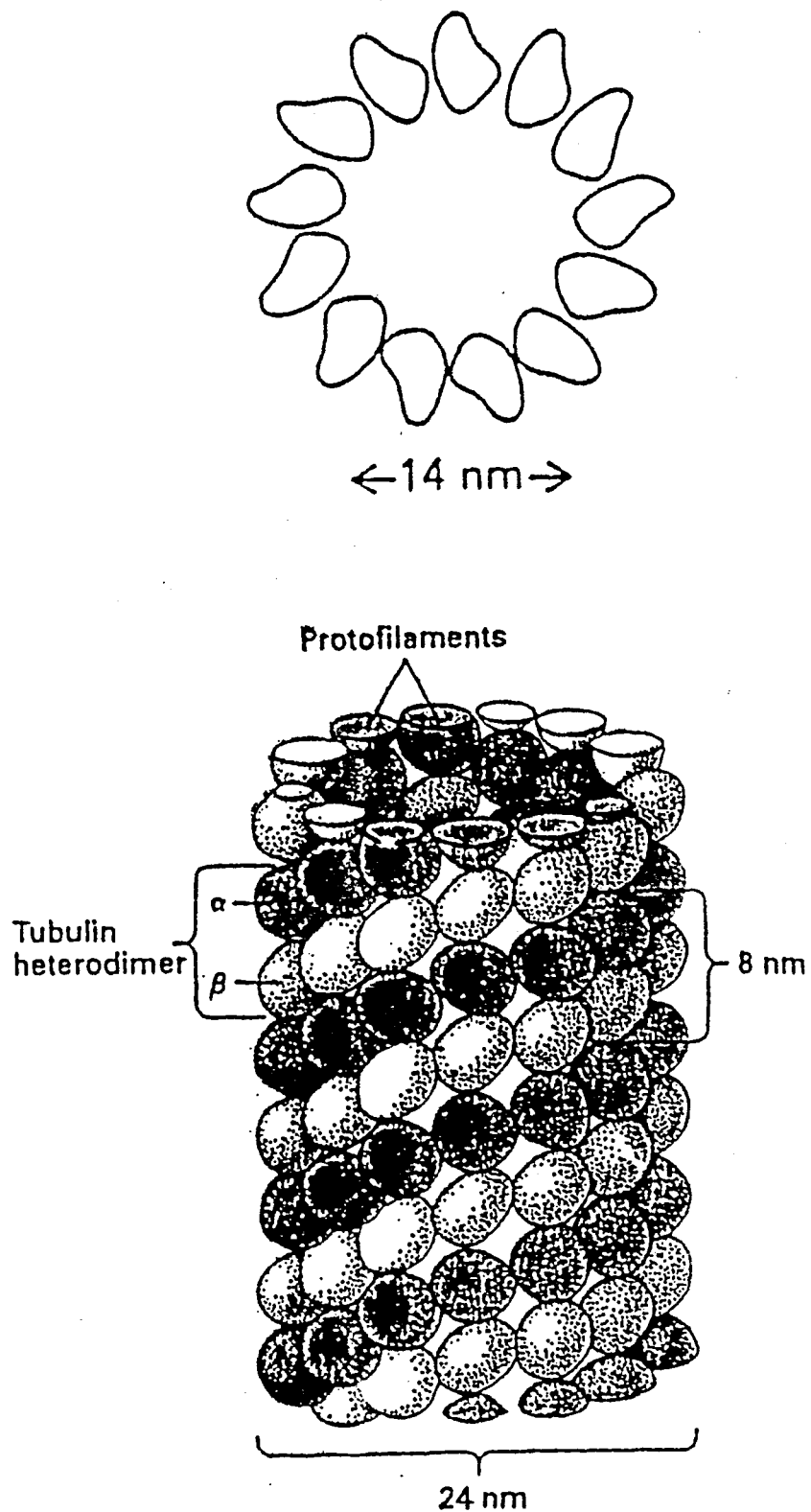
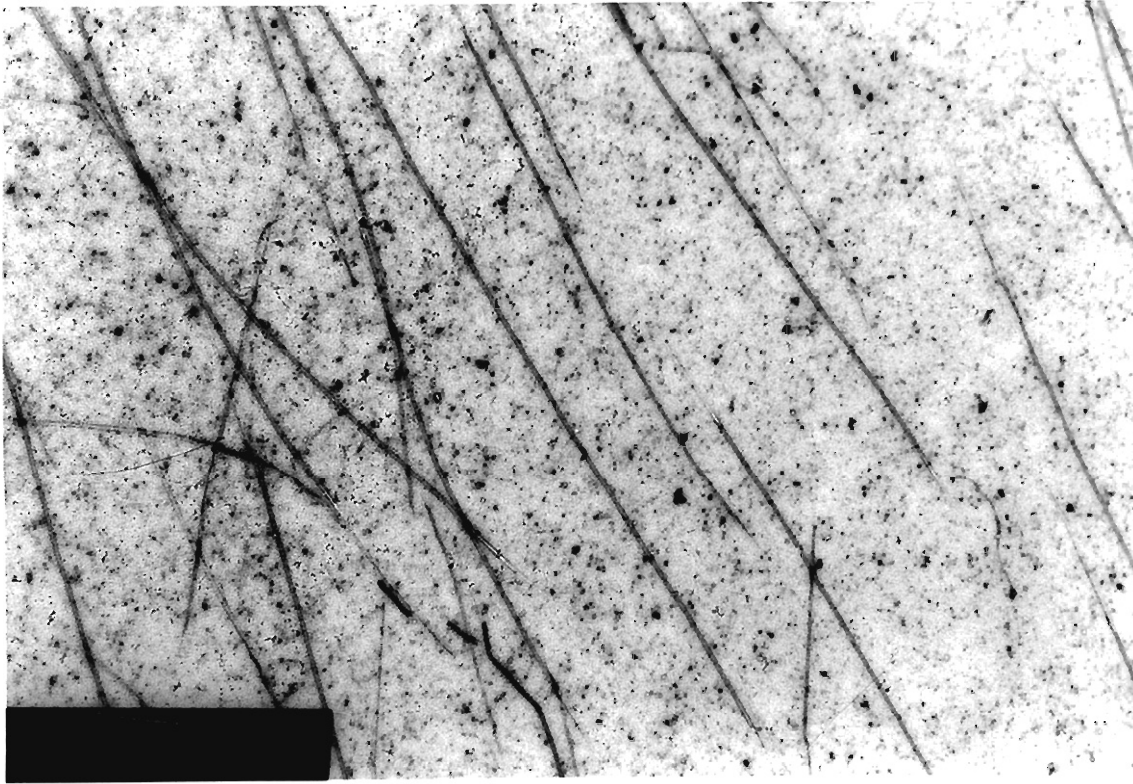


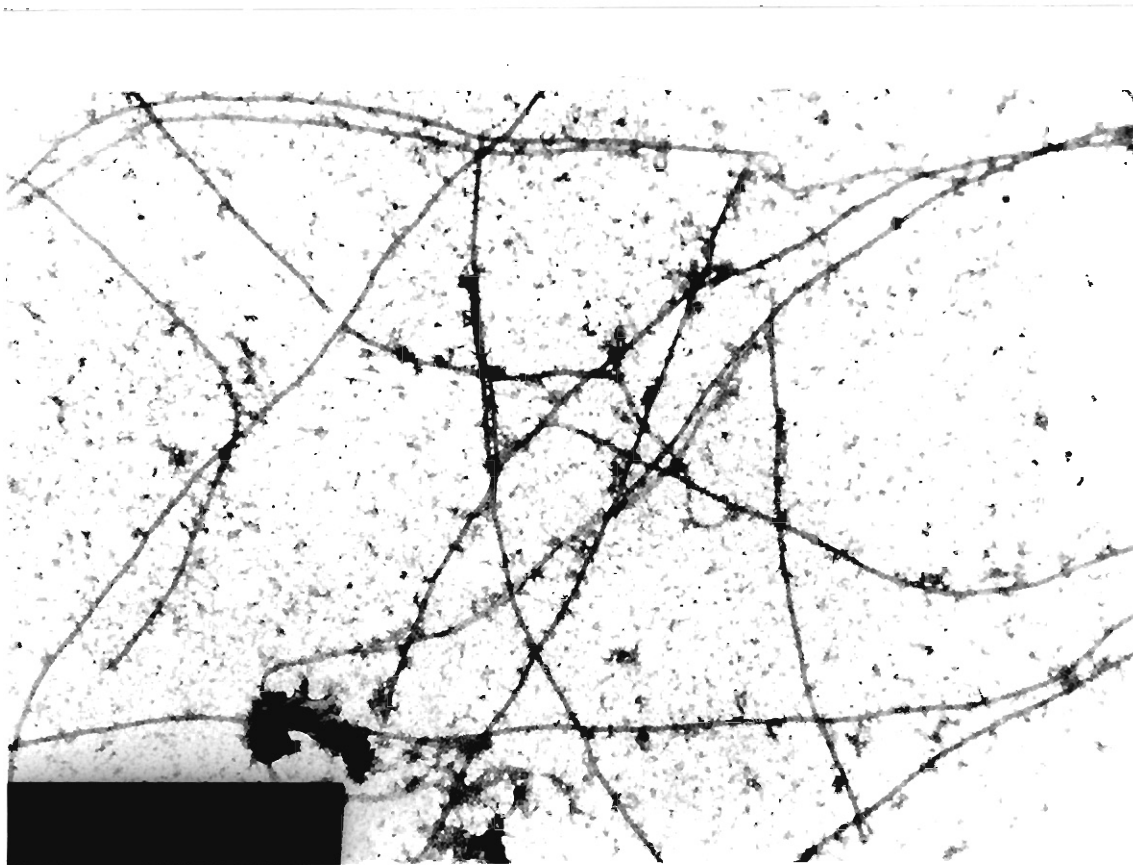
Fig.25. Three dimensional structure of a single microtubules. The tubulin poly-peptides are aligned in 13 parallel rows, called protofilaments. Each protofilament is composed of  $\alpha\beta$  tubulin dimers, aligned head to tail.



(a)



$H=1T$



(b)

$H=0$

— 1  $\mu\text{m}$

Fig.26. Transmission electron microscopic photographs of microtubules polymerized (a) in and (b) out of a magnetic field of 1 T.

## 6. Conclusion

The magnetic field effects on the polymerization of fibrin fibers have been investigated first. The polymerization process is enhanced by adding the specific enzyme thrombin into the fibrinogen solution. Almost 100% alignment is observed at the field of 8 T by measuring the polarization of transmitted light and also by means of scanning electron microscope (SEM). The number of fibrinogen aggregated in a fibrin fiber shows a rapid increase in the first 15 min. up to about  $5 \times 10^5$  and in the finally a fiber has about  $10^6$ - $10^7$  fibrinogens in average. Considerable orientation is obtained even in a field as low as 1 T. This implies that the magnetic field effect on the human body might not be negligible even if a magnetic field is of the order of 1 T.

Normal red blood cells are found to align by a magnetic field with their disk planes parallel to the field irrespective of the spin states. The origin of the anisotropic susceptibility of normal red blood cells is attributed to the diamagnetic bilayer lipid membrane of the cells.

Solidified red blood cells are observed to align with their disk planes normal to the magnetic field. The alignment is opposite to those in normal cells. This implies that the magnetic orientation of red blood cells are modified by the solidification of proteins in the cells where the solidified hemoglobins are not random but have some coherence in the cells.

Blood platelets are found to align with their disk plane parallel to the magnetic field. The size of blood platelet is

smaller than that of red blood cells but the anisotropic diamagnetic susceptibility of blood platelets is 1.5 times larger than that of red blood cells. The large  $\Delta\chi$  is explained by introducing the contribution from microtubules which have large anisotropic diamagnetic susceptibility.

#### REFERENCES

- 1) M. Faraday: Exp. Res. Elect. (London) 3(1855)27.
- 2) K. Landsdale: Proc. Soc. London Ser. A171(1939)541.
- 3) W. Arnold, R. Steele and H. Muller: Proc. Natl. Acad. Sci. USA 44(1958)1.
- 4) Ad. J. Kalmijn and R. P. Blakemore: Proc. Intern. Union Physiol. Sci. 13(1977)364.
- 5) A. Cotton and H. Mouton: Compt. Rend. 145(1907)229.
- 6) P. Langevin: Le Radium 7(1910)249.
- 7) A. Yamagishi, E. Nagao and M. Date: J. Phys. Soc. Jpn. 53(1984)928.
- 8) A. Yamagishi and M. Date: Physica B155(1989)91.
- 9) R. Chagneux and N. Chalazonitis: C. R. Acad. Sci. Ser. D274(1972)317.
- 10) F. T. Hong, D. Mauzerall and A. Mauro: Proc. Natl. Acad. Sci. USA 68(1971)1283.
- 11) J. D. Clement-Metral: FEBS Lett. 50(1975)257.
- 12) J. Breton: Biochem. Biophys. Res. Commun. 59(1974)1011.
- 13) J. F. Becker: Dissertation (New York University, New York) (1975)
- 14) D.-Ch. Neugebauer, A. E. Blaurock and D. L. Worcester: FEBS Lett. 78(1977)31.
- 15) G. Maret and K. Dransfeld: Phys. Status solidi B&C 85(1977)1077.

- 16) C. Rosenblatt, P. Yager and P. E. Schoen: *Biophys. J.* 52(1987)295.
- 17) J. Horau, N. Lumbroso and A. Pacault: *Compt. rend.* 242(1956)1702.
- 18) A. Yamagishi, T. Takeuchi, M. Date and T. Higashi: *Physica B* 155(1989)433.
- 19) A. Yamagishi, T. Takeuchi, T. Higashi and M. Date: *J. Phys. Soc. Jpn.* 58(1989)2280.
- 20) A. Yamagishi, T. Takeuchi, T. Higashi and M. Date: *Physica B* 164(1990)222.
- 21) W. E. Fowler, R. R. Hantgan, J. Hermans and H. P. Erickson: *Proc. Natl. Acad. Sci. USA* 78(1981)4872.
- 22) J. Torbet: *Biochem.* 25(1986)5309.
- 23) R. F. Doolittle, D. M. Goldbaum and L. R. Doolittle: *J. Mol. Biol.* 120(1978)311.
- 24) L. Pauling: *Proc. Natl. Acad. Sci. USA* 76(1979)2293.
- 25) D. L. Worcester: *Proc. Natl. Acad. Sci. USA* 75(1978)5475.
- 26) E. W. Montroll and R. W. Hart: *J. Appl. Phys.* 22(1951)1278.
- 27) V. Twersky: *J. Opt. Soc. Am.* 60(1970)1084.
- 28) J. M. Steinke and A. P. Shepherd: *Appl. Phys.* 27(1988)4027.

#### ACKNOWLEDGEMENTS

The author wishes to express his sincere gratitude to professor Muneyuki Date for his valuable suggestion and enlightening discussions, and his continuous encouragement during the present work. He would like to thank Dr. Koichi Katsumata of the Institute of Physical and Chemical Research(RIKEN) for supplying samples of Haldane gap materials and fruitful discussions. He also would like to thank Professor Terumasa Higashi of College of Biomedical Technology, Osaka University for supplying samples of biological systems and helpful discussions.

He would like to thank Professor Akio Yamagishi of the Research Center for Extreme Materials, Osaka University for many helpful suggestions on use of high magnetic field laboratory and helpful discussions on magnetic orientation of biological systems. He also would like to thank Professor Hidenobu Hori for his valuable suggestions on the techniques of magnetization measurement. He would like to thank Dr. Taturu Yosida of Low Temperature Center, Osaka University for Supplying single crystals of NENP and NINO. He also would like to thank to Dr. Koichi Kindo for his useful discussion on Haldane problem.

He is indebted to Mr. Mitsuru Ono for the cooperation in analysis of the magnetic susceptibility results. He is also indebted to Mr. Toshiyuki Mizuno for the cooperation in the various measurements on magnetic orientation of biological systems.

Finally, the author wishes to thank all the members of Date laboratory.

